
Combined Theoretical and Experimental Studies
of Some Antiperovskite Systems for Energy
Applications

A thesis

submitted in partial fulfilment of the requirements for the

Doctor of Philosophy

By

Sk Mujaffar Hossain

(20163471)



Department of Chemistry

Indian Institute of Science Education and Research (IISER)

Pune 411008, Maharashtra, India

May 2022

To my parents

Certificate

Certified that the work incorporated in the thesis entitled **Combined Theoretical and Experimental Studies of Some Antiperovskite Systems for Energy Applications** submitted by **Sk Mujaffar Hossain** was carried out by the candidate, under our supervision. The Computational part of the thesis has been guided by Dr. Prasenjit Ghosh while the experimental part has been guided by Prof. Satishchandra Ogale. The work presented here or any part of it has not been included in any other thesis submitted previously for the award of any degree or diploma from any other University or institution.



(Dr. Prasenjit Ghosh)

Thesis supervisor

Date: 25-05-2022



(Prof. Satishchandra Ogale)

Thesis Co-supervisor

Declarations

I, Mr. **Sk Mujaffar Hossain**, declare that this written submission represents my ideas in my own words and wherever other's ideas have been included, I have adequately cited and referenced the original sources. I also declare that I have adhered to all principles of academic honesty and integrity and have not misrepresented or fabricated or falsified any idea / data / fact / source in my submission. I understand that violation of the above will cause for disciplinary action by the Institute and can also evoke penal action from the sources which have thus not been properly cited or from whom proper permission has not been taken when needed.



Date: 25-05-2022

(Sk Mujaffar Hossain)

Roll No. 20163471

Acknowledgements

As I near the end of my Ph.D. program, I'd like to express my gratitude and appreciation to everyone who has assisted me in some way, directly or indirectly, in completing this difficult but rewarding journey and making things easier and more enjoyable for me.

To begin, I'd like to express my deep sense of gratitude to my supervisors, Dr. Prasenjit Ghosh and Prof. Satishchandra Ogale, for allowing me to work with them. Their invaluable guidance and support throughout my working career enabled me to complete my Ph.D. on time. Everything I've learned during the last five years is thanks to them. They have assisted me not only with professional advice and supervision but also on a personal level by taking care of me and constantly thinking about my health and career.

Prof. Ogale was instrumental in educating me on the experimental front, a new frontier for me, and constantly motivated me to learn new things. His upbeat demeanor and unwavering enthusiasm for research served as a strong source of inspiration for everyone who works with him including me. His helping attitude and human qualities are undeniably admirable as an educator.

I'd like to express my gratitude to Prof. M. Jayakannan, the former chair of the IISER Pune Chemistry Department, for helping me with the Ph.D. guide assignment process. Dr. Prasenjit Ghosh, faculty of the Physics Department, was also extremely helpful throughout the process. I admire their initiatives and efforts to assist graduate students.

I am grateful to IISER Pune for providing me with the opportunity to work in such a prestigious institute, as well as for the research funding and fellowship. I thank Prof. Jayant Udgaonkar and Prof. K. N. Ganesh the current and former directors of IISER Pune, for providing us with first-rate research facilities, a healthy research environment, and a charming campus. I thank the Department of Chemistry and the Department Chair Prof. H. N. Gopi for providing us with all of the resources we needed to conduct our research and for not letting us stop working under any circumstances.

I wish to sincerely thank Dr. Angshuman Nag and Prof. R Boomi Shankar, members of my RAC, for their helpful suggestions during RAC meetings that helped me improve the quality of my work and approach to doing scientific research significantly. I'd also like to thank the IISER Pune faculty for all of their assistance and support in various situations, as well as my coursework mentors for their excellent instruction.

I owe a debt of gratitude to the technical and non-technical staff members of IISER Pune for their friendly demeanor when I approached them for assistance. They are always willing to assist students and provide them with the information they need to solve problems. I am fortunate to have a large group of almost 30 people, so I don't want to miss anyone's name in my attempt to thank everyone. From the bottom of my heart, I am grateful to all of the seniors and juniors for their constant assistance, support, and friendliness. They've always done their best to make me feel at ease at work by creating a welcoming atmosphere. I'll never forget how they treated me during the ups and downs of my life. They always trying to cheer me up and make working in the lab enjoyable.

I would like to give my special thanks to Prof. Sunit Rane of C-MET Pune for helping with Raman Spectroscopy measurement on an emergency basis. My special thanks to Prof. C P Vinod of NCL Pune for helping with the XPS measurement. Finally, I want to give my sincere thanks to Prof. Sunil Nair of IISER Pune and his Ph.D. student Anna Merin Francis for helping in a crucial time.

I would like to give my special thanks to my closest friends Montu Modak, Sourav Majhi, Hasem Ali, Arinda Ghosh, Kingshuk Roy, Kanika Kohli, Aswathi Mohan, Bharati Debnath Vineet, Unmesh, Rahul Sir, Shubbu, Anil, Abhijit Biswas, Rajesh Mondal for their support during my crunch time.

Finally, I want to express my heartfelt gratitude to my parents and family for their unwavering love, support, and patience. Their influence has shaped me into who I am today. I would not have made it this far if they had not been so encouraging.

Sk Mujaffar Hossain

Contents

Certificate	ii
Declarations	iii
Acknowledgements	iv
Contents	vi
List of Figures	ix
List of Tables	xii
Abstract	xiii
1 Introduction	1
1.1 Importance of renewable energy and its sources	1
1.2 Status of energy in the world and its utilization	3
1.3 Future demand of energy	3
1.4 New materials for energy storage applications	4
1.5 Perovskites and Antiperovskite materials	7
1.6 The fundamental difference between perovskites and antiperovskite	7
1.7 All other properties of Antiperovskite materials	15
1.7.1 Superconductivity in Antiperovskite	18
1.7.2 Negative Thermal Expansion (NTE) in Antiperovskite	18
1.7.3 Magnetism and Magnetoresistance in Antiperovskite	19
1.7.4 Spin-polarization and magnetization of magnetic antiperovskite materials	19
1.7.5 Antiperovskite as Advanced Battery Materials	21
1.7.6 Carbide and Nitride Antiperovskite	24
1.8 Aim and scope of the thesis	25
2 Lithiation-induced Evolution of Biphasic Constitution in Intermetallic Anti-perovskite Fe_3SnC and its consequences for magnetism: A Case for Rechargeable Spintronic Battery	27
2.1 Introduction	28
2.2 Experimental and Computational Details	30
2.3 Results and Discussion	31

2.3.1	Structural and Morphological Analysis	32
2.3.2	Magnetic Measurements	37
2.3.3	DFT Based Calculations of the Electronic and Magnetic Properties	40
2.4	Conclusions	46
3	Surface-modified Antiperovskite Nitride Co_3CuN as a High Capacitive Anode Material Boosting Li-Ion Storage Capacity	47
3.1	Introduction	48
3.2	Experimental Details	50
3.2.1	Materials	50
3.2.2	Synthesis of Co_3CuN	50
3.2.3	Synthesis of Cu Excess Co_3CuN ($\text{Co}_3\text{CuN} + \text{Cu}$)	50
3.2.4	Synthesis of Surface modified Co_3CuN ($\text{Cu}_{1-x}\text{NCo}_{3-y}/\text{CuFeCo}$)	50
3.2.5	Characterization	51
3.3	Electrochemical Characterizations	51
3.3.1	Fabrication of Electrode and Coin Cell	51
3.3.2	Fabrication of Full Coin Cell	51
3.4	Results and Discussion	52
3.4.1	Synthesis Mechanism of Co_3CuN and $\text{Cu}_{1-x}\text{NCo}_{3-y}/\text{CuFeCo}$	52
3.4.2	Structural Characterization	53
3.4.3	Morphological Characterization	54
3.4.4	Electrochemical Characterization	59
3.4.5	Post-cycling characterisation of $\text{Cu}_{1-x}\text{NCo}_{3-y}/\text{CuFeCo}$	61
3.5	Conclusions	65
4	Growth and Properties of Epitaxial Heterostructure of Antiperovskite and Perovskite Using Pulsed Laser Deposition (PLD)	66
4.1	Introduction	67
4.2	Experimental Sections	71
4.2.1	Synthesis of Target Material Co_3CuN (CCN)	71
4.2.2	Structural Characterization of Target Material Co_3CuN (CCN)	71
4.2.3	Fabrication of Co_3CuN thin Film Using PLD	74
4.2.4	Structural Characterization of Co_3CuN thin film	75
4.3	Results and Discussion	78
4.3.1	XRD analysis of the CCN thin film	78
4.3.2	Raman Spectroscopy Analysis of the CCN thin film	79
4.3.3	XPS Analysis of the bulk and thin film of CCN	81
4.3.4	Resistance vs Temperature (RT) Plot	84
4.4	Conclusions	85
	Summary and Future Outlook	86
A	Experimental and Battery Details	89
A.1	Experimental Details	89

A.1.1	Synthesis Methods	90
A.1.1.1	Solid-state Method	90
A.1.1.2	Hydrothermal and Sealed Glass Tube Method	91
A.2	Fabrication of the Battery Coin Cell	93
A.2.1	Protocol of Working Electrode Preparation	93
A.2.2	Assembly of coin cell	93
A.2.3	Testing of the Coin Cell	94
A.3	Electrochemical Energy Storage	95
A.3.1	Battery	95
A.3.2	Capacitor	96
A.3.3	Supercapacitor	97
A.3.4	Types of Batteries	97
A.3.4.1	Primary Batteries	98
A.3.4.2	Secondary Batteries	98
	Bibliography	100
	Publications	133

List of Figures

1.1	Source of pollutions and it effects	2
1.2	Different renewable energy sources	2
1.3	Past and projected world energy use (source: Based on U.S. Energy Information Administration, 2011)	4
1.4	Requirement of new electrode materials for energy storage from different renewable sources (wind, solar, etc.)	5
1.5	Structural information of both perovskites and antiperovskite	8
1.6	(a) Antiperovskite, (b) Perovskite, (c) Antiperovskite, (d) Perovskite	9
1.7	(a-d) Different perovskite phases of SrSnO_3 with SnO_6 coordination, (e) Single antiperovskite phase of Sr_3SnO with Sr_6O coordination.	9
1.8	3d orbital splitting of bulk perovskite (ABX_3) and antiperovskite (X_3BA).	11
1.9	3d orbital splitting of perovskite (ABX_3) and antiperovskite (X_3BA) at the surface.	12
1.10	Structure and properties of halide and chalcogenide perovskites compared to those of the nitride antiperovskite [1].	13
1.11	Comparison of the physical properties between the 3D antiperovskite and 3D halide perovskite [1].	14
1.12	Spin Polarization of different magnetic Order (internet)	20
1.13	Sources of electron spin polarization	21
1.14	Antiperovskite materials for cathode and Solid State Electrolyte [2]	22
1.15	All antiperovskite materials for used as cathode and Solid State Electrolyte for Li and Na ion batteries [3]	23
1.16	(a) Crystal structure of Carbide and Nitride (a) Fe_3SnC , (b) Co_3CuN with Fe_6C and Co_6N octahedral co-ordination coordination was studied in this thesis.	24
2.1	(a) Capacity of Fe_3SnC and (b) Cyclic Voltametry or CV plot. [4]	31
2.2	Detail calculation of maximum number of Li atoms. [4]	31
2.3	34 lithiated configuration of 1-4Li.	32
2.4	34 Optimized lithiated configuration of 1-4Li.	33
2.5	Magnetic moments of Fe atoms of the optimize structure of Fe_3SnC and $\text{Li}_x\text{Fe}_3\text{SnC}$ ($x = 1-4$) and lattice paramters	34
2.6	(a-c) HRTEM image of lithiated compound LiFe_3SnC , Inset shows atomic details showing hexagonal arrangement; (d) represents the theoretically obtained image showing atomistic details of two-phase Fe_3C and LiSn	35
2.7	(a) HRTEM image of lithiated compound $\text{Li}_x\text{Fe}_3\text{SnC}$, Inset shows atomic details showing hexagonal arrangement; (b) represents the theoretically obtained image showing atomistic details and hexagonal arrangement; (d) crystal structure of the single lithiated compound.	36

2.8	(a), (b) M vs H plot of pure Fe ₃ SnC and a single lithiated Fe ₃ SnC at 5K and 300K.	37
2.9	(a), (b) M vs H plot of pure Fe ₃ SnC and all lithiated Li _x Fe ₃ SnC (x=1 - 4) at 5K and 300K.	38
2.10	ZFC and FCW curve of (a) pure Fe ₃ SnC, (b) single lithiated LiFe ₃ SnC.	38
2.11	ZFC and FCW curve of other lithiated phases of Fe ₃ SnC	39
2.12	Williamson Hall or WH plot: (a) Fe ₃ SnC, (b) LiFe ₃ SnC (c) Li ₂ Fe ₃ SnC (d) Li ₃ Fe ₃ SnC (e) Li ₄ Fe ₃ SnC.	41
2.13	The repeating unit of lithiated phases of Fe ₃ C: (a) LiFe ₃ C (b) Li ₂ Fe ₃ C, (c) Li ₃ Fe ₃ C and (d) Li ₄ Fe ₃ C. The different colors of the Fe atom correspond to the different magnetic moments.	41
2.14	Represents the total density of states (DOS) of unlithiated systems (a) Fe ₃ SnC and (b) Fe ₃ C	42
2.15	Represents the projected DOS of lithiated system: (a) Fe ₃ C (FM), LiFe ₃ C (FM) (b) Li ₂ Fe ₃ C (FM) (c) Li ₃ Fe ₃ C (FIM) (d) Li ₄ Fe ₃ C (FM).	43
2.16	Black and the green curve represent the experimental magnetization per Fe atom at 5K and 300K, and the blue and cyan curve represents theoretically obtained magnetic moment per Fe atom for Fe ₃ SnC and Fe ₃ C, the red and wine color curve represents the magnitude of the degree of spin polarization for both the system.	45
3.1	Schematic representation of Co ₃ CuN and Cu _{1-x} NCo _{3-y} /CuFeCo synthesis.	52
3.2	Powder XRD patterns of (a) Co ₃ CuN; (b) Cu excess Co ₃ CuN (black line) and surface reconstructed Co ₃ CuN (Cu _{1-x} NCo _{3-y} /CuFeCo) (red).	53
3.3	(a) SEM; (b) HRTEM image of CuNCo ₃ . (c) FFT image corresponds to the (111) planes of Co ₃ CuN; (d) Unit cell representation of Co ₃ CuN.	55
3.4	(a) EDAX analysis; (b) Elemental mapping of Co ₃ CuN.	56
3.5	(a-b)HRTEM image of the core-shell of Cu _{1-x} NCo _{3-y} /CuFeCo.	57
3.6	(a) Illustrates the elemental mapping of the core-shell (Cu _{1-x} NCo _{3-y} /CuFeCo) element (b) Line scan of the core-shell.	58
3.7	Charge-discharge profile in the half cell configuration (a) Co ₃ CuN and (c) Cu _{1-x} NCo _{3-y} /CuFeCo; Stability, efficiency and rate performance of (b) Co ₃ CuN and (d) Cu _{1-x} NCo _{3-y} /CuFeCo.	59
3.8	The Electrochemical impedance spectroscopic analysis for the cell (fresh cell and after 5 cycles) impedance of the pure and core-shell of Co ₃ CuN.	60
3.9	The XPS spectra of Fe, Co, and Cu elements of the core-shell of Co ₃ CuN.	62
3.10	Battery performance: (a) Charge-discharge profile in the full cell configuration using NMC-532 as the cathode and Cu _{1-x} NCo _{3-y} /CuFeCo as anode; (b) Stability and efficiency data of the full cell.	62
3.11	Post cycling ex-situ FESEM images of (a) fresh electrodes; (b) after 1st cycle; and (c) after 100th cycle of Cu _{1-x} NCo _{3-y} /CuFeCo electrodes in the half cell configuration.	63
4.1	(a) Bulk and (b) surface structure of corresponding antiperovskite and perovskite.	68
4.2	Four possible hetero-interface between antiperovskite and perovskite: (a) XA/BO ₂ (b) X ₂ N/BO ₂ (c) XA/AO (d) X ₂ N/AO.	69
4.3	Bulk and surface (001) structure of Co ₃ CuN (a-d).	70
4.4	Bulk and surface (001) structure of LaAlO ₃ (a-b).	71

4.5	(a) XRD of Co_3CuN (b) SEM image (c-d) HRTEM image (e) Optimized Co_3CuN	72
4.6	(a) EDAX analysis; (b) Elemental mapping of Co_3CuN	73
4.7	Schematic of PLD processes	75
4.8	(a-c) Thin film XRD of Co_3CuN	76
4.9	SEM EDX and AFM image of the thin film of Co_3CuN	76
4.10	Thickness of CCN film ~ 40 nm.	77
4.11	Shifting of XRD peak of CCN film on LAO substrate.	79
4.12	The Raman spectrum of Bulk CCN, LAO substrate and CCN film	80
4.13	The Raman spectrum overlap of LAO substrate and CCN film	81
4.14	XPS spectra of the CCN thin film (a) Co 2p , (b) Cu 2p and (c) N 1s.	82
4.15	XPS spectra of the bulk CCN (a) Co 2p , (b) Cu 2p and (c) N 1s.	83
4.16	Resistance vs Temperature or RT plot.	84
A.1	Equipment used in solid-state synthesis	91
A.2	Autoclave	92
A.3	Sealed glass tube	92
A.4	Battery Components (From internet)	96

List of Tables

2.1	Energy difference(ΔE) between the different magnetic orders of Fe ₃ SnC from the lowest energy FIM ordering.	40
2.2	Optimized lattice parameters of lithiated Fe ₃ C and Li ₀ Fe ₃ SnC	41
2.3	Contribution of up and down spin of electrons at the Fermi level into the magnitude of spin polarization for Fe ₃ SnC.	44
2.4	Contribution of up and down spin of electrons at the Fermi level into the magnitude of spin polarization for Fe ₃ C.	45
3.1	Comparison table of capacity between perovskite and antiperovskite as an anode material for Li-ion battery	64

Abstract

In recent years there is a significant interest in developing and exploring new and efficient functional materials for emergent energy applications. Such applications include individually tiny energy-consuming device operations but are necessarily implemented on a very large volume such as advanced computer chips and sensors for the Internet of Things (IOT), batteries for electric mobility, grid-scale power handling, and storage. Towards this end, in this work, we have focused on two classes of materials, namely antiperovskites and chalcogenides, which are endowed with interesting set of physical properties in view of their unique structures and chemistry. We have chosen two antiperovskites Fe_3SnC and Co_3CuN as representative cases for battery and spintronic (IOT) applications and interface between antiperovskite nitride and perovskite oxide as an emerging hetero-interface material for its diverse functionality applications. We have combined theoretical as well as experimental work so as to generate a comprehensive understanding about the basic functionality (structure-chemistry-property relationship) of these materials and how the same unfolds in real applications in each case.

Chapter 1

A key notion defining the progress of the emergent fields of modern electronics, renewable energy, and smart systems is “charge storage” which is primarily embodied in various battery chemistries and systems. In addition to the “charge” property, the electron also has the “spin” property which is exploited in the field of “spintronics” to access novel magnetically controlled device actions that are not accessible to conventional electronics. An interesting question is whether the two can be fruitfully integrated into a single device concept to expand the horizon of device design and applications. Herein, we present a combined experimental and theoretical study of virgin and lithiated conducting intermetallic anti-perovskite with nominal stoichiometry represented as $\text{Li}_x\text{Fe}_3\text{SnC}$ ($x = 1, 2, 3, 4$) to establish the principle of reversible and concurrent charge and spin polarization storage that can be aptly christened as Iono-Spintronics representing a notion of Spintronic Battery. The experimental results however showed that lithiation turns the system into a biphasic state comprised of tin-lithium alloy (due to high affinity of Sn for Li) along with lithiated Fe_3C ; the process exhibiting multiple cyclability (rechargeability).

Chapter 2

Surface modified antiperovskite nitride Co_3CuN with high specific capacity have been studied as high-performance anodes for Li-ion storage devices. Herein, an antiperovskite Co_3CuN was prepared via the hydrothermal method followed by calcination in the NH_3 atmosphere. A surface modified Co_3CuN ($\text{Cu}_{1-x}\text{NCo}_{3-y}/\text{CuFeCo}$) was also designed and studied as an anode material for Li-ion battery (LIB), the material was noted to deliver a reversible capacity of 1150 mAhg^{-1} at a current density of 0.1 Ag^{-1} whereas pure Co_3CuN showed the reversible capacity of 408 mAhg^{-1} at a current density of 0.1 Ag^{-1} . It also exhibited very good retention of the initial capacity of surface reconstructed Co_3CuN after 350 charge-discharge cycles which is more than 62% retention of capacity at 0.1 Ag^{-1} . Finally, the Li-ion full cell performance of surface reconstructed Co_3CuN was studied using $\text{LiNi}_{0.5}\text{Mn}_{0.3}\text{Co}_{0.2}\text{O}_2$ (NMC-532) as a high-capacity cathodic counterpart, which showed a very high reversible capacity of 600 mAhg^{-1} (based on the anode weight) at an applied current density of 0.1 Ag^{-1} with 35% retention of capacity after 100 cycles. This work offers new promising strategies to improve a higher reversible capacity of antiperovskite as an anode material for Li-ion battery applications.

Chapter 3

In the 3rd chapter, we have addressed the epitaxial heterostructure interface of thin-film between nitride antiperovskite and oxide perovskite by a physical deposition process using the Pulse laser deposition technique (PLD). Designing and growing the antiperovskite and perovskite heterostructure and exploring the corresponding interface properties is an interesting but challenging task due to their complex structural surface phase(s) and dissimilar chemical character. Herein, we report the growth of epitaxial heterostructure interface of magnetic intermetallic antiperovskite nitride Co_3CuN (CCN) on the non-magnetic insulating metal oxide single crystal substrate of LaAlO_3 (LAO) by using the physical thin film deposition technique of Pulsed Laser deposition or PLD. PLD is a well-known method of film growth in the field of oxide epitaxy because of its natural strength of true stoichiometry transfer from a single sintered target to the film. Its applicability to the growth of an intermetallic like CCN entails an optimization effort.

Chapter 1

Introduction

1.1 Importance of renewable energy and its sources

Pollution is rampant everywhere worldwide, and it emanates from various sources such as road transportation, waste drainage water, industrial waste products, usage of fossil fuels (coal, natural gas, and Oil), and many others such as direct and indirect polluting sources of energy. Pollution creates many serious side-effects on our planet which lead to increased frequency and strength of natural disasters such as floods, tornados, cyclones, and storms. Pollution also vastly affects the globe by increasing the CO₂ emission and thereby the temperature across the globe. This also increases the seawater level by melting ice. It also significantly affects our well-being and health as well as the health of flora and fauna. It also helps grow and spread infections causing a variety of diseases by creating conditions favorable for the growth of micro-organisms. The sources and impact of pollution are presented below in [Figure 1.1](#)

To get rid of the pollution, we need to stop using the sources of pollution such as fossil fuels as our primary sources of energy and move to other clean and green energy sources and these are sunlight, wind, rain, biomass, geothermal, and tidal energy, etc. All these energy sources are known as renewable energy sources and are presented in the figure below [Figure 1.2](#)

Since the character of renewable and green energy sources is distinctly different than that of the high energy density fossil fuels such as coal, petrol, diesel, etc. we need to develop new concepts and device architectures to harvest them efficiently. There are various avenues for intelligent and effective use of different green energy sources, but they invite fundamental changes in our thinking about the whole ecosystem development for responsible energy utilization. Materials innovation compounded with the scalability of

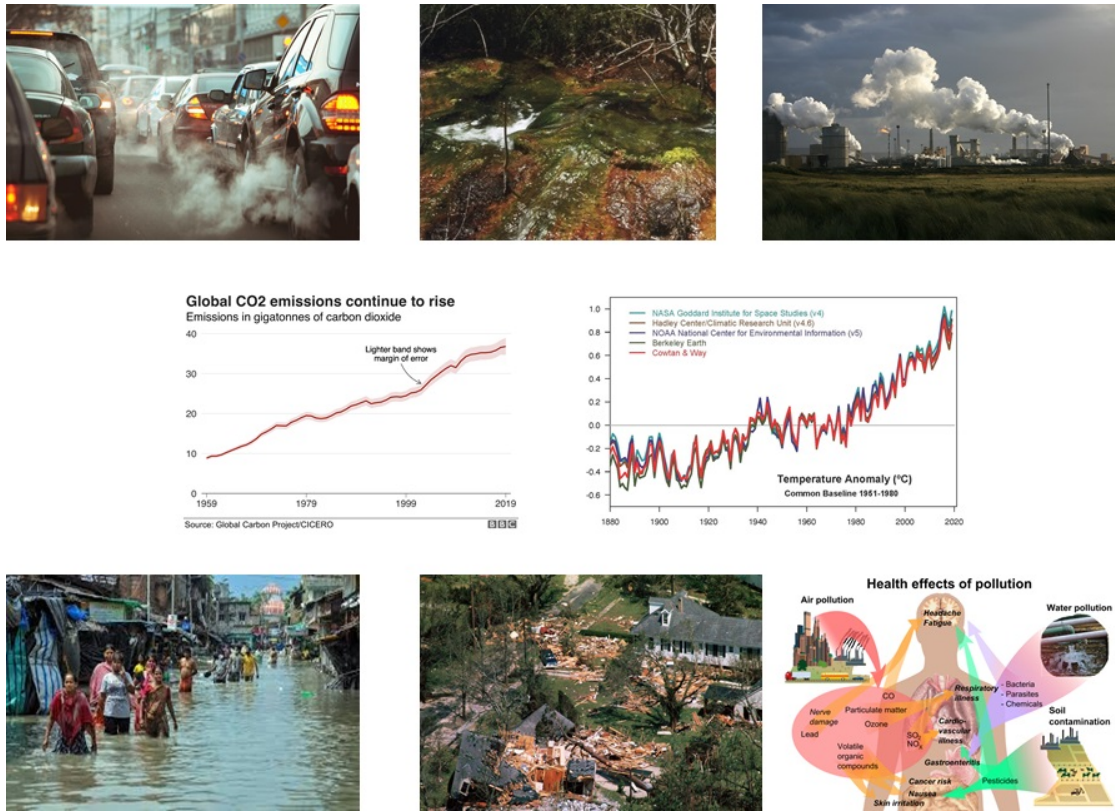


FIGURE 1.1: Source of pollutions and it effects

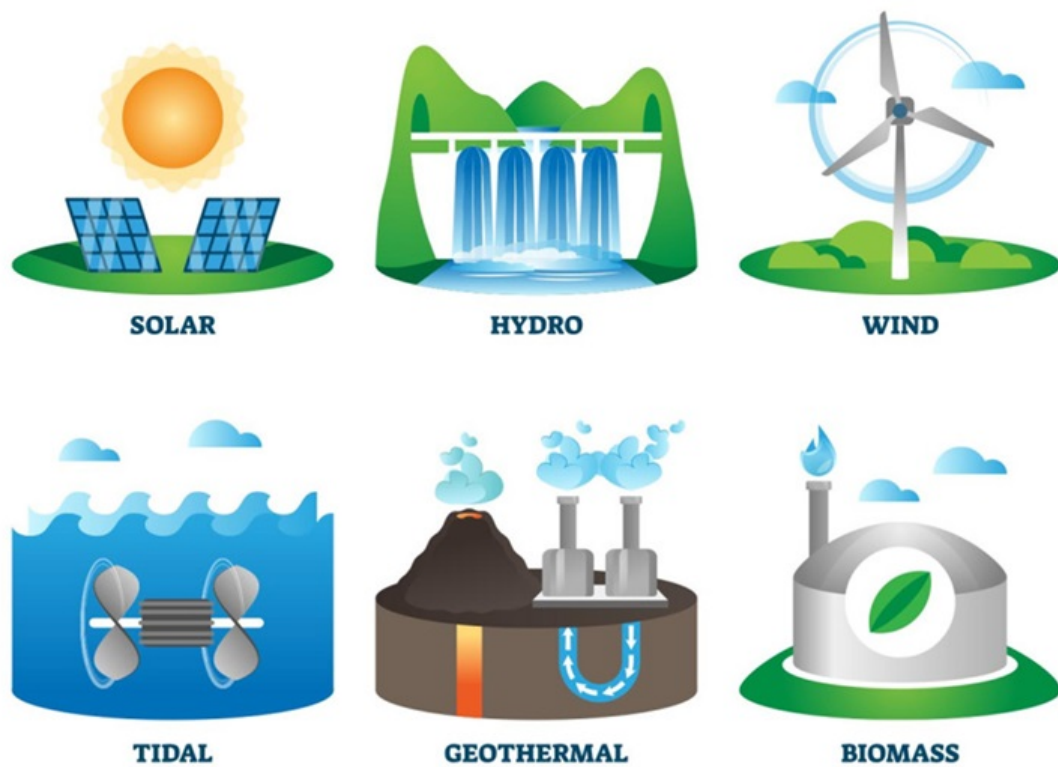


FIGURE 1.2: Different renewable energy sources

implementation holds the key to the success of this frontier which involves renewable energy harvesting, storage, and conservation.

In the changing world, our needs for transportation and communication have been growing very rapidly and these are highly energy-consuming. Major progress is expected in these sectors on the energy utilization front by way of electric mobility and things becoming smatter and faster based on AI, ML, robotics, and the internet of things (IoT). One soon expects to have smart cities, hospitals, factories, highways, etc. all around us with everything everywhere connected to cloud storage.

1.2 Status of energy in the world and its utilization

In the developing countries of the world, the usage of energy continues to grow as shown in Figure 1.3. Global energy demand has tripled in the last 50 years and could triple again in 30 years. While much of this growth will come from the fast-growing economies of China and India, many developed countries, especially in Europe, are hoping to meet their energy needs by expanding their use of renewable sources. Currently, only a small percentage of renewable energy, especially wind energy, is being used, and a significant expansion of the use of all types of renewable energy is needed and expected. For example, Germany plans to meet its 20% electricity and 10% overall energy needs with renewable resources by 2020. Energy is an essential obstacle to the rapid economic growth of China and India. In 2003, China surpassed Japan as the world's second-largest oil consumer. However, one-third of it is imported. Unlike most Western countries, coal dominates China's commercial energy resources, accounting for 2/3 of its energy costs. In 2009, China surpassed the United States as the largest generator of CO₂. In India, the primary energy resources are organic matter (wood and dung) and coal. Half of India's oil is imported; about 70% of India's electricity is generated by highly polluting coal. Nevertheless, significant progress is being made in the renewable energy sector in most countries. India has a rapidly growing wind power base and has one of the most comprehensive solar cooking programs globally.

1.3 Future demand of energy

Over the next decade, India is set to leap toward adopting renewable energy sources to meet its growing energy needs. For example, the Government of India aims to rapidly transform the clean energy landscape of India (Figure 1.4) with the installation of 175 gigawatts of solar and wind power by 2022. Although both solar and wind energy

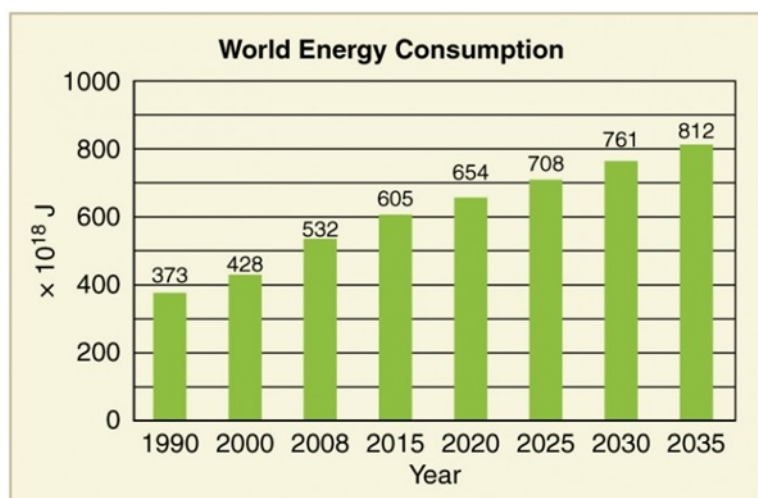


FIGURE 1.3: Past and projected world energy use (source: Based on U.S. Energy Information Administration, 2011)

benefits have reached economically viable price points, the break-in energy production from these sources is a significant obstacle to their adoption. Therefore, it will be essential for India to adopt the planned renewable energy sources to manage technoeconomically electric power storage. A related but distinctly ambitious national agenda is the mass market electrification of transport. It is noted that by 2030, 60 million vehicles in India should be electrically powered (Global Energy Outlook 2017 by IEA). This is a difficult task as only 4,800 electric vehicles are on the road in India till 2016. While the adoption of renewable energy sources for grids, the widespread adoption of electric vehicles is also limited by the economic efficiency of electrical energy storage. Nothing comes from anything. This fact about seemingly abstract concepts like "energy" can easily be forgotten. More solar panels, wind turbines, electric vehicles, and larger batteries mean more clean energy. Even so, the above implies a greater requirement for the materials which enable those technologies (Figure 1.4). Innovative materials with enhanced efficiency can improve energy productivity and productivity. Innovative materials will enable energy savings in energy-intensive processes and applications, as well as open up new design possibilities for renewable energy generation. Advances in physics and engineering are needed to allow these new capabilities. Many R&D portfolios follow promising materials technologies that offer the potential for significant energy savings.

1.4 New materials for energy storage applications

Since the discovery of the voltaic pile in 1799 development of new novel electrode materials for batteries has continued over the last couple of centuries and the pace of the

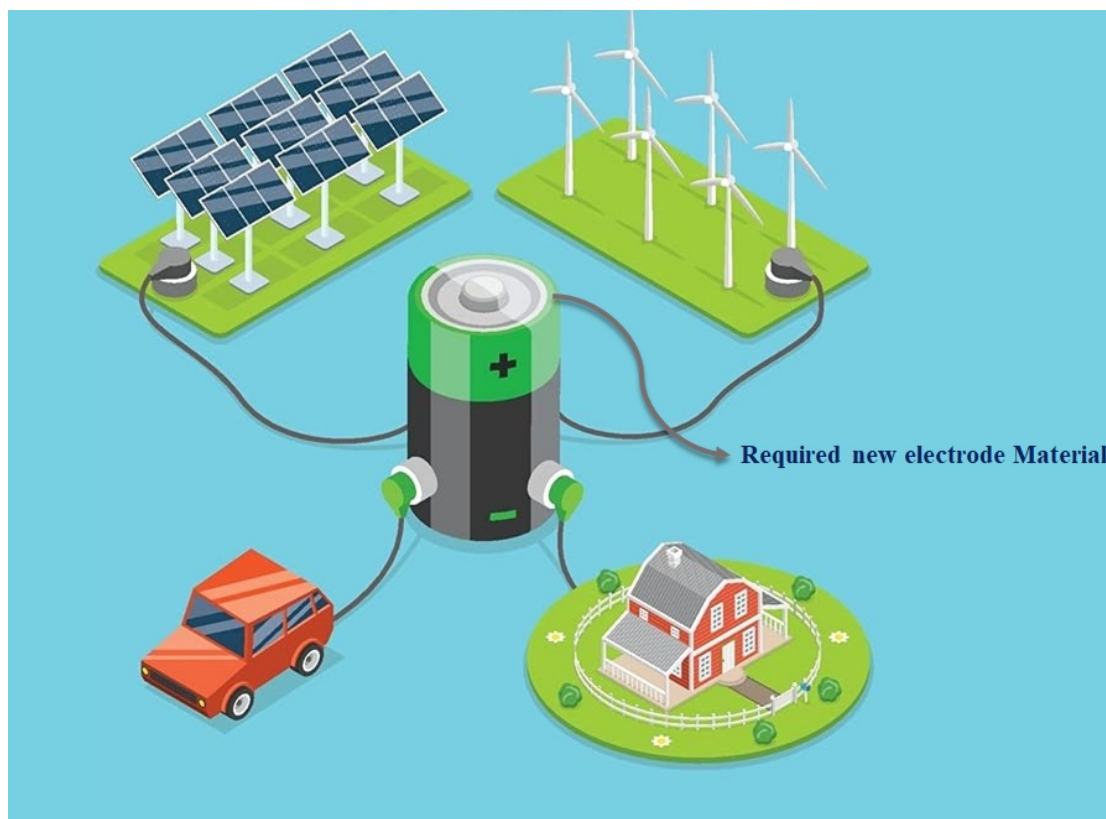


FIGURE 1.4: Requirement of new electrode materials for energy storage from different renewable sources (wind, solar, etc.)

same has been accelerating. Several battery chemistries have been discovered over this period such as Lead-acid (1859)[5–8], Nickel-cadmium (1899)[9–11], Nickel iron (1901) and Nickel Zinc (1932) [12–14], Rechargeable alkaline (1950), Nickel hydrogen (1977), Vanadium flow battery (1986), Nickel-metal hydride (1990) [13], Lithium cobalt oxide LCO (1991) [15, 16], Sodium sulfur (1993) [17], Lithium iron phosphate LFP (1996) [18], Nickel cobalt aluminum oxide NCA (1999)[18], Lithium Manganese oxide LMO (1999) [19], Lithium titanate LTO (2008) [18], Nickel manganese cobalt oxide NMC (2008) [18], Lithium-sulfur (2008) above all these batteries oxide (cathode) and carbide (graphene) based batteries are dominating the world commercial market based on its energy density, stability, and good cyclic stability [20].

Due to the high population growth in the last few decades, world energy use has been steadily increasing. Greater energy storage and conversion devices are urgently necessary to reach human life's basic needs. Traditional energy-saving materials and devices are based on either lithium-ion batteries or perforated carbon (electric double layer). Conducting polymers, supercapacitors and pseudocapacitors have also entered the energy-saving systems to improve the battery system. The Li-ion battery (LIB) was introduced by Sony Corporation in 1991 and has since transformed portable electronic

devices. While the new-generation Li-ion battery can drive electric vehicles within a limited driving range while charging, it is still a long way from reaching the 500-kilometer target. Li-ion batteries have various defects associated with the reaction of lithium metal electrodes that lead to the formation of dendrites which can affect the life of the battery cycle. The specific energy concentration of the current sophisticated LIB is below that of the United States.

Department of energy vehicle technology program's long-term target for secondary batteries [21]. Similarly, the volatile organic electrolytes of LIB have raised safety concerns. These drawbacks in LIB have led to the development of new stable liquid electrolyte, solid polymer electrolyte (SPE), and solid-state electrolyte (SSE) systems that inhibit dendrite growth and improve its practical, specific energy capacity, energy density, and power efficiency. Most of the research thus far on materials aspects has been intensely focused on different structural materials to improve their storage capability and performance, such as layered, spinel and olivine, and perovskite systems. All these structures and their atomic environments help host the guest atom (like Li, Na, etc.) and improve the storage capacity.

In this thesis, the study has focused on a new structural material system called "Antiperovskite." This is a twin brother of the ubiquitous perovskite-type material, where the cation and anion positions are inverted, as discussed later. In this thesis, we have explored this antiperovskite material (in their carbide and nitride forms) for its application as an anode material for energy/charge storage in Li-ion batteries (LIB). Interestingly these antiperovskite materials systems we have explored are intermetallics and have intrinsically good electrical conductivity bringing the corresponding advantages to their efficacy for battery anode application. Separately, we have also studied the effect of electrochemical lithiation on the magnetic properties of antiperovskite materials such as magnetization and spin polarization, the latter being essential for spintronics wherein the electron spin plays a crucial role. Indeed, spintronics is based on offsetting spin-up and spin-down concentrations of itinerant electrons at the Fermi level. Thus, we have examined the possibility of lithiation-induced manipulation of the up and down spin concentrations bringing in a conceptually novel scheme of iono-spintronics or a spintronic battery which could significantly impact the next generation data storage system designs. The structural details and critical implications of the antiperovskite class against the well-studied perovskite class have been discussed in the following sections.

1.5 Perovskites and Antiperovskite materials

For the last 20 to 30 years, perovskite materials have played a humungous role in every field of science and technology and dominated the world in material space. Due to their multidimensional properties, they have always attracted significant attention in research and applications. High-temperature superconductivity, ferroelectricity, piezoelectricity, and multiferroicity are all these examples of different properties that have been observed especially in oxide-based perovskites (ABO_3). Due to the flexibility of coordinating with neighboring species or elements, these materials possess different dynamics during many reaction processes from classical to quantum mechanical effects and effects of external stimuli like temperature, electric or magnetic field, etc.

Perovskite belongs to various crystal types such as cubic, orthorhombic, and hexagonal, and they also exist in different dimensions such as 2D, 3D, etc [22–24].

Antiperovskite materials have not been as much explored as the perovskite materials, but they also possess exciting properties like perovskites and these are: Superconductivity, Thermoelectric properties, Energy storage capabilities (used as solid states electrolyte, cathode, etc.), very good electrocatalytic activity, etc. which will be discussed in the later section. Antiperovskites also have different crystal structures like perovskite such as cubic, orthorhombic, hexagonal, etc., and they also support crystal structures of different dimensions such as 1D, 2D, and 3D [25–28]. All the explored fundamental properties of antiperovskite materials, and how the cation and anion exchange change the chemical environment and related chemical properties as compared to the well-known perovskite materials are discussed in the flowing sections.

1.6 The fundamental difference between perovskites and antiperovskite

It is very important and exciting to first discuss and explore the fundamental differences between the perovskite (ABX_3 , where A= cations, B= cations X= anions) and antiperovskite (X_3AB , where X= cations, A= cations, B= anions) materials. The exchange of positions of cations and anions is the leading cause that differentiates the fundamental properties such as electric, magnetic, optical, and mechanical between the perovskites and antiperovskites. The basic structural difference between perovskite and antiperovskite is presented in Figure 1.5. Most of the natural and fundamental elements in the periodic table contribute to the formation of skeletons for both the perovskite and antiperovskite structures (Figure 1.5).

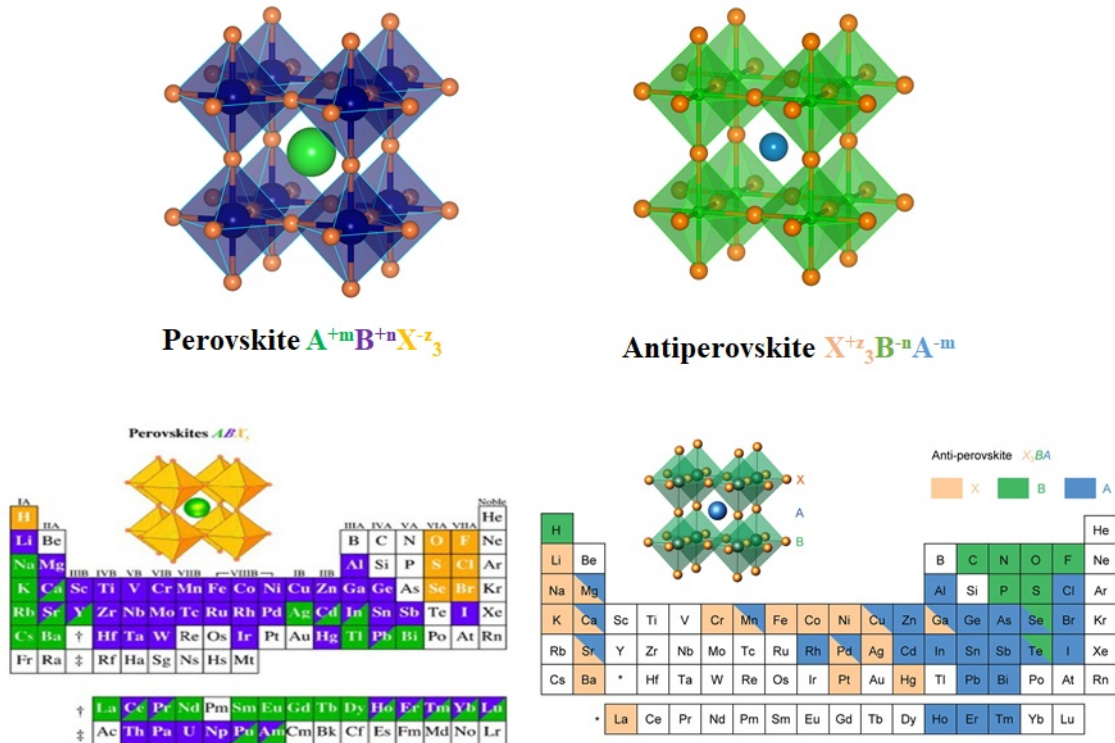


FIGURE 1.5: Structural information of both perovskites and antiperovskite

The proper chemical charge balance of the cations (A, B) and anions (X) is completely satisfied in perovskites whereas for the antiperovskite materials an unusual charge balance is observed between the cations (X) and anions (A, B) [29–31]. It was observed that the A-site elements in antiperovskite such as Al, Zn, Sn, In, etc., technically carry a -ve charge which is very much unusual case [32].

To better understand the effect of cation and anion positions in both the perovskite and antiperovskite and their real exciting impact on different physical and chemical properties, we discuss here a few examples of compounds consisting of the same elements with different stoichiometry but which can exist in both the perovskite and antiperovskite structures such as $ASnO_3$ and A_3SnO where A is Ca, Sr, and Ba respectively. Figure 1.6 represents some Antiperovskite and Perovskite materials.

Crystal structure, symmetry, and space group of A_3SnO and $ASnO_3$ [31, 33, 34] could be the same or different depending on the synthesis conditions and processes of these compounds respectively. It has been observed that A_3SnO has only one stable phase with cubic symmetry and the corresponding space group number is Pm-3m (221) but on the other hand, the $ASnO_3$ material could exhibit a series of phases depending on the synthesis mechanism and growth condition like pressure, temperature and etc. It has been observed that for $SrSnO_3$ multiple phases exists with different temperatures such as the structural or phase transformation occurs from the room temperature structure

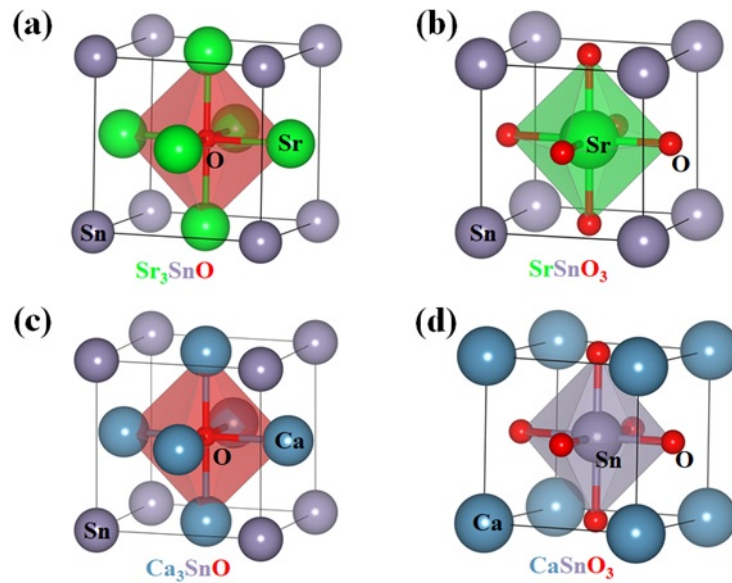


FIGURE 1.6: (a) Antiperovskite, (b) Perovskite, (c) Antiperovskite, (d) Perovskite

$Pnma$ to $Imma$ at 905K, to $I4/mcm$ at 1062K, and finally to the $Pm-3m$ aristotype at 1295K [35, 36]. With changes in the structure, the atomic environment also changes like tilting of SnO_6 octahedra in $SrSnO_3$ all these phases of $SrSnO_3$ being shown in Figure 1.7 (a-d). But for Sr_3SnO antiperovskite, only one stable cubic $Pm\bar{3}m$ phase exists and Sr_6O octahedral coordination observed (Figure 1.7 (e)).

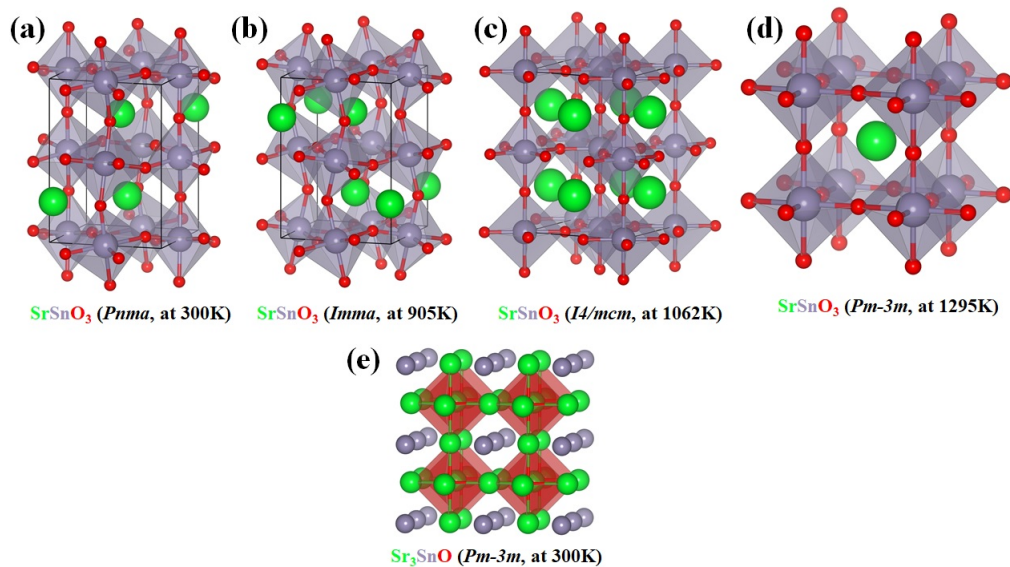


FIGURE 1.7: (a-d) Different perovskite phases of $SrSnO_3$ with SnO_6 coordination, (e) Single antiperovskite phase of Sr_3SnO with Sr_6O coordination.

Following specific Synthesis protocols for perovskites and antiperovskites is very important to realize these materials in a stable form. The synthesis protocol of all normal perovskites of ABX_3 type is easily accessible and there is no need for

use of vacuum and high-temperature conditions. For antiperovskite materials X_3AB , the synthesis protocol is quite hard and challenging because the switching between the cation and anion (like $ASnO_3$ to A_3SnO) leads to the requirement of high pressure and temperature conditions. Indeed, the synthesis process of antiperovskite material involves heating under a sealed evacuated quartz tube at a high temperature and many precautions have to be taken [37]. Sometimes it is very hard to achieve the exact phase of the antiperovskite crystal as compared to perovskite crystal, but it is achievable.

Electronic, magnetic, optical, and mechanical properties of both perovskites and antiperovskites are very interesting depending on the positions of cations and anion and their behavior could differ dramatically from each other. It has been reported that the electronic properties of $ASnO_3$ perovskite and A_3SnO is majorly different. $ASnO_3$ behaves as a high indirect bandgap material. For example, $SrSnO_3$ has an indirect bandgap of 3.70 eV [38–40], while antiperovskite A_3SnO is reported (theoretically) to be either metallic or semiconductor with a very small direct bandgap. For instance, Sr_3SnO has a direct bandgap of value 0.1 eV [31, 41]. Since the difference in their electronic bandgap is basically due to the orbital overlap strength between the O-2p and Sn-5p orbitals for both the perovskite and antiperovskite systems, it suggests that the antiperovskite A_3SnO could behave as a very good electrical and thermal conductor as compared to the $ASnO_3$ perovskite.

In A_3SnO the metallic concentration (Vs oxygen) is high as compared to $ASnO_3$ and this leads to the less ionic bond character in antiperovskite vis a vis the perovskite material and this property helps reveal that the antiperovskite materials are brittle whereas $ASnO_3$ is ductile. In $SrSnO_3$ the presence of SnO_6 octahedral coordination and low metallic concentration (1:1) lead to high bandgap and ductility as compared to Sr_3SnO where the metallic concentration is high (3:1) and Sr_6O octahedral coordination helps to reduce the bandgap and improve all electronic properties. Both $ASnO_3$ perovskite and A_3SnO antiperovskite carries multiple properties due to their exchanged positions of cations and anions and they could access different application areas in the different fields of science and technology. Similarly, antiperovskite carbides and nitrides have attracted great attention in research academia, and industry. In this thesis, we will specifically discuss the properties and applications of some interesting antiperovskite carbide and nitride systems.

As discussed above, the crystal structure of both the perovskite (ABX_3) and the antiperovskite (X_3BA) defines their crystal symmetry (such as octahedral symmetry of BX_6 in perovskite and X_6B in antiperovskite) in the bulk and on the truncated surface, thereby playing a fundamental role in many of their properties such as magnetism, catalysis, etc. It is a well-known fact that e_g filling of 3d orbitals and position of the d-band center

are the important descriptors/fingerprints to describe the binding strength between the molecules (like H_2O , CO_2 , NH_3 etc) with the corresponding crystal facet (such as 100, 110, and 111 surfaces). By engineering the crystal surface in different ways such as creating defects or doping or substituting different elements it is possible to enhance the many desired properties of the system.

Figure 1.8 describes the difference between the 3d orbital splitting of transition metal (TM) for octahedral symmetry of both the bulk and the surface of the perovskite and antiperovskite materials

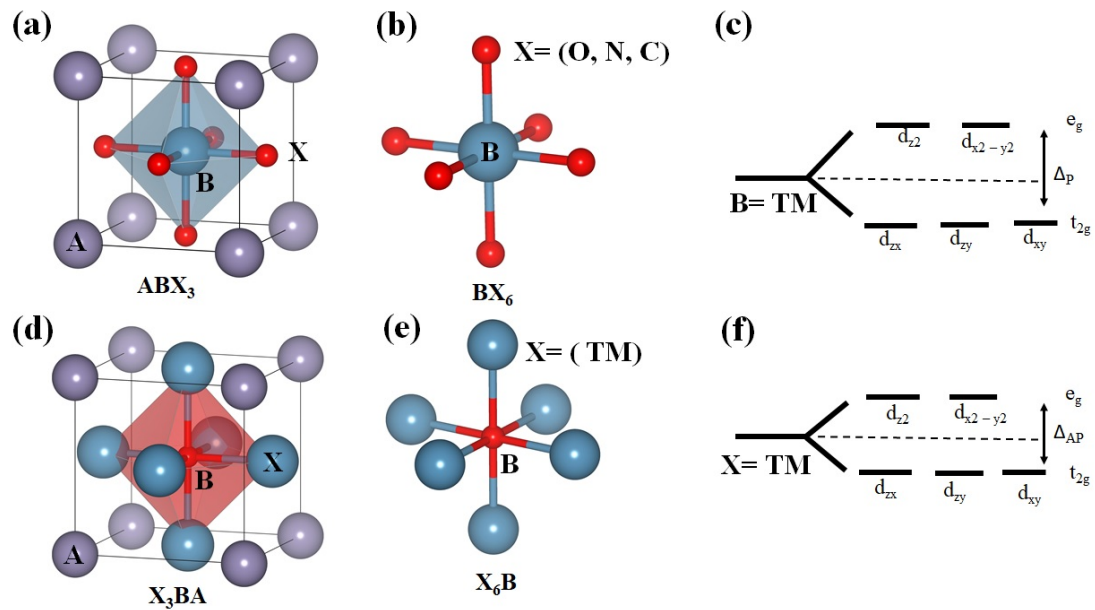


FIGURE 1.8: 3d orbital splitting of bulk perovskite (ABX_3) and antiperovskite (X_3BA).

In the perovskite the BX_6 octahedral co-ordination (Figure 1.8 a) the cation B TM atom co-ordinated with the six anion O atom (Figure 1.8 b), so the five 3d orbital of TM atom and O atom orbital will make strong overlap. Due to electrostatic coulomb repulsion and pouli repulsion, the orbital gets split with two different orbitals e_g and t_{2g} and the energy gap between them is Δ_P (crystal field energy “P” used for Perovskite system) (Figure 1.8 c).

Depending on the strength of the crystal field energy of different local crystal coordinations such as octahedra and tetrahedra, the important aspects of the “high spin” and “low spin” states of any material can be understood. In the case of antiperovskite with X_6B octahedral co-ordination (Figure 1.8 d) the anion B (C, O, and N atom) makes sixfold coordination with the six nearest neighbor transition metal ions (Figure 1.8 e). Therefore in an antiperovskite, a single anion B interacts with six TM atoms so the Coulomb repulsion due to the electron cloud of the orbitals is less as compared to the perovskite, where one single TM ion is coordinated with six anions. So, in an

antiperovskite, the five 3d orbitals will split (e_g and t_{2g}) but the crystal field energy gap Δ_{AP} (“AP” denotes Antiperovskite) will be small as compared to Δ_P . Since $\Delta_{AP} < \Delta_P$ most of the antiperovskite materials will carry the “high-spin” (more number of unpaired electrons) properties. This also suggests that the ionic character of the TM-X ($X=O, N, C$) bond for perovskite materials is large and as a result, most of the oxide perovskite materials exhibit a larger energy bandgap whereas for the antiperovskite the ionic character of B-X ($B=O, N, C$, and $X= Fe, Ni, Co$, etc.) bond is less and most such antiperovskite materials are either conductors or exhibit only a very small energy bandgap.

It is very interesting to understand the crystal surface of both the perovskite and antiperovskite. For every crystal structure, the crystal symmetry is lost at the surface. This loss of symmetry helps in many fundamental applications, especially in electrocatalysis-type applications. More number of active sites on the surface of any crystal enhance the performance of the catalyst. The presence of a large number density of TM atoms on the surface could also enhance the catalytic performance. For antiperovskite, the surface accommodates a high density of TM atoms (Figure 1.9 (e)) as compared to the perovskite materials as shown in Figure 1.9 (b).

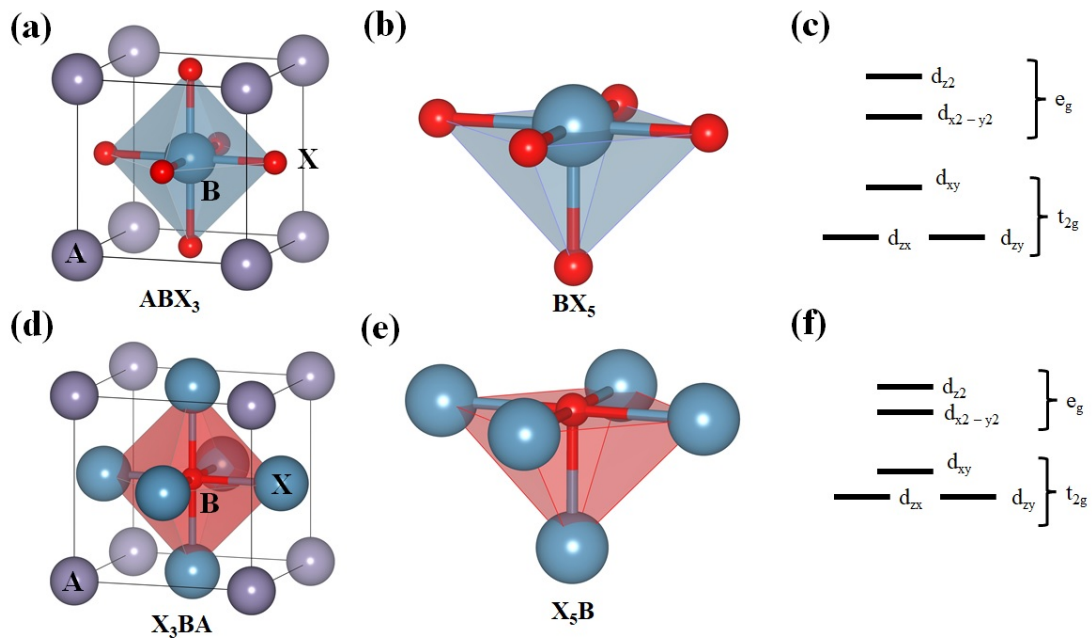


FIGURE 1.9: 3d orbital splitting of perovskite (ABX_3) and antiperovskite (X_3BA) at the surface.

Due to the loss of symmetry at the surface, the 3d orbital splitting (Figure 1.9 c and f) will become different as compared to the bulk crystal system. Thereby it opens itself up for designing or engineering a surface and enhancing many interesting properties and performance features of the corresponding materials. Other important property

differences between the antiperovskites and the halide or chalcogenide perovskites have been discussed by Yuan et al. and presented in Figures 1.10 and 1.12. It suggests an electronic inversion of the element between the perovskites and the antiperovskites building property differences between them [1].

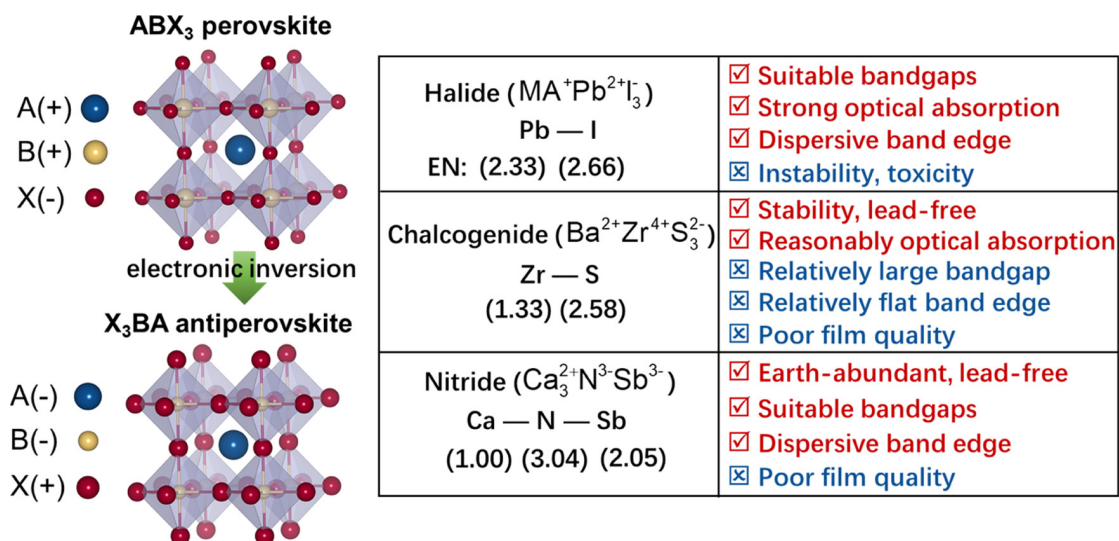


FIGURE 1.10: Structure and properties of halide and chalcogenide perovskites compared to those of the nitride antiperovskite [1].

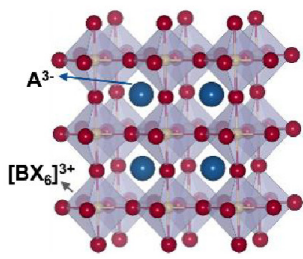
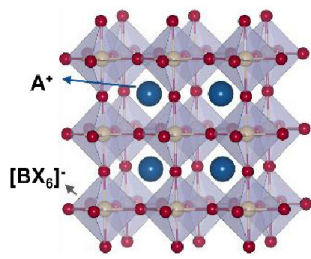
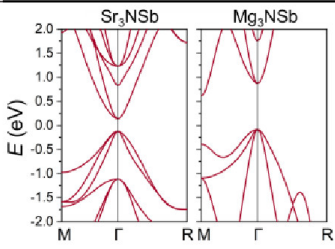
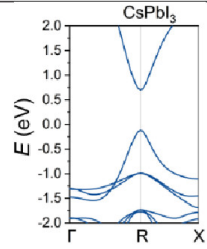
	3D antiperovskite X_3BA	3D halide perovskite ABX_3
Crystal structure		
Material example	$A^{3-} = P^{3-}, As^{3-}, Sb^{3-}, Bi^{3-}$ $B^{3-} = N^{3-}$ $X^{2+} = Mg^{2+}, Ca^{2+}, Sr^{2+}$	$A^+ = MA^+, FA^+, Cs^+$ $B^{2+} = Pb^{2+}$ $X^- = Cl^-, Br^-, I^-$
Synthesis	Reaction tube (~ 800 °C)	In solution (~ 100 °C)
Processing methods	sintering, sputtering	CVD, sputtering
Sample types	Powder, thin film	Single crystal, thin film
Typical band structures		
Band edge's main contribution	CBM X d/s VBM A p + B p	CBM B p VBM B s + X p
E_g (eV)	0.70-2.48	1.40-3.21 ^{48, 49}
m_h (m_0)	0.26-0.98	0.14-0.31 ^{48, 50}
E_b (meV)	4-65	14-68 ⁵¹
Optical transition	Allowed	Allowed
Y (GPa)	90.10-181.48	17.79-21.92 ⁵²
Brittleness/Ductility	Brittleness	Ductility

FIGURE 1.11: Comparison of the physical properties between the 3D antiperovskite and 3D halide perovskite [1].

1.7 All other properties of Antiperovskite materials

In the current world scenario of development, there is always a demand for new exciting functional materials with novel physical properties for diverse emergent fields of application interest. Perovskite is one such class of materials that has dominated over the last 30 years or more in almost every area of science and technology. Antiperovskite is also a promising functional material but has not been explored as much as the perovskites, although it has an interestingly different set of functionalities.

Antiperovskite is like a twin brother of the perovskite structure with the general formula ABX_3 for perovskite and X_3BA for Antiperovskite. There are several Bravais crystal types of perovskites and antiperovskites. In this thesis, we have focused only on the 3D simple cubic antiperovskite system, which belongs to the space group of $Pm\bar{3}m$ no. 221. In perovskite, the anions on the face center make BX_6 octahedral coordination. The beauty of this coordination impacts most of the properties of the fascinating and crucial material.

In contrast, in antiperovskite materials, cations make X_6B octahedral coordination, making antiperovskite differently more exciting as the bonding character is characteristically different. Like perovskite, different chemical phases can occur in an antiperovskite, such as a carbide, oxide, nitride, sulfide, or halide [42]. All these systems have other functional properties, making them more attractive to the research community. All these individual antiperovskites with different chemical phases have many applications in various fields, such as superconductivity [32, 43–56], thermoelectric [34, 57–68], electrocatalytic [69], optical [70–72], magnetoresistance [42, 73–77], solid-state electrolyte [3, 78–81], solar cell [1, 59, 82–84], topological insulator [85–88], ferroelectric [89, 90] and energy storage system like alkali ion battery, etc.[3]

Since the discovery of the antiperovskite in 1930, various researchers have shown their potential for applicability in the different fields, as derived from their rather unique material properties. Normal perovskite has ionic bonds [91]. Still, for antiperovskite, various metallic, ionic, and covalent bonds are observed, which make antiperovskite a functionally intriguing material.

Perovskites were invented in 1839 by the Russian mineralogist L. A. Perovskite [92]. Perovskites play important role in solid-state chemistry and physics (Pena and F.) due to the numerous essential features that support the functioning of the current advanced world, such as superconductivity, multiferroelectricity, ferroelectricity, magnetism, and It can also be used as a catalyst and a battery material. The discovery of an organic-inorganic hybrid perovskite that can be used as a photovoltaic material has sparked a surge in perovskite research. The formula ABX_3 can also describe an antiperovskite but

is electronically reversed (where X is denoted as cations and A, and B denoted as anions, which could be written as X_3BA) [27, 73, 93–96]

The antiperovskite in principle shares the advantages of perovskite-type structure with traditional perovskites accommodating diverse elements to form a large family of functional materials from a structural chemistry standpoint. Though antiperovskite has a number of intriguing properties, including superconductivity, negative thermal expansion, ionic and electronic conductivity, magnetism and etc. As a photoluminescence host material antiperovskite also play a significant role. Several of these recent exciting discoveries are likely to spur a new round of functional antiperovskite development. We can also consider whether and how we might be able to structurally develop an antiperovskite that is equivalent to perovskites in order to enhance the performance or to achieve some surprising results.

As we have discussed earlier the antiperovskite of formula X_3BA , where the X behave as a cation, and the remaining A and B behave as an anion of different sizes. The perfect antiperovskite architecture is tightly packed and belongs to the $Pm\bar{3}m$ space group. The B ions are centered in the six-fold integrated octahedra, while the A ions are 12-fold embedded with the X cations. The octahedra structure's 3D skeleton is formed by corner-sharing BX_6 and the cations in the octahedra of perovskite replace with anion in antiperovskites. The presence of the rich amount of TM metal in the X-site caches antiperovskites with obsolete physical and chemical properties related to d-spin states or band structures with attractive ionic transport properties. Figure 1.5 shows the basic elements of the antiperovskites known so far, typically, monovalent or divalent cations are situated at the X site and small anions are positioned at the B site. Some of the converted metals A and X can behave as both components depending on the relative ionic radius and electrical negativity, which is uncommon in traditional perovskites.

At first sight, the antiperovskite appears to contain roughly half of the elements in the periodic table, however, the published antiperovskites frequently contain no more than ten components. In comparison to the vast potential represented by the basic periodic table (Figure 1.5), the number of antiperovskite compounds is insignificant. As a result, antiperovskite research is still uncommon, with fewer than fifty research papers published each year due to the small number of antiperovskite studies. The concept of "anti" is not widely accepted, at times, newly discovered antiperovskite are considered intermetallic compounds or dual-metal nitrides/carbides, often overlooking the consequences of their exceptional structure and properties. Nonetheless, the significance of antiperovskite exceeds expectations.

For perovskites, the tolerance factor (t) has been introduced to determine their geometrical crystallographic stability and possible structural symmetry, and the factor t is defined by the equation: $R_A + R_X = \sqrt{2}(R_B + R_X)$

here R_A , R_B , and R_X denoted as the ionic radius of the equivalent ions. Most of the cases it has been observed that when the range of t value is within the range of 0.85 to 1.0 then the observed possible crystal structure is cubic symmetry and if the value of t lies less than 0.85 then lower crystallographic symmetry is expected which is observed in tetragonal or orthorhombic structural symmetry.

Similarly, for the antiperovskite of X_3BA , the formula of the tolerance factor t is equally valid and very much useable to define the crystal symmetry. In the formation or the construction of antiperovskite materials most of the cases p orbital based elements such as Al, Ga, and Ge preferred to form the covalent bond in the antiperovskite materials whereas the d and f block elements preferred metallic bond. With the help of interatomic bonds, tolerance factor t and R_A/R_B Benzonsikov et al. tried to predict the metallic bond of nitride antiperovskite structure but the practicality and success of the method were not verified [96]. It has been observed that sometimes the t factor does not follow the metallic X_3BA antiperovskite compounds though most of the ideal antiperovskite adopt cubic or pseudo-cubic symmetry [42]. As compared to perovskite, antiperovskite adopts fewer distortion [42].

The distortions in perovskites can always be broken down into a few basic components: (a) octahedra tilting, (b) octahedra distortion, and (c) cation displacement [42]. Tilting of the octahedra often dominates the overall crystal structure, and due to the rotation of the rigid octahedra [97, 98], a total of 23 possible space groups exist. Distortions observed in Cr_3AsN [99] with a typical rotation of Cr_6N and Mn_3NA ($A = As, Sb, Ga, Cu$), which exhibits phase transitions to lower symmetry due to processes of the Mn_6N octahedra, according to Glazer's distortion classification. [100]

The distinct coordinate surrounding of cation X (i.e., the $X-X$ length and linear two-fold coordination vs the 6-fold coordination in perovskites) is one of the most significant basic structural features of antiperovskite X_3BA , which plays an important role in magnetic interaction or crystal field strength. Antiperovskites are also X -rich, which is a notable structural feature. Physical properties like magnetism and ionic conductivity are strongly linked to the antiperovskite's X -enriched portion. The high-temperature superionic conductivity of $NaMgF_3$ and MgF_3 perovskite influenced the breakthrough of superionic conductivity in Li -rich antiperovskite ($LiRAPs$ [101]). As a result, the "electronically inverted" antiperovskite retains the Li_3OA ($A = Cl, Br, I$) perovskite-type structure, allowing Li + superionic conduction to be comparable to F -superionic conduction in $NaMgF_3$ [101]. Lithium-rich (60 percent Li) and lightweight antiperovskite

crystalline solids have been developed. The structural arrangement that is X-rich also gives rise to 3D migration channels of the X ions, which favors high ionic conductivity.

The magnetic exchange within the transition-metal-rich topology of magnetic antiperovskites differs from that incorporated in nonmagnetic skeletons, and a metallic ground state is expected. There are tremendous emerging functionalities of antiperovskite, along with superionic conductivity, superconductivity, magnetism, negative thermal expansion, etc., also, antiperovskite has an excellent capability to perform like a phosphor host and electrocatalyst. The flexibility of manipulating the chemical compositions, especially the cations (basically the transition metal ions) towards improving its performance attracts humungous attention in different research areas, which we discuss in the following sections.

1.7.1 Superconductivity in Antiperovskite

Several Antiperovskite materials of different chemical compositions have shown excellent superconducting properties at low temperatures. To date, the highest T_c Antiperovskite superconducting material is Pt_3SrP at $T_c=8.4K$ [102, 103]. Again Ni content ternary carbide antiperovskite shows a superconducting nature in which Ni_3MgC was the first superconducting material discovered in 2001 of critical temperature $T_c=8K$ [104]. The interplay of magnetic interaction due to partial filling Ni d-states and the transient nature of electrons also the local crystal structure and electron-phonon interactions are responsible for the superconductivity in this kind of material. Effects are still there to achieve the high T_c superconducting antiperovskite materials [32, 43–56]. Sr_3SnO is the first superconducting Antiperovskite oxide of $T_c = 5K$ [32].

1.7.2 Negative Thermal Expansion (NTE) in Antiperovskite

NTE is the thermal expansion behavior that arises in magnetic antiperovskite materials due to the complex interplay of the lattice, electrons, and phonons [105, 106]. Most transition metal antiperovskite NTE properties originate from magnetic interaction during cooling with a significant magneto-volume effect, followed by a first-order transition (MVE). Out of all antiperovskites, manganese-based materials such as Mn_3BA ($B=Ni, Cu, Zn, Sn, Ge; A=C, N$) belong to the NTE family [107, 107–116] due to their excellent electrical and thermal conductivity as compared to ceramic NTE materials such as ZrW_2O_8 [117] Non-magnetic materials can also behave as NTE materials such as Na_3OBr and Na_4OI_2 [118]

1.7.3 Magnetism and Magnetoresistance in Antiperovskite

Antiperovskite of formula X_3BA where X constitutes metallic ions (X=Fe, Ni, Co, Mn, etc.), has X_6B octahedral coordination makes antiperovskite excellent functional materials. This octahedral arrangement of metallic cations makes X-X metallic bonds and X-B covalent bonds. The 3d electrons of metal cations participate in their conduction behavior and the magnetic exchange interaction. On the other hand, X-B covalent bonds form orbital hybridization between the p and d orbitals, which broadens the conduction bands near the Fermi level, driving high conductivity, and making the material magnetized and polarized. Switching cations and anions from the perovskites to the antiperovskite alters the electronic and magnetic properties. Several antiperovskite materials exhibit intriguingly different magnetic properties like giant magnetoresistance (GMR), giant magnetocaloric effect (MCE), and giant magnetostriction (MS). Almost all the transition metal-based antiperovskite are metallic, conducting, and magnetic. The presence of two different types of bonds (metallic and covalent) makes antiperovskite mechanically solid and stable.

1.7.4 Spin-polarization and magnetization of magnetic antiperovskite materials

Spin polarization and magnetization are the fundamental properties of all magnetic materials. The electron carries both charge and spin in which electron charge is responsible for energy storage, all electronic device applications, and all kinds of reactions. Along with electron charge, it carries two different spin moments, up spin and down spin and these two-electron spin moments play the lead role in spin polarization and magnetization. The magnetization and the spin polarization of any magnetic materials are realized from the density of states (DOS) plot but there is a fundamental difference between the magnetization and the spin polarization of any magnetic system. The magnetization is the difference between the total number of spin-up (N^\uparrow) and down-spin (N^\downarrow) states of the electrons from the whole DOS plot whereas the spin polarization is the difference between the spin-up ($N_{E_F}^\uparrow$) and spin-down ($N_{E_F}^\downarrow$) states of the electrons particularly at the Fermi level (E_F) of the DOS. So, depending on the number of up spins ($N_{E_F}^\uparrow$) and down spins ($N_{E_F}^\downarrow$) at the Fermi level the percentage or the degree of the spin polarization changes. The formula to define the spin polarization and magnetization are [119, 120]

$$\text{Spin Polarization } P = \frac{N_{E_F}^\uparrow - N_{E_F}^\downarrow}{N_{E_F}^\uparrow + N_{E_F}^\downarrow}$$

$$\text{Degree of Spin Polarization: (DSP)} = P \times 100\%$$

Magnetization: $M = \int (N^\uparrow - N^\downarrow) dV$; **Over all space**

Depending on the values of the spin polarization (P) we can predict the magnetic order of any materials and these are

if $P = 0$; Paramagnetic

if $P < 1$; Ferromagnetic or Ferrimagnetic

if $P > 1$; Half Metallic

Figure 1.12 represent the different order of magnetization with corresponding P values.

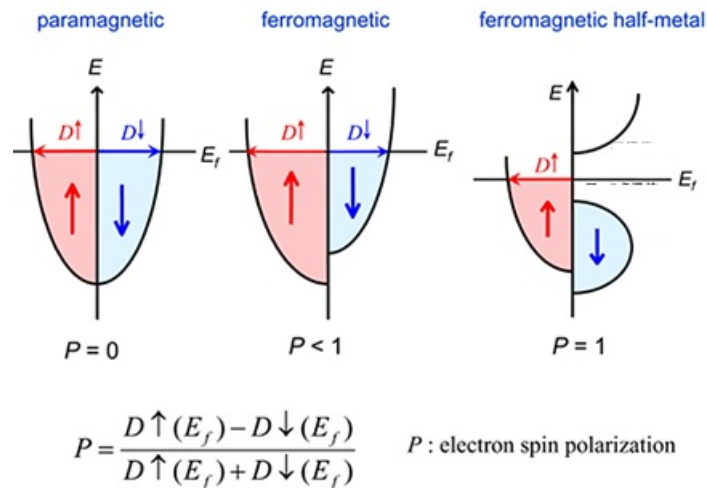


FIGURE 1.12: Spin Polarization of different magnetic Order (internet)

One of the most important concepts is the correlation between spin polarization and magnetization though it has been a mystery [120]. It is assumed that spin-polarized tunnelling currents are proportional to the electron density of the state at the Fermi level. The magnetic moment increases with the number of spin-up electrons, corresponding to a larger spin-up. There is a massive role of electron spin polarization in the applications of solid-state spintronics devices as spintronics has become an important part of science from both its fundamental as well as application point of view since it has a strong potential for emerging technologies. The research in spintronics has brought several novel and promising concepts of advanced electronic devices steered by electric current and/or field with low energy consumption, non-volatile magnetic memories with the ultrafast response, and innovative ways of generating spin currents and spin manipulation. There are various sources of electron spin polarization such as spin Hall effect, spin Nernst effect, current-induced spin polarization, and thermal current-induced spin polarization also there is much more important source of the spin polarization which are shown below Figure 1.13. All these sources build various achievements in the application of spin polarization like Giant Magnetoresistance (GMR), spin valve, data storage,

spin-orbit driven phenomenon, etc. Out of all these sources of electron spin polarization, there could be another source that is the insertion of Li-ion inside the electrode material that could lead to the change of the up and down spin at the Fermi level which may introduce the spin polarization in the system of interest. Here, I have focused on one such study based on controlling the spin polarization by lithiation into the antiperovskite electrode material, which will be discussed in the first chapter of my thesis.

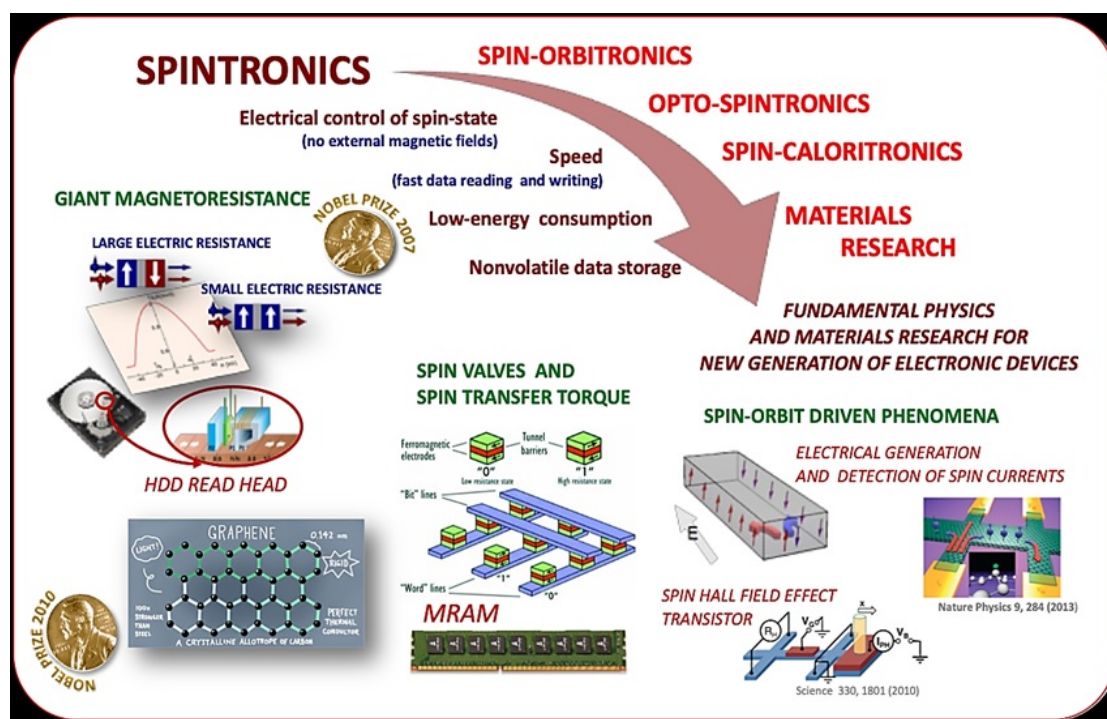


FIGURE 1.13: Sources of electron spin polarization (<http://zfmexo.home.amu.edu.pl/research.php>)

1.7.5 Antiperovskite as Advanced Battery Materials

As we have discussed earlier, antiperovskites can support many interesting properties that have the potential for an array of applications [3, 121]. In 1938 Zintl and Morawietz [2, 122] first reported on a Na-rich antiperovskite Na_3NO_3 in which X sites are occupied by Na and the A and B sites are occupied by NO_2^- and oxide anions (Figure 1.14, [2]). After that, the first antiperovskite alkali metal chalcogenide halides Na_3OBr and Na_3OCl was reported by Sabrosky et al [101], which built the foundation for the antiperovskite in solid states electrolyte research. In 2012 the first report appeared on Li-rich antiperovskite by Zhao and Daemen [101], and they showed that Li_3OCl , Li_3OBr , and $\text{Li}_3\text{OCl}_{0.5}\text{Br}_{0.5}$ [2] have excellent ionic conductivity of 10^{-3} Scm^{-1} at room temperature with low activation energies (0.2 - 0.3 eV), respectively. Hartwig et al. reported that Li and Na rich antiperovskites could be used as solid states electrolytes due to their excellent superionic conductivities of the order of 10^{-3} Scm^{-1} for Li_3OBr and Na_3OBr

[2]. The applications of Li- and Na-rich antiperovskite have also been proposed as battery cathode materials. Indeed, transition metal-based antiperovskite such as Li_2FeChO could be used as cathode materials (Ch= Chalcogenides = S, Se, Te)[2].

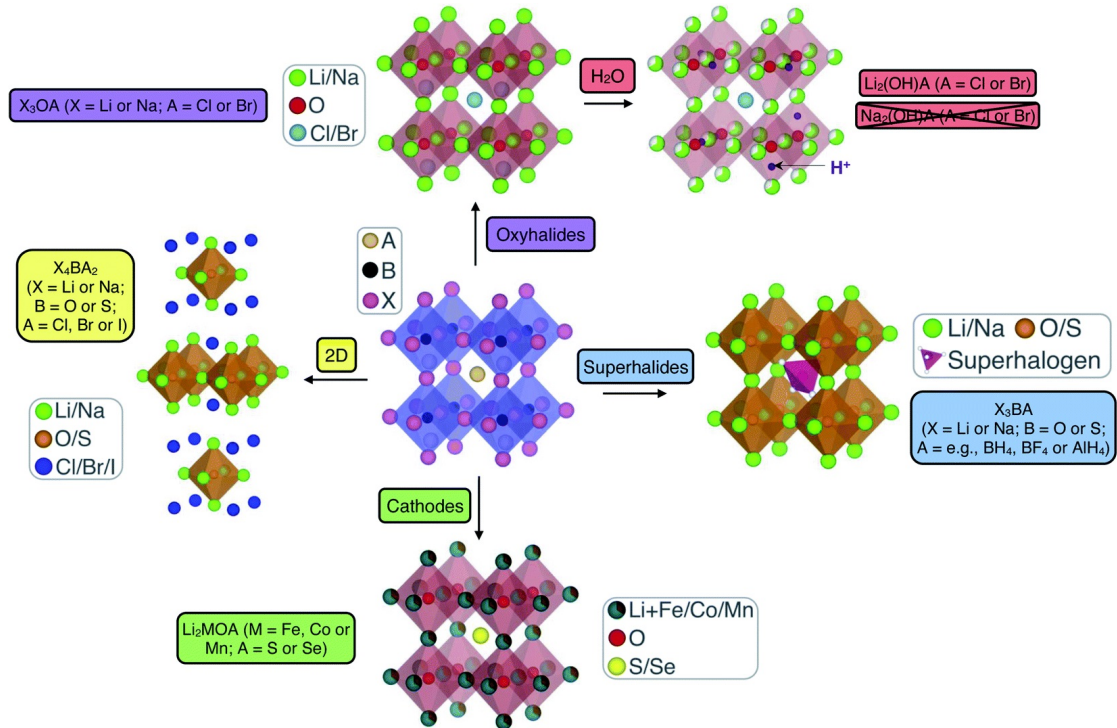


FIGURE 1.14: Antiperovskite materials for cathode and Solid State Electrolyte [2]

The theoretical capacity of Li_2FeSO is 227 mAh/g, comparable to some commercial cathode materials. The chemical flexibility in antiperovskite offers many possibilities for improving the battery performance by doping or substituting different transition metals such as Ni, Mn, Co, etc., in place of Fe in Li_2FeChO . But stability issues exist for this kind of structure due to Li insertion/extraction. There is no report published on the antiperovskite anode material, which still opens up new challenges and opportunities in the future. Hence, in my thesis, one chapter will be focused on antiperovskite nitride-based anode materials. Most of the advanced antiperovskite materials used as SSE and cathode materials are shown in Figure 1.15 [3]

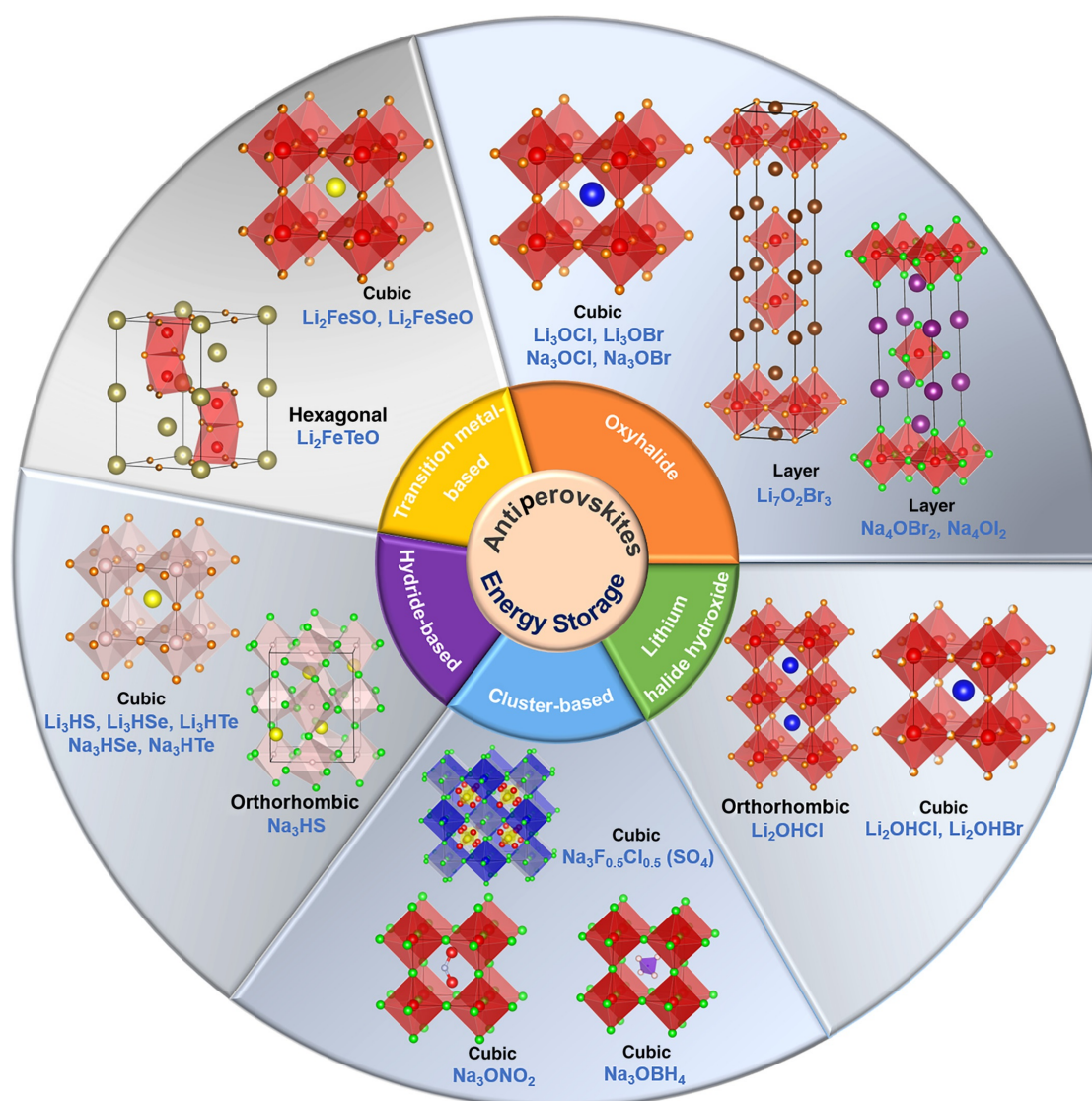


FIGURE 1.15: All antiperovskite materials for used as cathode and Solid State Electrolyte for Li and Na ion batteries [3]

1.7.6 Carbide and Nitride Antiperovskite

The work in this thesis is focused on carbide and nitride-based 3D antiperovskite (Figure 1.16). The unique cubic structure ($Pm\bar{3}m$, 221) of antiperovskite makes these two antiperovskites very promising and attractive. There are various carbide and nitride-based antiperovskites observed such as X_3AC where X is the transition metal (TM) (where $X = \text{Ti, Mn, Fe, Co, Ni, etc.}$) and A is the post-transition metal (where $A = \text{Ga, Al, Sn, Zn, Cu, In, Ge, etc.}$) [113, 123–125] (Grandjean et. al 1979, Stadelmaier and Huette) similarly X_3AN represents all nitride antiperovskite materials, here X could be alkaline earth metals (likes Mg, Ca, Sr, etc) and or transition metals (like V, Fe, Co, Ni, Cu, etc.) and A is the heavy metals (like As, Sb, Bi, Pd, etc.) [3, 42, 69, 123] (Yuan et. al 2021, Zhao et. al 2019). But here in our study, we have focused on an iron-rich 3D carbide antiperovskite Fe_3SnC and a cobalt-rich nitride antiperovskite Co_3CuN . Fe_3SnC is intermetallic as it has more than two metallic elements and also behaves as a very good conducting material. It contains a 60% iron atom and this Fe atom makes Fe_6C octahedral coordination induces strong hybridization between the Fe-3d and C-2p orbitals and produces magnetization in the system. Co-rich nitride antiperovskite Co_3CuN is a magnetic, highly conducting, and intermetallic material. Due to its high conducting nature, this material is used as an electrocatalyst [126].

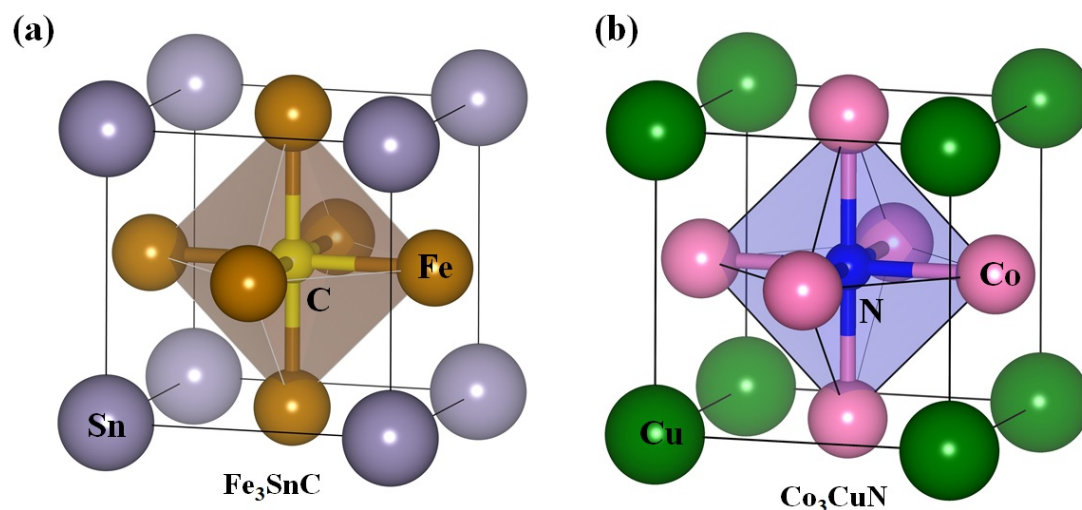


FIGURE 1.16: (a) Crystal structure of Carbide and Nitride (a) Fe_3SnC , (b) Co_3CuN with Fe_6C and Co_6N octahedral co-ordination coordination was studied in this thesis.

1.8 Aim and scope of the thesis

In this thesis, we have chosen to work on the exciting Antiperovskite material systems endowed with some unique and intriguing set of properties as advanced functional materials for spintronics and energy applications.

In the second working chapter, we report our work on the control of the magnetism and electronic spin polarization of a magnetic intermetallic antiperovskite carbide system, namely Fe_3SnC , with electrochemical lithiation and de-lithiation. This material is shown to behave like a high-capacity anode material for a Li-ion battery over the explored electrochemical voltage window and is able to reversibly incorporate four Li-ions. However, the XRD studies reveal that lithiation leads to a two-phase system (Li-Sn alloy and Fe_3C) and it evolves structurally with further lithiation. Interestingly, the experimental study further brings out that the magnetization of this material also reversibly follows lithiation and de-lithiation. Our theoretical (DFT) analysis has shown that Fe_3SnC is endowed with spin polarization (differing density of spin up and spin down states at the Fermi energy) and the same is true also with Fe_3C . The changes in magnetism and structure (XRD) observed experimentally, and the changes in spin polarization noted theoretically to mimic the same are suggested to emanate from lithiation of the Fe_3C phase in the two-phase system; since the Fe_3SnC system appears to decompose by extraction of Sn which has a strong affinity to form an alloy with lithium rendering Fe_3C phase to mimic the magnetism and spin polarization. It is a rather complex but interesting system with intriguing effects and can germinate a new concept of a spintronic battery.

Motivated by our initial work on the Fe_3SnC carbide system, we decided to probe another interesting antiperovskite material, this time a nitride Co_3NCu , to design a high-capacity antiperovskite anode material for alkali ion batteries. Until now, to the best of our knowledge, there is no report on an antiperovskite-based anode material, except for our earlier publication on Fe_3SnC for Li-ion batteries exhibiting a capacity of 450 mAh/g (K. Roy et al. 2020) [4]. With the presence of high metallic concentration (60%) and finite density of states at the Fermi level, Co_3NCu possesses high electrical conductivity (metallicity), which is important for a high-capacity battery anode material. Also, the concurrent presence of metallic (Co-Co) and covalent (Co-N) bonds endows this nitride antiperovskite with good structural stability which is potentially important for higher cycling capacity under reversible lithiation and delithiation. After careful consideration of different materials design aspects, we synthesized and optimized a core@shell Co_3NCu system, and characterized it in all its details. Interestingly, we were able to achieve a remarkably high capacity (1100 mAh/g) with antiperovskite anode material serving as

an anode in a Li-ion battery. The details pertaining to this study are reported in chapter 3.

Encouraged further by the results of our studies on carbide and a nitride antiperovskite reported in the first two chapters, we set out to grow high-quality (preferably epitaxial) thin films of the antiperovskite Co_3CuN on a single crystal of LaAlO_3 , a perovskite material. In a sense, this is therefore also a step towards developing and examining an antiperovskite/perovskite interface. Since most device platforms and fundamental scientific studies (like spin polarization via tunneling through a magnetic tip of a half-metallic material, electric field effects, etc.) are thin film-based, success in developing high-quality thin films of antiperovskites could open up many scientific opportunities, which drove us to undertake this work. For example, the electronic cation/anion and thereby property inversion across the interface between a perovskite and an antiperovskite could potentially lead to some new electronic and magnetic interface-borne effects. The presence of a high concentration of cations (TM ions) at the surface of an antiperovskite and the high concentration of anions (e.g. oxygen ions) at the surface of a perovskite make the interface interestingly different than the significantly explored perovskite/perovskite interfaces over the last two decades, which attracted our attention. Single crystal LaAlO_3 is a cubic perovskite with a lattice constant of 3.787 \AA and the cubic antiperovskite Co_3CuN has a fairly matching lattice parameter of 3.75 \AA , which makes them structurally compatible for epitaxial growth. Using the Pulsed Laser Deposition or PLD technique we, therefore, deposited Co_3CuN (CCN) thin films on the oxide substrate LaAlO_3 (LAO) along its 001 crystal facet. All the protocols of the deposition and property characterizations have been discussed in chapter 4.

Chapter 2

Lithiation-induced Evolution of Biphasic Constitution in Intermetallic Anti-perovskite Fe_3SnC and its consequences for magnetism: A Case for Rechargeable Spintronic Battery

Abstract

A key notion defining the progress of the emergent fields of modern electronics, renewable energy, and smart systems is “charge storage” which is primarily embodied in various battery chemistries and systems. In addition to the “charge” property, the electron also has the “spin” property which is exploited in the field of “spintronics” to access novel magnetically controlled device actions that are not accessible to conventional electronics. An interesting question is whether the two can be fruitfully integrated into a single device concept to expand the horizon of device design and applications. Herein, we present a combined experimental and theoretical study of virgin and lithiated conducting intermetallic anti-perovskite with nominal stoichiometry represented as $\text{Li}_x\text{Fe}_3\text{SnC}$ ($x = 1, 2, 3, 4$) to establish the principle of reversible and concurrent charge and spin polarization storage that can be aptly christened as Iono-Spintronics representing a notion of Spintronic Battery. The experimental results however showed that lithiation turns the system into a biphasic state comprised of tin-lithium alloy (due to high affinity of Sn for Li) along with lithiated Fe_3C ; the process exhibiting multiple cyclability (rechargeability).

2.1 Introduction

An electron is endowed with two important properties namely charge and spin. Manipulating the flow of electronic charge in various ways in materials media is the mandate of modern electronics and the world has witnessed its tremendous impact on our lives over the past several decades. During the past few decades, there has also been significant progress in manipulating the spin property of electrons to generate novel magnetically manipulated device architectures and responses that are conceptually entirely different from those of conventional electronics. This branch of physics, termed Spintronics, also promises interesting new solutions for our futuristic technological needs in fields such as IOT [127].

One of the key device constructs of modern electronics that has fueled very rapid progress of the emergent fields of renewable energy and smart mobile device systems is the concept of “charge storage” embodied in various battery systems that have been developed over many decades. During the past two decades, a question that has surfaced and been discussed in the literature in a limited way is whether a “spin battery” is feasible along the same lines as a “charge battery”. A “spin battery” [128–131] envisages device architectures that could provide pure spin currents into the external circuits without associated charge current. These studies have involved some very creative suggestions involving electric field controlled selective spin injection across a semiconductor interface [132–134], or use of topological insulators, etc [135]. A few other studies, which have no direct bearing on the concept of “spin battery” as stated above, have addressed a separate question of manipulating the magnetic moment of some magnetic materials by electrochemical lithiation and delithiation as done in a rechargeable battery system for “charge” storage. To put our work into perspective, we briefly discuss below some of these past research works.

In an early study, Sivakumar et al. (MIT group) examined the changes in the magnetic and structural properties of magnetite (Fe₃O₄) as a function of lithiation. An almost 75% drop of saturation moment was observed upon 2 moles of Lithium insertion per formula unit [136]. Again in his other paper, he showed that by electrochemical lithiation a large change in the magnetization of CrO₂ is possible [136]. In another work, Abdel-Ghany et al. studied the magnetic properties of LiNi_{0.33}Mn_{0.33}Co_{0.33}O₂ (lithiated NMC) more from the standpoint of using magnetism as a diagnostic tool for developing fundamental understanding and control of battery phenomena [137, 138]. However, no battery electrochemistry was used to examine reversible charge-discharge effects. In a subsequent and more recent work, Reitz et al. explored the magnetism of mesoporous Lithium ferrite films and demonstrated in situ tuning of their magnetic properties by reversible topotactic lithium insertion [139]. In a somewhat similar study based on

nanoscale hematite battery electrode, Zhang et al. showed reversible and rapid manipulation of its magnetism by 3 orders of magnitude by lithiation/delithiation at room temperature [140]. In another purely theoretical recent study, Wang et al. considered the case of half-metallic (100% spin polarization) TiF₃ under lithium insertion and showed that the half metallicity is retained upon insertion [141]. They proposed that such material could potentially serve as an anode for the Li-ion spin battery.

One must differentiate between the technical interest in reversibly changing the magnetic moment and/or coercive field of a ferromagnet (or a ferrimagnet or canted antiferromagnet) by lithiation/de-lithiation and changing its spin polarization, because the latter is important for spintronic devices wherein spin itinerancy is the key, rather than static information storage. Indeed, we believe that there is significant scope for doing new and novel device science if we do not restrict to the concepts of separate charge and spin storage. Indeed, one could envision a new domain of “iono-spintronics” wherein ionic movements and separations such as in Li-ion batteries could also be used to concurrently control the spin polarization of the material. The origin of the present work lies in our recent research on a 3D antiperovskite intermetallic system Fe₃SnC [4], wherein we found that this conducting system (itinerancy required for spintronics) is a robust high capacity anode material that can reversibly cycle four lithium ions. While exploring this system by first-principles DFT calculations we discovered an interesting fact that this system not only has a finite density of states at the Fermi energy (metallicity), but also a net spin polarization (the net difference between spin up and spin down electrons at Fermi energy (E_F)). This raised the possibility that by lithiation and de-lithiation in a battery scheme, it may be possible to ionically and reversibly control the spin polarization (and magnetism) of the material by manipulating the charge (Li-ion) population; a perfect case for the suggested concept of “Iono-Spintronics” or a “spintronic battery”. Following these theoretical insights, we experimentally examined the magnetism (along with the other properties) in the solid-state sintered extra Li-incorporated bulk system with stoichiometry of Li_xFe₃SnC ($x = 1, 2, 3, 4$), as well as the reversible magnetism changes occurring in the same material as a function of lithiation/de-lithiation in a Li-ion battery half-cell. Indeed, we found remarkable similarities between the theoretical and experimental results, although the experimental results showed that lithiation turns the system into a biphasic state comprised of tin-lithium alloy (due to high affinity of Sn for Li) along with lithiated Fe₃C. This work clearly suggests that the suggested iono-spintronic or charge-driven spintronic battery effect is indeed possible and can be exploited in interesting applications.

3D antiperovskite are rapidly emerging as materials systems of significant interest in various fields of application; with nitride and carbide-based antiperovskite attracting the most recent attention. The general formula for antiperovskite materials is M₃AX where

M is a 3D transition metal (e.g., Fe, Ni, Co, Mn, Cu, etc.), A is a post-transition metal (e.g., Sn, Ga, Ge, etc.), and (X= N, C, O). In an M₃AX cubic antiperovskite material, the M atom is situated at the face center, the A atom is at the corner, and the C atom is at the body center with M₆C octahedral coordination [142]. Antiperovskite material has many applications in the different fields of science and technology such as advanced battery materials [101, 143–148], magnetism and magnetoresistance [124, 125, 149–152], the emergence of superconductivity [32, 51, 102, 103, 153–155], electrochemical energy conversion and storage [156–158], etc.

2.2 Experimental and Computational Details

Fe₃SnC was prepared by a two-step solid-state synthesis using an evacuated quartz tube as reported by Roy et al. Li_xFe₃SnC (x= 1 - 4) was synthesized using this Fe₃SnC powder and Lithium acetate (CH₃COOLi). These two compounds were mixed in appropriate ratios and heated in an argon atmosphere at 900°C for 4 hours. These four samples were characterized by Powder X-Ray Diffraction (P-XRD), high-Resolution Transmission Electron Microscopy (HRTEM), and Field Emission Scanning Electron Microscopy (FESEM). The PXR, FESEM were performed by using a Bruker D8 advance X-ray instrument and NOVA nano SEM, respectively. HRTEM was performed by using a Jeol, JEM 2200FS at 200 keV. Magnetization (M) was measured as a function of Temperature (T) and applied magnetic field (H) using commercial 7 T-SQUID-VSM (Quantum Design Inc., USA) systems. The zero-field cooling (ZFC), and field cooled (FC) measurements were performed at an applied magnetic field of 100 Oe. Also, M vs H measurements was carried out at constant temperatures of 5K and 300K.

We performed spin-polarized ab-initio density functional theory (DFT) based calculations using Quantum Espresso (QE) computer package [159]. Ultrasoft pseudopotentials were used to describe the electron-ion interactions [160–162]. The valence electronic configurations, considered in this work, for each element are: Sn [4d¹⁰ 5s² 5p²], C [2s² 2p²], Fe [3s² 3p⁶ 3d⁶ 4s²] and Li [1s² 2s¹]. A plane-wave basis set determined by kinetic energy cut-offs of 60 Ry (for wavefunction) and 520 Ry (for charge density) was used to expand the wavefunction and charge density. The electron-electron exchange-correlation was described by the Perdew-Bueke-Ernzerhof (PBE) parametrization of the generalized gradient approximation [163]. Brillouin zone integrations were performed with a shifted (12×12×12) Monkhorst-Pack [164] k-point mesh. Marzari-Vanderbilt smearing of 0.008 Ry was used to speed up the convergence [164, 165].

2.3 Results and Discussion

Fe_3SnC is a cubic antiperovskite intermetallic compound. In this crystal, eight tetrahedral and three octahedral interstitial void spaces are present, hence there is sufficient space for a Lithium atom to navigate within the cubic unit cell of Fe_3SnC . In our earlier paper, we have shown that from the CV plot (Figure 2.1 b) a maximum of 4 lithium atoms can be accommodated in the bulk Fe_3SnC through electrochemical lithiation and this material behaves as high capacity anode material with an impressive specific capacity of 450 mAh/g (Figure 2.1 a) [4].

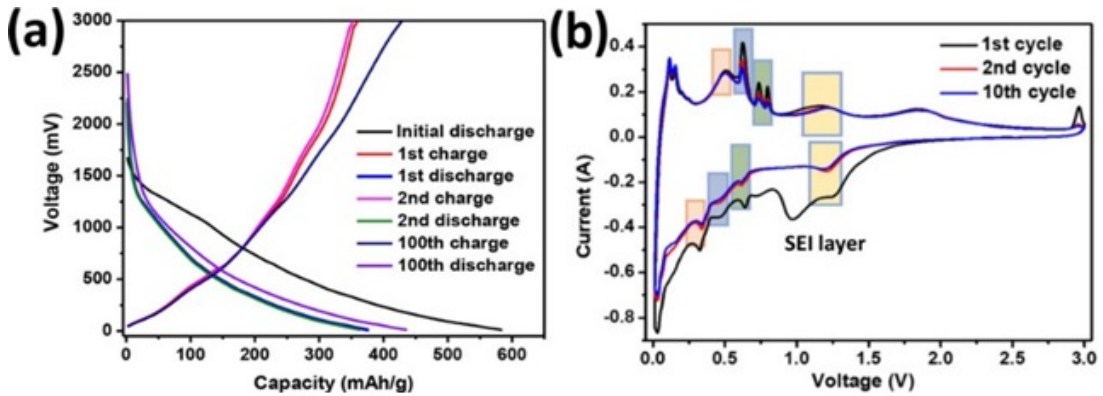


FIGURE 2.1: (a) Capacity of Fe_3SnC and (b) Cyclic Voltammetry or CV plot. [4]

By simple mathematical calculation we have seen that, maximum 4 Li are possible which also corresponds to the four sharp redox peaks in the CV plot (Figure 2.1 b) and the calculation details are presented in the Figure 2.2

□ $1 \text{ mAh} = 3.6 \text{ A.S} = 3.6 \text{ C}$

$1 \text{ electron} = 1.6 \times 10^{-19} \text{ C}$

$3.6 \text{ C} = 2.2 \times 10^{19} \text{ no. of electron} = 2.2 \times 10^{19} \text{ no. of Li}^+$

So,

$1 \text{ mAh} = 3.6 \text{ C} = 2.2 \times 10^{19} \text{ no of electron or Li}^+$

□ Here we obtained 450 mAhg^{-1} due to Li incorporation into the Fe_3SnC crystal system.

□ Now, calculated molecular weight of the unit cell of $Fe_3SnC = 298.26 \text{ g/mol}$

□ Hence, one unit cell contains

$2.2 \times 10^{19} \times 450 \times (298.26 / 6.023 \times 10^{23}) = 4.36 \text{ (~4) no. of Li atoms}$

FIGURE 2.2: Detail calculation of maximum number of Li atoms. [4]

Taking these experimental inputs into consideration, in the present case, we first modeled the systematic insertion of 1-4 Lithium atoms at different interstitial positions in the bulk Fe_3SnC crystal. We find that there are 34 different inequivalent configurations as shown in Figure 2.3

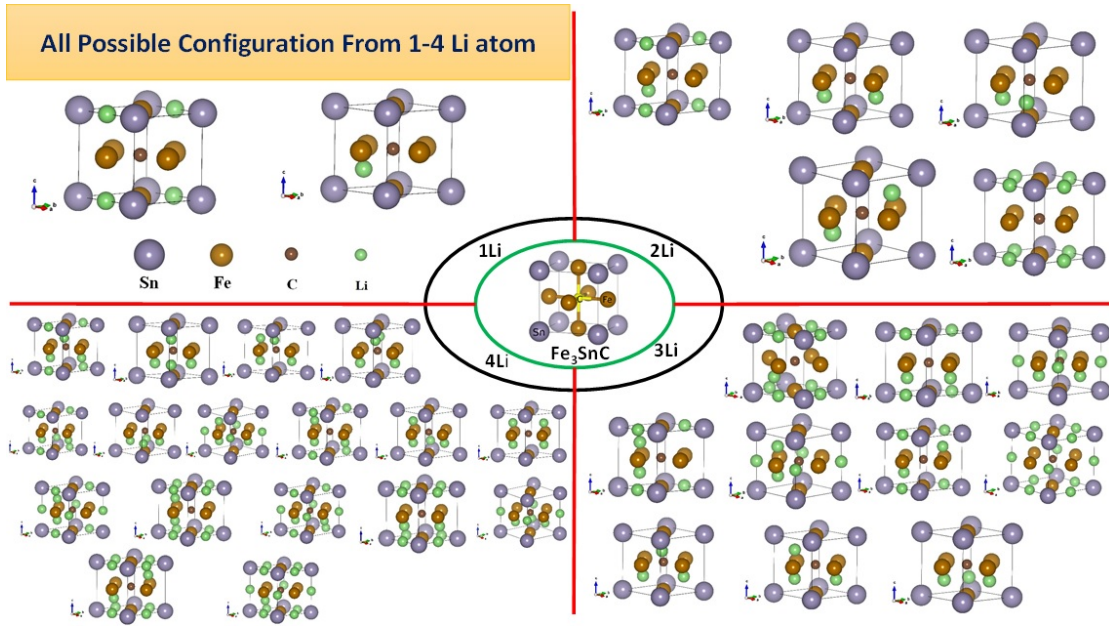


FIGURE 2.3: 34 lithiated configuration of 1-4Li.

2.3.1 Structural and Morphological Analysis

Fe_3SnC is a cubic antiperovskite intermetallic compound. In this crystal, eight tetrahedral and three octahedral interstitial void spaces are present, hence there is sufficient space for a Lithium atom to navigate within the cubic unit cell of Fe_3SnC . In our earlier paper, we showed that a maximum of 4 lithium atoms can be stored in bulk Fe_3SnC through electrochemical lithiation and this material behaves as a high capacity anode with a very impressive specific capacity of 450 mAh/g [4]. However, in that study, it could not be unambiguously discerned whether the system retains its single-phase character upon multiple lithium-ion incorporations. Taking clues from these experimental inputs and to plan the present work, we first modeled the systematic insertion of 1-4 Lithium atoms at different interstitial positions in the bulk Fe_3SnC crystal and found that there are 34 different inequivalent configurations as shown in Figure 2.3. Upon optimizing all these structures (Figure 2.4), we observed that due to the insertion of the Li atom(s) in the unit cell of Fe_3SnC , significant strain and structural deformations occur. The theoretically obtained lowest energy lithiated crystal structures for 1-4 Li and their optimized lattice parameters are given in Figure 2.5. It can be seen from Figures 2.4 and Figure 2.5 that the theory suggests that after one Li incorporation, the cubic phase of Fe_3SnC must get distorted and become rhombohedral (hexagonal family) if it has to retain its single-phase character. However, as our experimental work described below revealed, the great affinity of Sn to Li leads to the extraction of Sn out from Fe_3SnC , leading to a biphasic system of Sn-Li alloy phase(s) and Fe_3C (with partial or full lithiation).

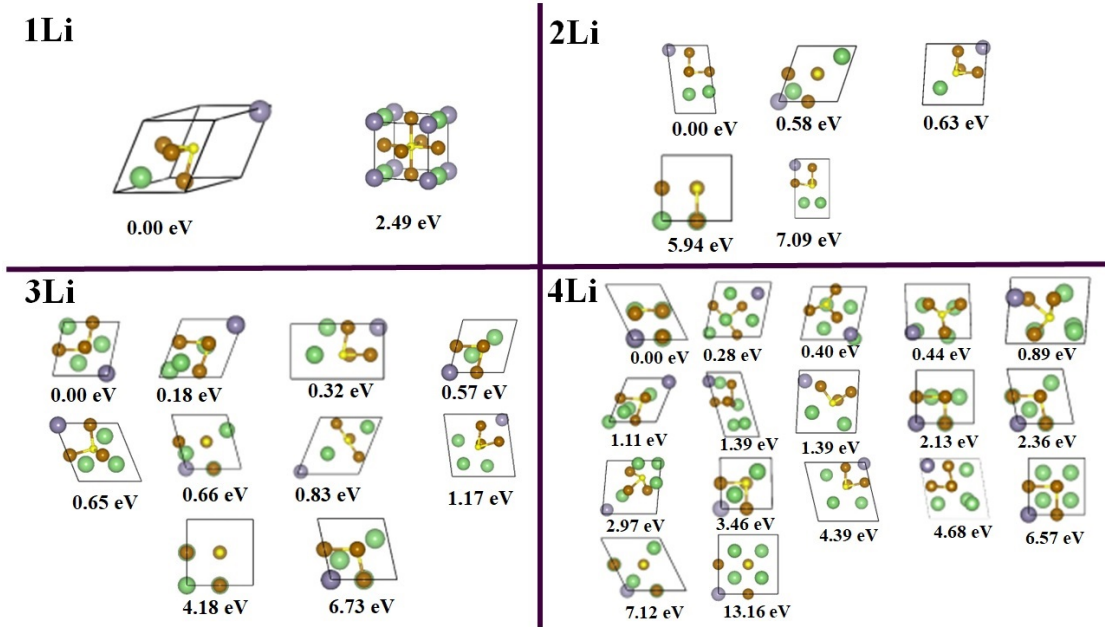


FIGURE 2.4: 34 Optimized lithiated configuration of 1-4Li.

We synthesized the material with progressively higher Lithium content ranging from $\text{Li} = 1$ to 4 (as described in the experimental section) and scrutinized the corresponding x-ray diffraction data. Upon insertion of the very first Li atom, however, the experimental data showed completely different peak locations and relative intensities varies those of the parent Fe_3SnC phase. The major peak signature of Fe_3SnC was at 40.3° (111) but that for a single lithiated case was noted to occur at 38.22° (111). The peak at 23.02° (100) for non-lithiated Fe_3SnC was not found, while another strong one was located at 18.32° . This suggested that perhaps due to high lithiation-induced stress, the system is not able to evolve along the the expectations based on theory (Figures (Tables 2.5), but rather evolve into new phase constitution. The entire family of peaks appeared to change reflecting changes in the crystal symmetry. Interestingly, with further addition of each lithium, the relative intensity ratios of peaks are seen to change, but the positions roughly remain the same as in the single lithium incorporation case. Since Sn is known to form an alloy with lithium enabling high anode capacity, [166–170] we considered the possibility of Sn from Fe_3SnC getting out from the structure to form an alloy phase Sn_xLi_y , leaving the Fe_3C carbide phase to incorporate additional Lithium. Indeed, we could identify the peaks for the lithiated phases with the concurrent presence of tin-lithium alloy and Fe_3C . The changes in the intensity ratios and small changes in the lattice positions could be understood from the distortions and strains. Morphologically (FESEM data, Figure 2.6), the cases of non-lithiated Fe_3SnC and lithiated compounds with one or two Lithium incorporations exhibit a layered morphology. However, for the 3 or 4 lithium incorporation cases, the morphology appears to be more in the form of

crumpled or ill-defined sheets. This can be due to excess stress embedded in these highly lithiated cases.

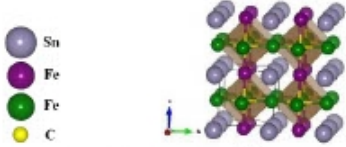
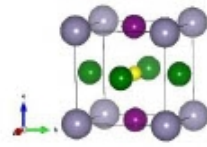
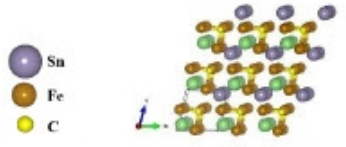
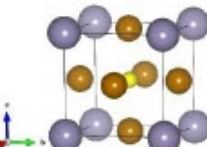
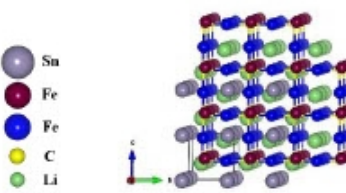
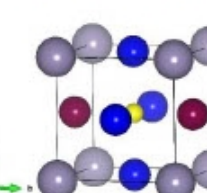
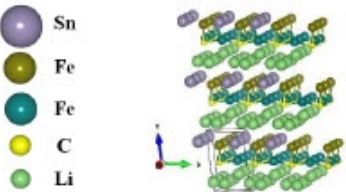
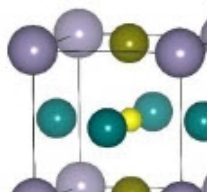
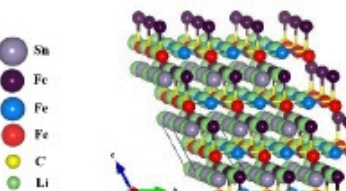
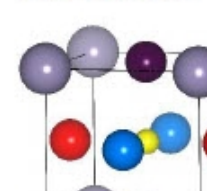
Lithiated Fe_3SnC	Magnetic Moment of Fe atom (μ_B/Fe)
<p>Li_0Fe_3SnC</p>  <p>$a = b = c = 3.87 \text{ \AA}; \alpha = \beta = \gamma = 90^\circ$</p>	<p>1.84, 1.84, -1.38</p> 
<p>Li_1Fe_3SnC</p>  <p>$a = b = c = 4.39 \text{ \AA}; \alpha = \beta = \gamma = 67.03^\circ$</p>	<p>1.85, 1.85, 1.85</p> 
<p>Li_2Fe_3SnC</p>  <p>$a = 6.48 \text{ \AA} \quad b = c = 3.79 \text{ \AA}; \alpha = 89.26^\circ$ $\beta = \gamma = 97.02^\circ$</p>	<p>1.99, 1.49, 1.49</p> 
<p>Li_3Fe_3SnC</p>  <p>$a = b = 3.99 \text{ \AA} \quad c = 6.42 \text{ \AA}; \alpha = \beta = 95.69^\circ$ $\gamma = 79.03^\circ$</p>	<p>2.26, 2.26, -2.36</p> 
<p>Li_4Fe_3SnC</p>  <p>$a = 8.51 \text{ \AA} \quad b = 3.76 \text{ \AA} \quad c = 4.63 \text{ \AA}; \alpha = 90.04^\circ$ $\beta = 66.03^\circ \quad \gamma = 66.08^\circ$</p>	<p>2.29, 1.96, 2.34</p> 

FIGURE 2.5: Magnetic moments of Fe atoms of the optimize structure of Fe_3SnC and Li_xFe_3SnC ($x = 1-4$) and lattice paramters

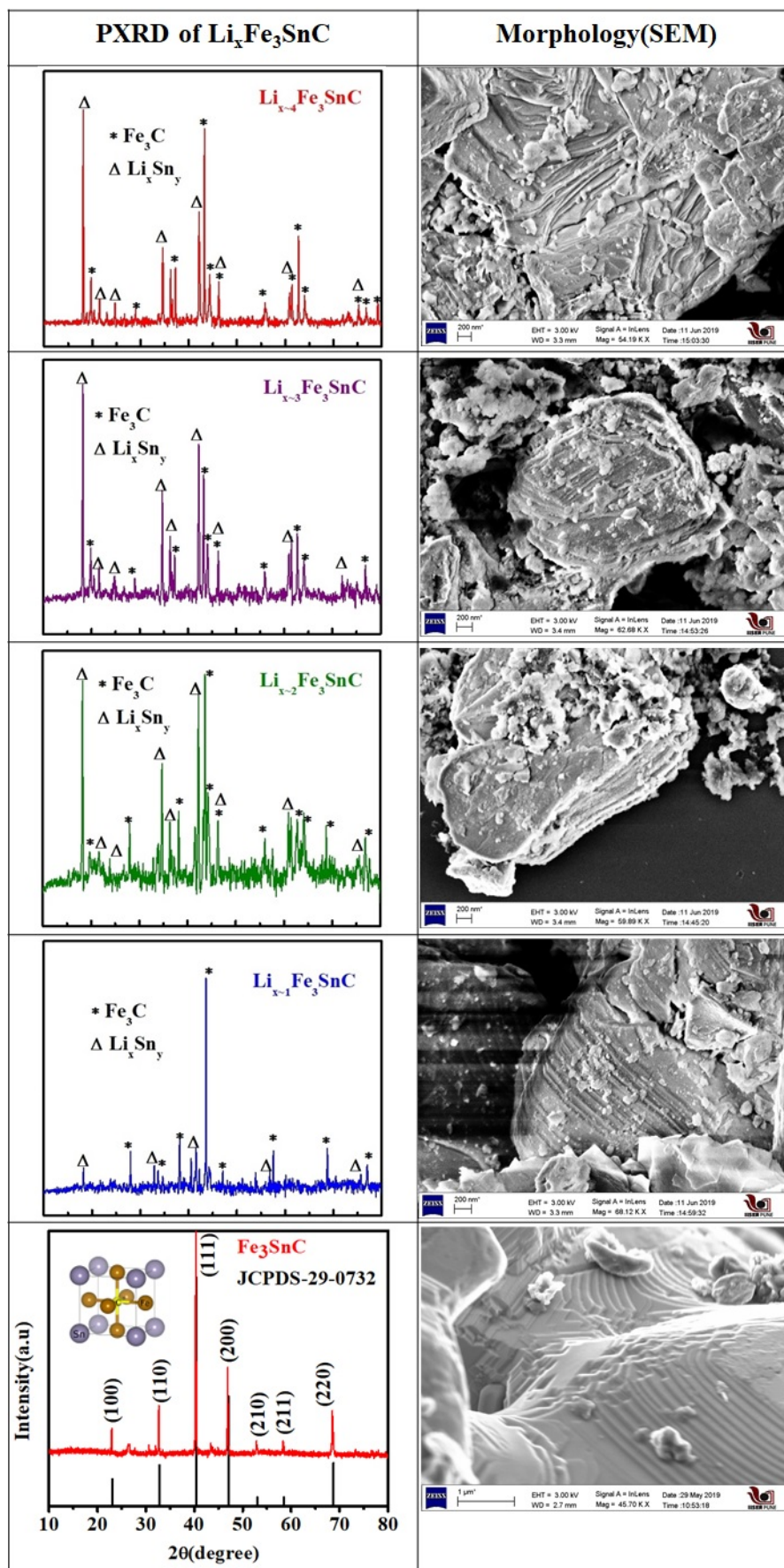


FIGURE 2.6: (a-c) HRTEM image of lithiated compound $LiFe_3SnC$, Inset shows atomic details showing hexagonal arrangement; (d) represents the theoretically obtained image showing atomistic details of two-phase Fe_3C and $LiSn$.

HRTEM images of the single lithium-containing Fe_3SnC compound (which shows excellent magnetic properties in this series as discussed below) viz. $LiFe_3SnC$ is shown in Figure 2.7(a). The interplanar distance (d) is found to be 0.41 nm and this is very close to the theoretically obtained value of 0.43 nm and which corresponds to the (100) plane of the rhombohedral lattice (hexagonal family) as shown in Figure 2.7(b). From the diffraction image of Figure 2.7(c) corresponding to the major (100) planes, it is clear that we do observe the hexagonal phase after a single lithiation in Fe_3SnC , as also represented by the red coloured line in Figure 2.7(b) with the $LiSn$ alloy phase. This corroborates excellently with our theoretically obtained crystal structure for a single Li case as shown in 2.7(d) where both Fe_3C and $LiSn$ phases are present.

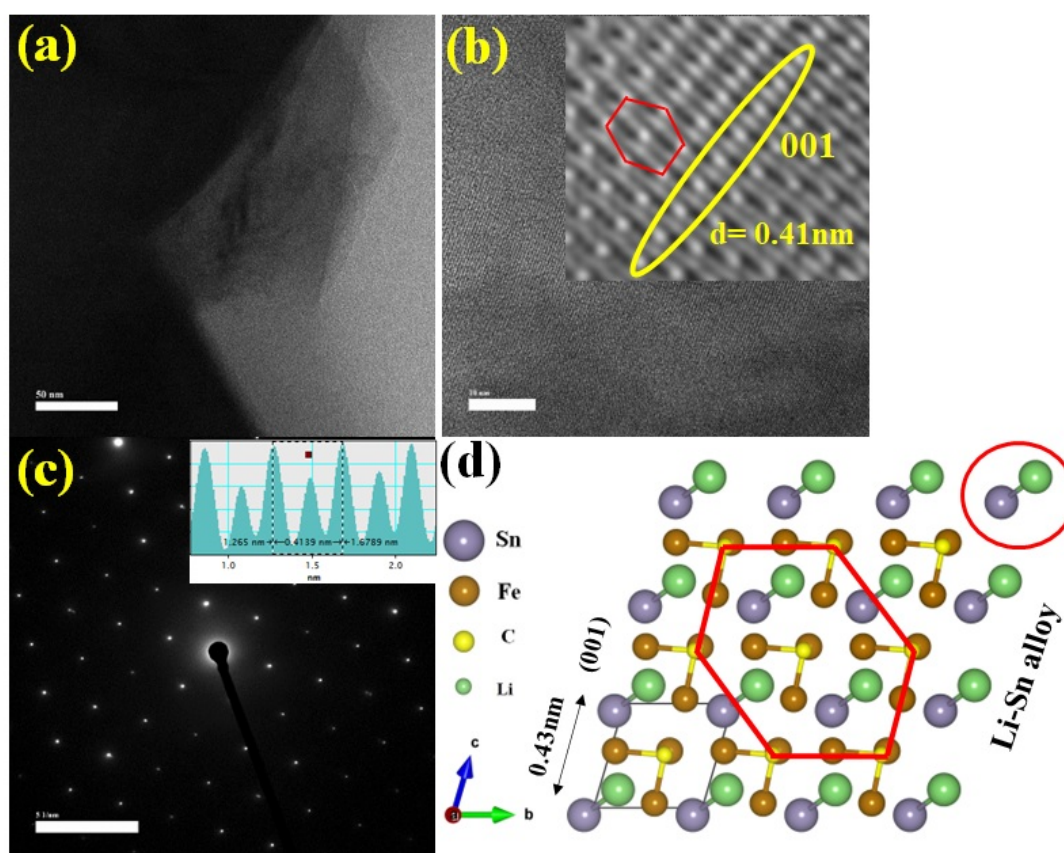


FIGURE 2.7: (a) HRTEM image of lithiated compound Li_xFe_3SnC , Inset shows atomic details showing hexagonal arrangement; (b) represents the theoretically obtained image showing atomistic details and hexagonal arrangement; (d) crystal structure of the single lithiated compound.

2.3.2 Magnetic Measurements

We performed the magnetic measurements of all the synthesized powder samples at 300K and 5K. These magnetization data are presented in the M-H curve for both pristine and a single lithiated Fe_3SnC systems at 5K and 300K are presented in Figure 2.8(a, b). On the right Y-axis, we present the magnetic moments per Fe atom.

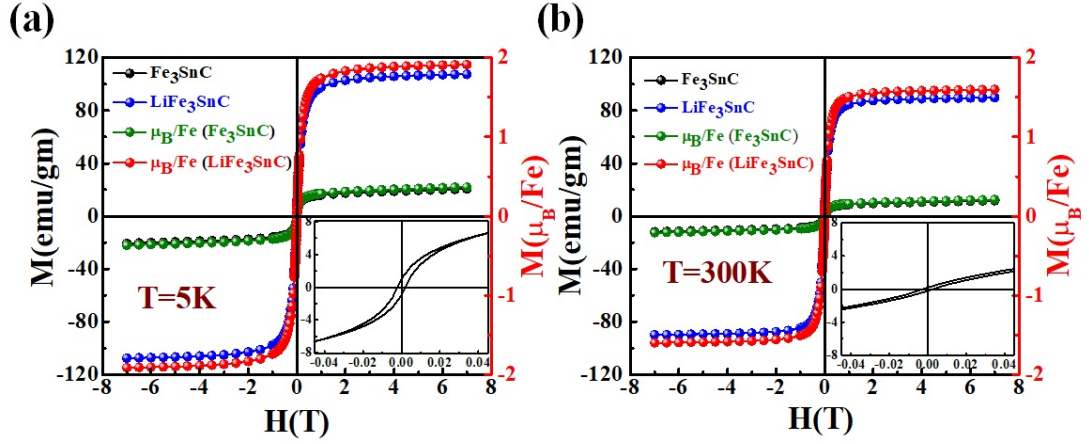


FIGURE 2.8: (a), (b) M vs H plot of pure Fe_3SnC and a single lithiated Fe_3SnC at 5K and 300K.

For pure Fe_3SnC , we observe that the sample exhibits a net saturated magnetization which could, in principle, emanate from a ferromagnetic or a ferrimagnetic order. However, as the value of M is quite small, the system can be considered to have an FIM order [171] at both the temperatures. It has a very small coercive (H_c) field of 25.7 (20.6) Oe at 300K (5K) and also a small saturation magnetization (M_s) of 11.73 (20.8) emu/gm at 300K (5K) respectively. After single lithiation (one Li-ion incorporation) that leads to biphasic state as mentioned earlier, we observe that there is an enormous change in the saturation magnetization (M_s) and the corresponding M_s value increases from 11.73 (20.8) emu/gm to 101.52 (107.42) emu/gm at 300K (5K), respectively. However, there are very small changes in the coercive field; the values changing to 15.6 (12.1) Oe at 300K (5K), respectively.

In pure and lithiated Fe_3SnC , the Fe atom is expected to be primarily responsible for the magnetization, hence we calculated the magnetic moments per Fe atom. The calculated magnetic moment on an Fe atom of Fe_3SnC is 0.21 (0.38) μ_B/Fe atom at 300K (5K) and for LiFe_3SnC it is 1.81 (1.91) μ_B/Fe at 300K (5K), respectively. Thus, one Li-ion introduction makes a huge change in the magnetic moment of Fe which is clear from the above Figure 2.8(a, b) and it nicely corroborates with our theoretically obtained results discussed below in Figure 2.16. After a successive insertion of Li in the pristine system (Fe_3SnC), we observed that the saturation magnetization (M_s) changes dramatically

which is presented in the M vs H plot shown in Figure 2.9(a-b). As discussed earlier, however, the system evolves as a biphasic material and not a single-phase material.

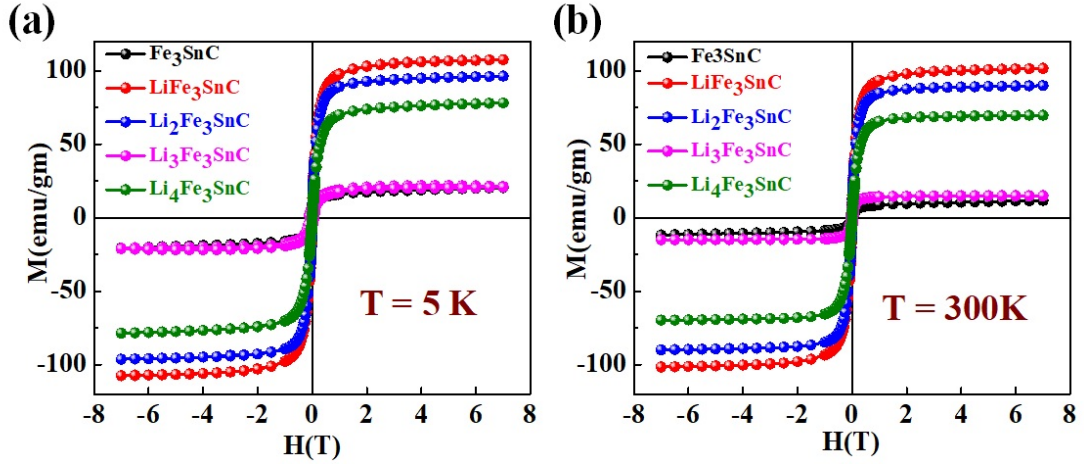


FIGURE 2.9: (a), (b) M vs H plot of pure Fe_3SnC and all lithiated $\text{Li}_x\text{Fe}_3\text{SnC}$ ($x=1 - 4$) at 5K and 300K.

In Figure 2.10(a, b) we present the M vs T plot at a constant magnetic field of 100 Oe for both the pristine and single lithiated Fe_3SnC . In the inset of Figure 2.10(a), we have presented the dM/dT vs T plot, which represents the paramagnetic transition temperature T_c of Fe_3SnC at 71K, which is closely matched with the reported value 77K [124]. From the nature of the ZFC and FCW curves, it is seen that pure Fe_3SnC is a low-temperature soft ferrimagnetic material[172].

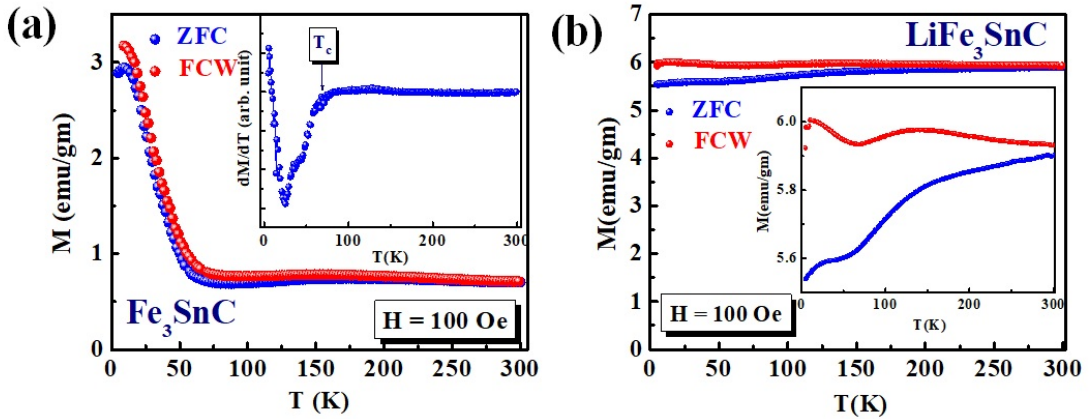


FIGURE 2.10: ZFC and FCW curve of (a) pure Fe_3SnC , (b) single lithiated LiFe_3SnC .

But upon single lithiation, it becomes room temperature ferromagnetic [168], which is seen from the ZFC and FCW bifurcation curve(s) and strong finite moment noted in Figure 2.10(b). With successive lithium concentrations, the magnetic order of the material changes as shown in Figure 2.11.

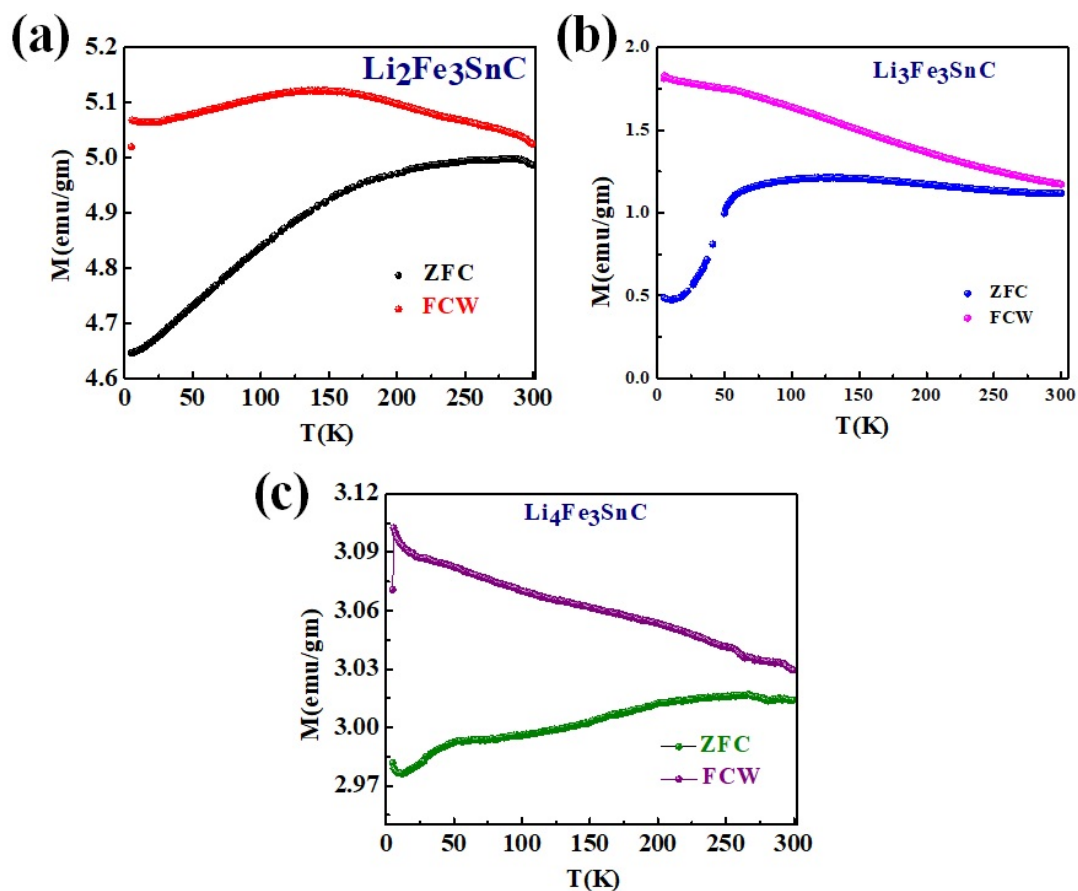


FIGURE 2.11: ZFC and FCW curve of other lithiated phases of Fe_3SnC .

2.3.3 DFT Based Calculations of the Electronic and Magnetic Properties

Since we found that lithiation evolves the sample into a biphasic constitution involving a tin-lithium alloy (Sn getting extracted from the Fe₃SnC phase to form the alloy) and a partially lithiated Fe₃C phase component; we examined theoretically (DFT) whether the magnetism and the changes therein emanate from the latter phase due to lithiation-induced strain and related changes.

In earlier reports, there has been some controversy about the magnetic ground state of Fe₃SnC [124, 173]. Stadelmaier and Huetter suggested that this ternary carbide is ferromagnetic [173]. Ivanovski et al. reported that this is nonmagnetic [155], while another experimental group of Wang et al. [125] reported that it could behave as a spin glass material. Grandjean reported that Fe₃SnC may have an FIM coupled phase below 77 K [58]. Our DFT study suggests that the Fe₃SnC is ferrimagnetic, as discussed in the Table 2.1 where from the energy value its clearly tell that FIM is more favorable magnetic order.

TABLE 2.1: Energy difference(ΔE) between the different magnetic orders of Fe₃SnC from the lowest energy FIM ordering.

Magnetic Order	ΔE (meV)
Non-magnetic (NM)	2.42
Ferromagnetic (FM)	37.5
Ferrimagnetic (FIM)	0.0

In the present case however, we are primarily concerned about the Fe₃C case, since the lithiation is noted to extract Sn from the Fe₃SnC compound and further proceeding happens in the Fe₃C phase. Thus, we need to compare the magnetism of the unlithiated case of Fe₃SnC with that of lithiated Fe₃C as the system evolves with more lithium. Some differences between experimental and theoretical results may emanate from partial lithiation of Fe₃C.

We first considered the cubic structure of the Fe₃C (Pm $\bar{3}$ m) phase taken from the OQMD database (ID: 1998746) [174, 175]. We optimized pure (just for comparison) and all the lithiated configurations of Fe₃C and calculated the density of states (DOS) for all the stable structures of Li_xFe₃C and the corresponding spin polarization with successive lithiation from 1-4 Li as discussed below

The optimized lattice parameters of the lithiated Fe₃C presented in Table 2.2 suggest that after 2-4 Li incorporation the lattice parameters evolve along different crystallographic directions. As can be seen from the analysis of XRD data based on the Williamson Hall method presented in Figure 2.12(a-e), the experimental results appear to broadly

TABLE 2.2: Optimized lattice parameters of lithiated Fe_3C and $\text{Li}_0\text{Fe}_3\text{SnC}$

Lithiated system	Lattice parameters
$\text{Li}_0\text{Fe}_3\text{SnC}$	$a=b=c=3.87\text{\AA}$; $\alpha=\beta=\gamma=90$
LiFe_3C	$a=b=c=3.87\text{\AA}$; $\alpha=\beta=\gamma=90$
$\text{Li}_2\text{Fe}_3\text{C}$	$a=4.37$, $b=c=4.88\text{\AA}$; $\alpha=50.67$ $\beta=118.88$ $\gamma=129.33$
$\text{Li}_3\text{Fe}_3\text{C}$	$a=b=4.37$, $c=5.28\text{\AA}$; $\alpha=\beta=89.98$ $\gamma=128.05$
$\text{Li}_4\text{Fe}_3\text{C}$	$a=b=4.57$, $c=6.74\text{\AA}$; $\alpha=99.92$ $\beta=80.08$ $\gamma=131.86$

reflect the systematic seen in the theoretical results presented in Figure 2.13(a-d) which corroborate fairly well with our experimental XRD patterns shown in Figure 2.6

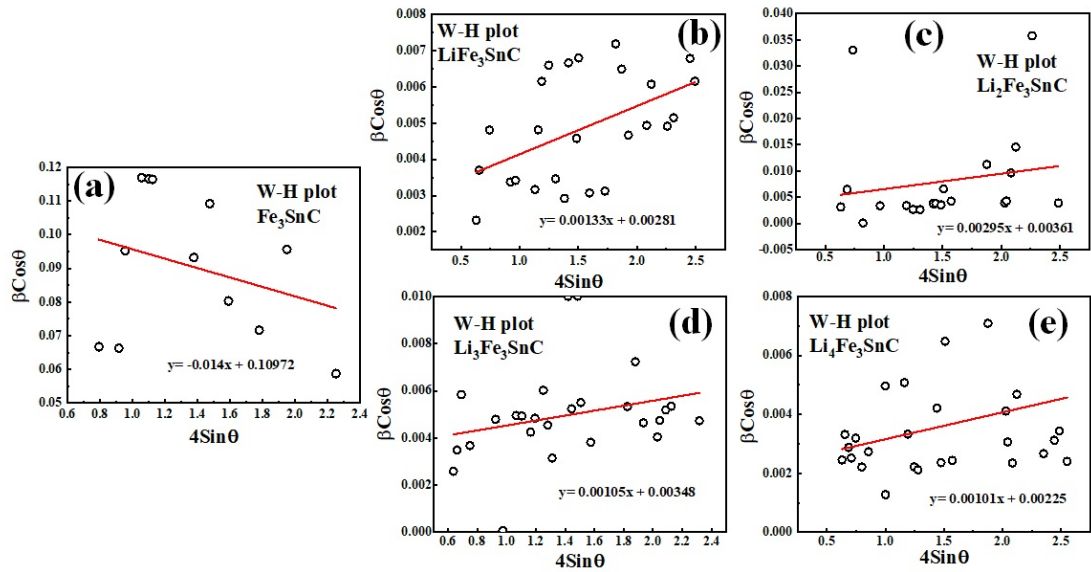


FIGURE 2.12: Williamson Hall or WH plot: (a) Fe_3SnC , (b) LiFe_3SnC (c) $\text{Li}_2\text{Fe}_3\text{SnC}$ (d) $\text{Li}_3\text{Fe}_3\text{SnC}$ (e) $\text{Li}_4\text{Fe}_3\text{SnC}$.

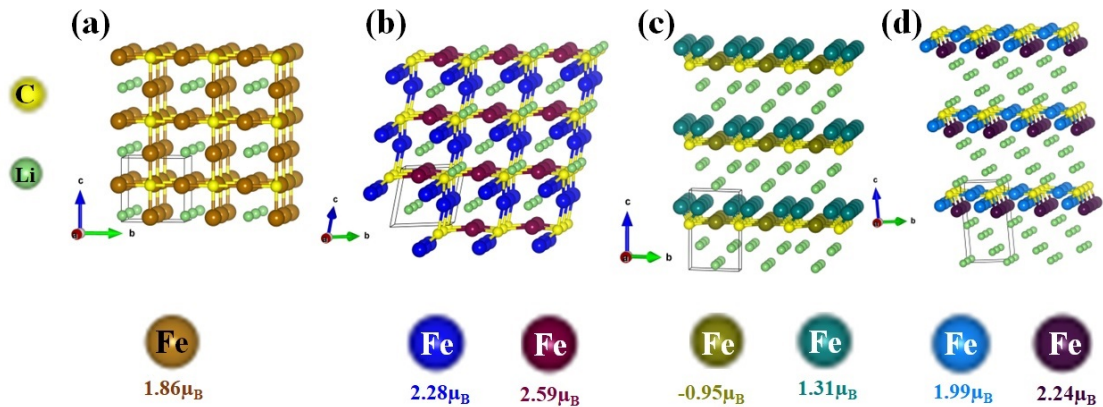


FIGURE 2.13: The repeating unit of lithiated phases of Fe_3C : (a) LiFe_3C (b) $\text{Li}_2\text{Fe}_3\text{C}$, (c) $\text{Li}_3\text{Fe}_3\text{C}$ and (d) $\text{Li}_4\text{Fe}_3\text{C}$. The different colors of the Fe atom correspond to the different magnetic moments.

During the process of Li-ion storage in a battery, strain is developed in the electrode material due to volume change-induced stress which is an unavoidable phenomenon. Since in our case, 1, 2, 3, and 4 Lithium ions are being incorporated in the Fe₃SnC anode system, and the same is also causing biphasic constitution of the material, analysis of strain is certainly an important consideration to address. To understand these issues of stress/strain Scherrer equation (Williamson Hall plot, Figure 2.12 (a-d)) is one of the best techniques to estimate and elucidate the strain from the XRD data. Therefore, we obtained the W-H plots using the Scherrer method for different cases of interest. The slopes of these plots tell about the microstrain in the system. In our case, we have observed that the slope of the unlithiated Fe₃SnC is -ve (Figure 2.12a) which signifies the zero or very negligible strain [176]. But with successive lithiation, we have observed that slope becomes +ve which implies that strain is indeed generated by lithiation. With single lithiation, the slope is 0.00133 (Figure 2.12b) which rises to 0.00295 (Figure 2.12c) after the second lithiation. However, interestingly, after the third and fourth lithiation, the slopes are found to be about the same (0.00105) (Figure 2.12 d, e) within error. We note that the scatter of points is quite large hence the error bars are huge. Therefore nominally we should take the leading digits as 0.001 (first lithiation) change to 0.003 (second lithiation) and change back to 0.001 after the 3rd and 4th lithiation. This implies that first lithiation leads to a biphasic state with strain in Fe₃C (both Fe₃SnC and Fe₃C are cubic), which increases with second lithiation suggesting substantial strain and possibly structural distortion, but this provides a setting for further incorporation of the third and fourth lithium incorporation.

The Density of States (DOS) of the unlithiated Fe₃SnC , Fe₃C and all the stable lithiated phases of Fe₃C are presented in Figure 2.14(a-b) and 2.15(a-d) respectively.

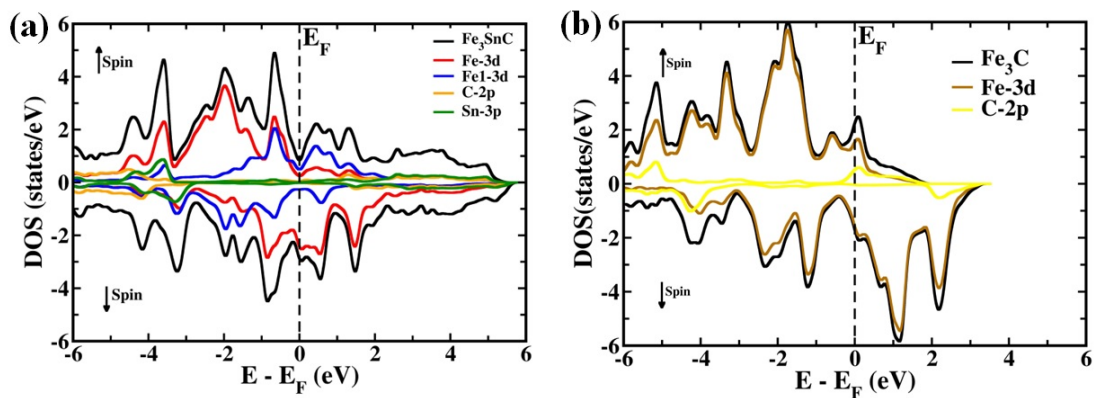


FIGURE 2.14: Represents the total density of states (DOS) of unlithiated systems (a) Fe₃SnC and (b) Fe₃C

With lithiation, the formation of structural distortion strain/stress alters the local coordination around the Fe atom and this leads to the changes in the magnetic moments

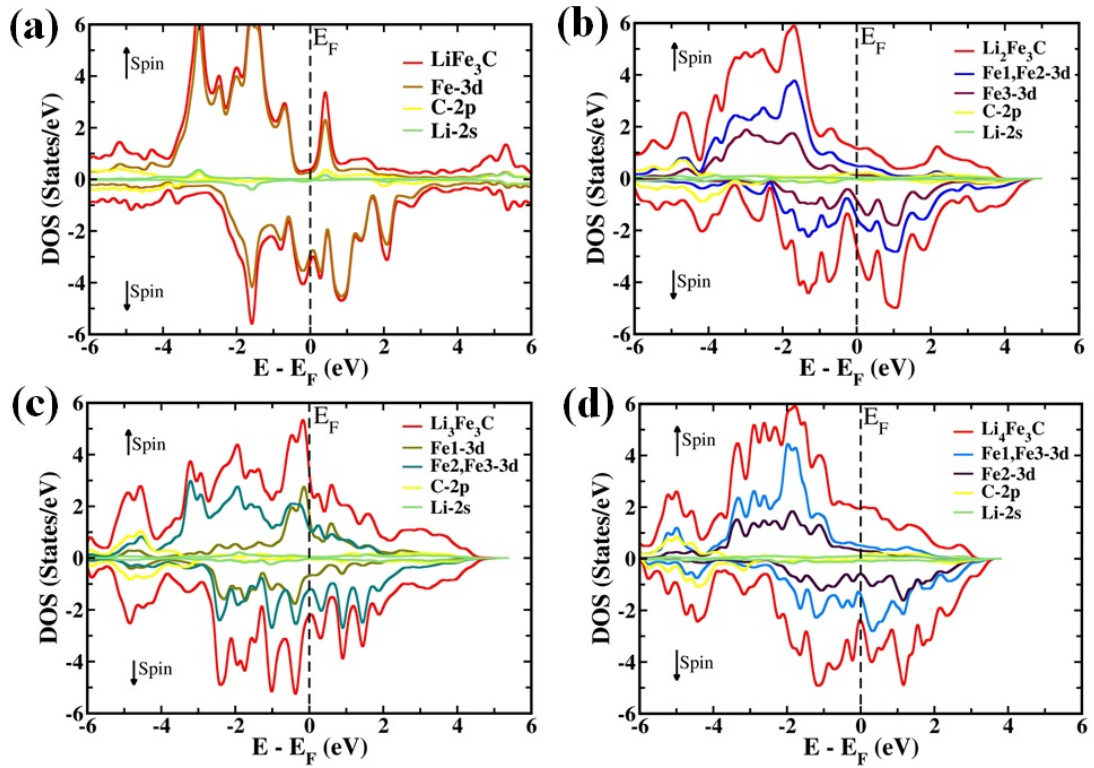


FIGURE 2.15: Represents the projected DOS of lithiated system: (a) Fe_3C (FM), LiFe_3C (FM) (b) $\text{Li}_2\text{Fe}_3\text{C}$ (FM) (c) $\text{Li}_3\text{Fe}_3\text{C}$ (FIM) (d) $\text{Li}_4\text{Fe}_3\text{C}$ (FM).

per Fe atom (Figure 2.13(a-d)). The above-mentioned structural distortions induce significant changes in hybridization between the atomic orbitals of Fe, C, and Li, which in turn result in changes in the DOS and magnetic properties of lithiated Fe_3C (Figure 2.15(a-d)). Importantly, this also creates large changes in the spin polarization (SP) of the corresponding lithiated systems.

To quantify this difference we compute the spin polarization (SP) using the following formula:[177–181]

$$\text{Spin Polarization (SP)} = \frac{N_{E_F}^\uparrow - N_{E_F}^\downarrow}{N_{E_F}^\uparrow + N_{E_F}^\downarrow}$$

$$\text{Degree of Spin Polarization: (DSP)} = |SP| \times 100\%$$

($N_{E_F}^\uparrow$) and ($N_{E_F}^\downarrow$) are the number of spins up and spin down states, respectively, at the Fermi level (EF). We find that for the pristine case SP=30.39%.

As seen from the data shown in Figure 2.15, all the lithiated cases of Fe₃C exhibit metallic behavior similar to the unlithiated Fe₃SnC and Fe₃C. Further, in all these cases, it is the Fe-d states that have dominant contributions to the DOS at the Fermi energy. More interestingly, the spin polarization at the Fermi level is significantly modulated. SP as a function of the number of Li atoms is shown in Figure 2.16 (red curve). We observe that except for Li₃Fe₃C (insertion of three Li-ions), where the system is in an FIM configuration (Figure 2.13b), lithium insertion significantly enhances the spin polarization at E_F as shown in Table 2.3 and 2.4. Noting that for the pristine cases of Fe₃SnC and Fe₃C the SP values are obtained as 30.39% and 13.64%, respectively, the largest enhancement (more than twice) is observed for single-lithiated Fe₃SnC.

Figure 2.16 also shows the average magnetic moment per Fe atom as a function of the number of Li atoms, both computed and experimentally measured, along with the spin polarization. We note that the computed and experimentally measured values of the magnetic moments show similar changes which are heartening and interesting. Further, the trends in the spin polarization as a function of the number of Li atoms follow the trends in the magnetic moments on the Fe atoms.

TABLE 2.3: Contribution of up and down spin of electrons at the Fermi level into the magnitude of spin polarization for Fe₃SnC.

Systems	($N_{E_F}^\uparrow$)	($N_{E_F}^\downarrow$)	(SP) = $\frac{N_{E_F}^\uparrow - N_{E_F}^\downarrow}{N_{E_F}^\uparrow + N_{E_F}^\downarrow} \times 100\%$
Fe ₃ SnC	1.28	2.36	30.39
LiFe ₃ SnC	0.65	3.87	71.23
Li ₂ Fe ₃ SnC	1.31	3.02	39.5
Li ₃ Fe ₃ SnC	2.60	2.04	12.09
Li ₄ Fe ₃ SnC	2.01	4.47	38.00

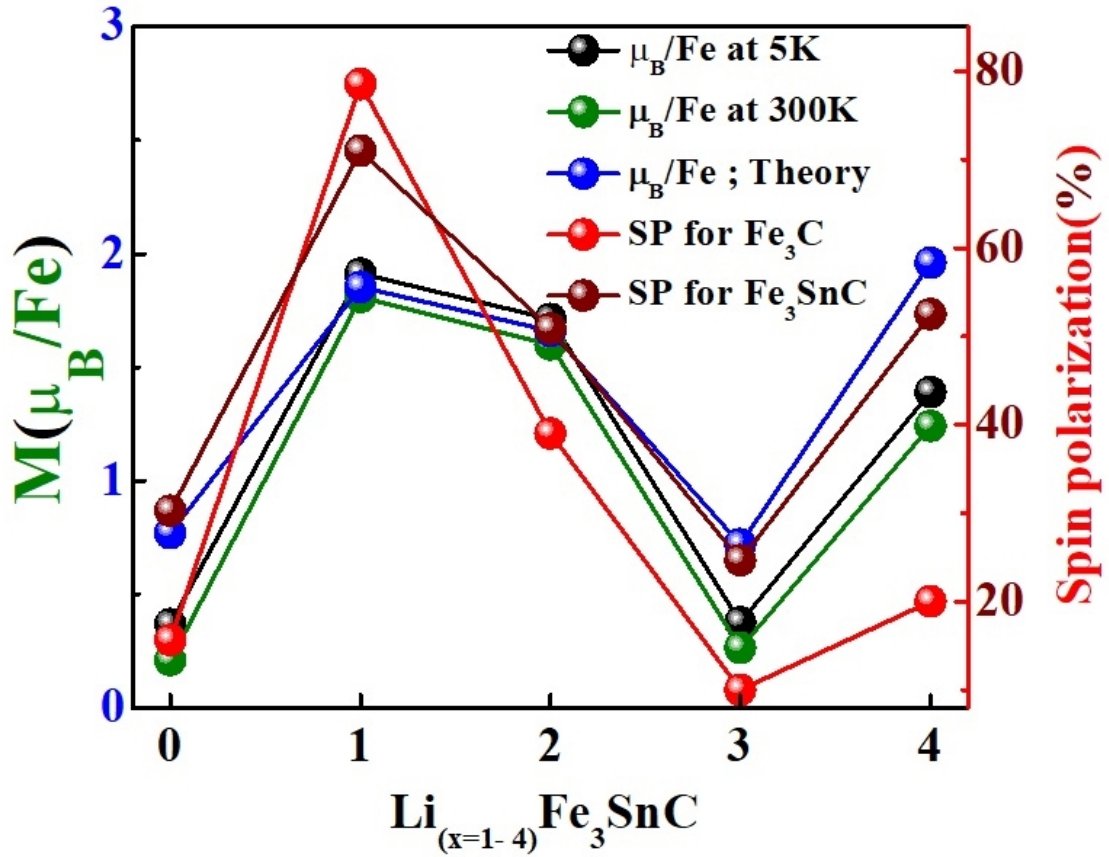


FIGURE 2.16: Black and the green curve represent the experimental magnetization per Fe atom at 5K and 300K, and the blue and cyan curve represents theoretically obtained magnetic moment per Fe atom for Fe_3SnC and Fe_3C , the red and wine color curve represents the magnitude of the degree of spin polarization for both the system.

TABLE 2.4: Contribution of up and down spin of electrons at the Fermi level into the magnitude of spin polarization for Fe_3C .

Systems	$(N_{E_F}^\uparrow)$	$(N_{E_F}^\downarrow)$	$(SP) = \frac{N_{E_F}^\uparrow - N_{E_F}^\downarrow}{N_{E_F}^\uparrow + N_{E_F}^\downarrow} \times 100\%$
Fe_3C	2.24	1.71	13.64
LiFe_3C	0.39	3.21	78.53
$\text{Li}_2\text{Fe}_3\text{C}$	1.16	2.64	39.01
$\text{Li}_3\text{Fe}_3\text{C}$	2.39	1.96	10.00
$\text{Li}_4\text{Fe}_3\text{C}$	2.21	3.34	20.00

2.4 Conclusions

In this combined theoretical and experimental study, we introduce the concept of iono-spintronics or Spintronic Battery wherein the accumulation and de-accumulation of Li-ion in the antiperovskite Fe_3SnC anode of a Li-ion half-cell concurrently and reversibly stores charge and spin; the latter mimicked by the experimental observation of non-monotonic changes in magnetization as a result of degree of lithiation, nominally depicted as $(\text{Li}_{x=1-4}\text{Fe}_3\text{SnC})$. It is noted experimentally that lithiation leads to a biphasic system in this particular case because of the affinity of Sn to form an alloy with Li. Thus with progressive lithiation changes occur in the stoichiometries and properties of the two phases, namely the Sn-Li alloy phase and lithiated or partially lithiated Fe_3C phase. The computer (DFT) calculations have been performed accordingly to account for these changes.

Given the structural and strain-related changes in magnetization upon lithiation and its degree, and their connection to spin polarization outlined here, we believe that this study would have broader and more interesting implications for a variety of structurally interesting materials systems, not limited only to the anti-perovskite intermetallic case discussed herein, wherein the structure-magnetism-spin polarization connection is acute. Also, the biphasic character encountered here may not occur in other systems wherein selective preferred interaction, as that of Sn in the present case, is not a possibility. With the rapid evolution of the fields such as the internet of things (IoT) a new breed of low-power consuming spintronics devices with novel functionalities is desired. Towards this end, effects such as concurrent storage of spins mediated by traditional battery architecture described here could add an interesting dimension.

Chapter 3

Surface-modified Antiperovskite Nitride Co_3CuN as a High Capacitive Anode Material Boosting Li-Ion Storage Capacity

Abstract

Surface modified antiperovskite nitride Co_3CuN with high specific capacity have been studied as high-performance anodes for Li-ion storage devices. Herein, an antiperovskite Co_3CuN was prepared via the hydrothermal method followed by calcination in the NH_3 atmosphere. A surface modified Co_3CuN ($\text{Cu}_{1-x}\text{NCo}_{3-y}/\text{CuFeCo}$) was also designed and studied as an anode material for Li-ion battery (LIB), the material was noted to deliver a reversible capacity of $\sim 1150 \text{ mAhg}^{-1}$ at a current density of 0.1 Ag^{-1} whereas pure Co_3CuN showed the reversible capacity of $\sim 408 \text{ mAhg}^{-1}$ at a current density of 0.1 Ag^{-1} . It also exhibited very good retention of the initial capacity of surface reconstructed Co_3CuN after 350 charge-discharge cycles which is more than 62% retention of capacity at 0.1 Ag^{-1} . Finally, the Li-ion full cell performance of surface reconstructed Co_3CuN was studied using $\text{LiNi}_{0.5}\text{Mn}_{0.3}\text{Co}_{0.2}\text{O}_2$ (NMC-532) as a high-capacity cathodic counterpart, which showed a very high reversible capacity of 600 mAhg^{-1} (based on the anode weight) at an applied current density of 0.1 Ag^{-1} with 35% retention of capacity after 100 cycles. This work offers new promising strategies to improve a higher reversible capacity of antiperovskite as an anode material for Li-ion battery applications.

3.1 Introduction

Lithium-ion (Li-ion) batteries are the most reliable sources of green energy, and the application of Li-ion rechargeable batteries in the real system makes them the most promising energy source. As a substitute energy storage technology, lithium-ion batteries (LIBs) can play a vital role in displacing fossil fuels without emitting greenhouse gases, as they efficiently store energy for long periods in applications ranging from portable electronic devices to electric vehicles [18]. The excellent stability, easy fabrication, and simple electrochemistry attract great attention in the commercial market all over the world. After the first commercialization of the Li-ion battery by SONY company in 1990 the demand for this battery continuously increases where LiCoO_2 was used as cathode and graphite used as anode material. Despite the huge success of this commercialized battery, intense research is continuously being hunted on the development of new novel materials with very high energy and power density and excellent stability for both the anode and the cathode electrode materials [182]. Any new anode and cathode materials should deliver better than the existing ones on certain important aspects such as cyclic stability, voltage hysteresis, operating potential window, capacity, and current stability [18, 182–184]. Dendrite formation prevents the direct use of Li metal as an anode, after that several different anode materials have been explored. Alloying, conversion, and intercalation, these three types of materials mostly fall into the category of anode material [18] though all these types of anode materials have some drawbacks. Different alloying materials such as silicon [185, 186] (Si), Tin (Sn) [167], bismuth (Sb) [187], etc these anode materials have other issues of capacity fading, volume expansion, and pulverization [188–191]. Various strategies have been involved to improve the performance of all these anode materials by controlling the capacity fading and volume expansion, but all the issues have partially been resolved [189]. The conversion material has distinct difficulties of high operating potential and high voltage hysteresis [192]. However, in terms of cycling and rate stability intercalation type materials are the best but it also has some limitations of low capacity [193]. From the commercial perspective, all these anode materials are not able to fulfill the required specification except graphite.

Many 2D, 3D oxides, carbides, nitrides, chalcogenides, and perovskites materials of different crystallographic sizes such as bulk, layer, and nanomaterials have been explored as new novel anode materials for Li-ion battery electrodes but each of them has some disadvantages and possess through some limitations. Nanomaterials have certain drawbacks in terms of applicability, such as limited density, poor electrical conductivity, and significant danger of surface side reactions. To overcome the disadvantages of nanomaterials the idea of core-shell nanostructure was introduced in the last 20 years [194]. The promising core-shell anode materials with different crystal types and different coating

layers, (generally carbon and oxide) were reported such as core-shell Si@C nanowires, and nanotubes [195–199], Core double-shell Si@SiO₂@C nanocomposite [200], Sn@C [201], Sn@Cu core-shell nanomaterials [166, 202], core-shell Fe₃O₄@C nanowires [203–206], core-shell SnO₂@C nanoparticle [170, 207–215], TiO₂@Sn core-shell [216–218]. The core is the most important component with different functional qualities, while the outer shell serves as a protective layer or adds new features to the core. Core-shell composites can also be assembled into zero–three-dimensional (0–3D) morphologies in the nanometre to micrometer scale. Core-shell structures often display superior physical and chemical properties over their single-component counterparts and hence are extensively used in optics, magnetism, biomedicine, catalysis, energy conversion, and storage [219–228].

Antiperovskite with the different chemical environments such as lithium halide hydroxide, oxyhalide, cluster-based, hydride-based, and transition metal-based antiperovskites [3] has been explored as solid-state electrolyte and cathode material for Li-ion batteries [3]. Based on the literature report there are very few reports of the antiperovskite anode materials with less capacity [4, 229]. A new family of Li and Na rich antiperovskite was reported as high ionic conducting material for solid-state electrolytes [3, 101]. The Li-rich antiperovskites were also proposed to serve as cathode materials by possible cation and/or anion manipulations [3, 230]. Antiperovskite carbide and nitride have a very high density of state (DOS) at the Fermi level (E_F) and exhibit metallic signature and it shows very high superconducting properties like in MgCNi₃ and CuNNi₃ [49, 104]. The highly conducting property of nitride antiperovskite leads to a promising application in the field of electrocatalysis and shows excellent (HER, OER) performance [69, 231–235], and these properties also encourage further applications in the field of energy storage in LIB.

Herein for the first time pure antiperovskite Co₃CuN and surface modified Co₃CuN-based core-shell like the structure of (Cu_{1-x}NC_{3-y}/CuFeCo) material is explored for a LIB as an anode with a very high capacity and outstanding stability. Antiperovskite Co₃CuN was synthesized via hydrothermal method followed by calcination in ammonia atmosphere. A surface reconstructed Co₃CuN (Cu_{1-x}NC_{3-y}/CuFeCo) was synthesized using Cu excess Co₃CuN followed by treatment with aqueous FeCl₃ solution which delivered a reversible capacity of 1150 mAh/g at a current density of 0.1 A/g whereas pure Co₃CuN showed 408 mAh/g at the same current density. Finally, the Li-ion full cell performance of surface reconstructed Co₃CuN was studied using LiNi_{0.5}Mn_{0.3}Co_{0.2}O₂ (NMC-532) as a high-capacity cathodic counterpart, which showed a very high reversible capacity of 600 mAh g⁻¹ (based on the anode weight) at an applied current density of 0.1 A/g with 35 retention of capacity after 100 cycles. This work offers new promising strategies to improve a higher reversible capacity of antiperovskite as an anode material for Li-ion battery applications.

3.2 Experimental Details

3.2.1 Materials

All the analytical grade reagents were used directly without further purification. Cobalt acetate (Co(CH₃COO)₂·4H₂O), Hexamethylenetetramine (HMT), Copper acetate, Ferric chloride hexahydrate (FeCl₃·6H₂O) were purchased from Sigma-Aldrich Chemical Co. Millipore water was used for all the experiments.

3.2.2 Synthesis of Co₃CuN

A hydrothermal method has been used to synthesize antiperovskite nitride Co₃CuN. In the typical synthesis, 1.5 mmol cobalt acetate, 0.5 mmol copper acetate, and 4 mmol HMT were dissolved in 50 mL deionized water and mixed it properly. The mixture was then transferred into a 100 mL Teflon-lined autoclave and then heated at 120°C for 12 h. After aftercooling down to room temperature, the precipitate was collected through centrifuging (1000 rpm for 15 minutes) and washed with deionized water and ethanol 3 to 4 times. The collected product was dried in a vacuum oven at 80°C overnight. The dried product was then ground well and calcined at 420°C for 4 h under NH₃ atmosphere in a tube furnace. After cooling down to room temperature, the furnace atmosphere was replaced with N₂ flow. The final product was collected for further characterization.

3.2.3 Synthesis of Cu Excess Co₃CuN (Co₃CuN + Cu)

Co₃CuN + Cu has been synthesized using a similar protocol of Co₃CuN using excess copper acetate during the hydrothermal process.

3.2.4 Synthesis of Surface modified Co₃CuN (Cu_{1-x}NCo_{3-y}/CuFeCo)

A solid product of Cu excess Co₃CuN (Co₃CuN + Cu) was used as a starting material to synthesize Cu_{1-x}NCo_{3-y}/CuFeCo. A desired amount of Co₃CuN + Cu was mixed in an aqueous solution of the appropriate amount of FeCl₃·6H₂O and the resulting solution was stirred for 25 min at room temperature. Finally, after 25 min, the solid sample was collected through centrifugation (1000 rpm for 15 minutes) followed by washing with deionized water and ethanol 3 to 4 times and kept in the oven at 80°C overnight.

3.2.5 Characterization

The powder XRD or PXRD measurement was carried out to analyze the crystal structure of the materials using the Bruker D8 advanced X-ray diffractometer (Cu-K α $\lambda = 1.54178\text{\AA}$). The morphology of the obtained solid products was studied via field-effect scanning electron microscopy (FESEM, ZEISS-Ultra Plus-4095). High-resolution transmission electron microscopy (HRTEM) image was obtained on a transmission electron microscope (a Jeol, JEM 2200FS at 200 keV) with a selected area electron diffraction (SAED) pattern.

3.3 Electrochemical Characterizations

3.3.1 Fabrication of Electrode and Coin Cell

The electrodes for both the Co₃CuN and Cu_{1-x}NCo_{3-y}/CuFeCo materials were made by mixing the active material, conducting carbon (Acetylene black) and polyvinylidene difluoride (PVDF) as a binder (Sigma-Aldrich; weight ratios were maintained as 7:2:1) in N-methyl-2-pyrrolidone (NMP) solvent and coating the slurry onto a Cu foil. The electrodes were dried in an oven at 80°C for overnight. The dried electrodes were then cut into round electrodes by using a disc-cutter. We made the 2032-type coin cells in an Ar-filled glovebox. For all the studies, LiPF₆ electrolyte was used in a solvent combination of 1:1 ethylene carbonate (EC) and dimethyl carbonate (DMC) along with 2 wt % fluoroethylene carbonate (FEC; Sigma Aldrich) as an additive. Celgard 2500 was used as the separator.

3.3.2 Fabrication of Full Coin Cell

A full cell was fabricated using LiNi_{0.5}Mn_{0.3}Co_{0.2}O₂ (NMC-532) as the cathode having an anode to cathode mass ratio 1 : 3. The operating potential window was kept at 2 to 4 V and 1M LiPF₆ in EC/DMC (1 : 1 v/v) was used as the electrolyte with 2 vol % of EFC additive. A total amount of 200 μL of electrolyte was used. The capacity of the full cell was calculated based on the anode weight.

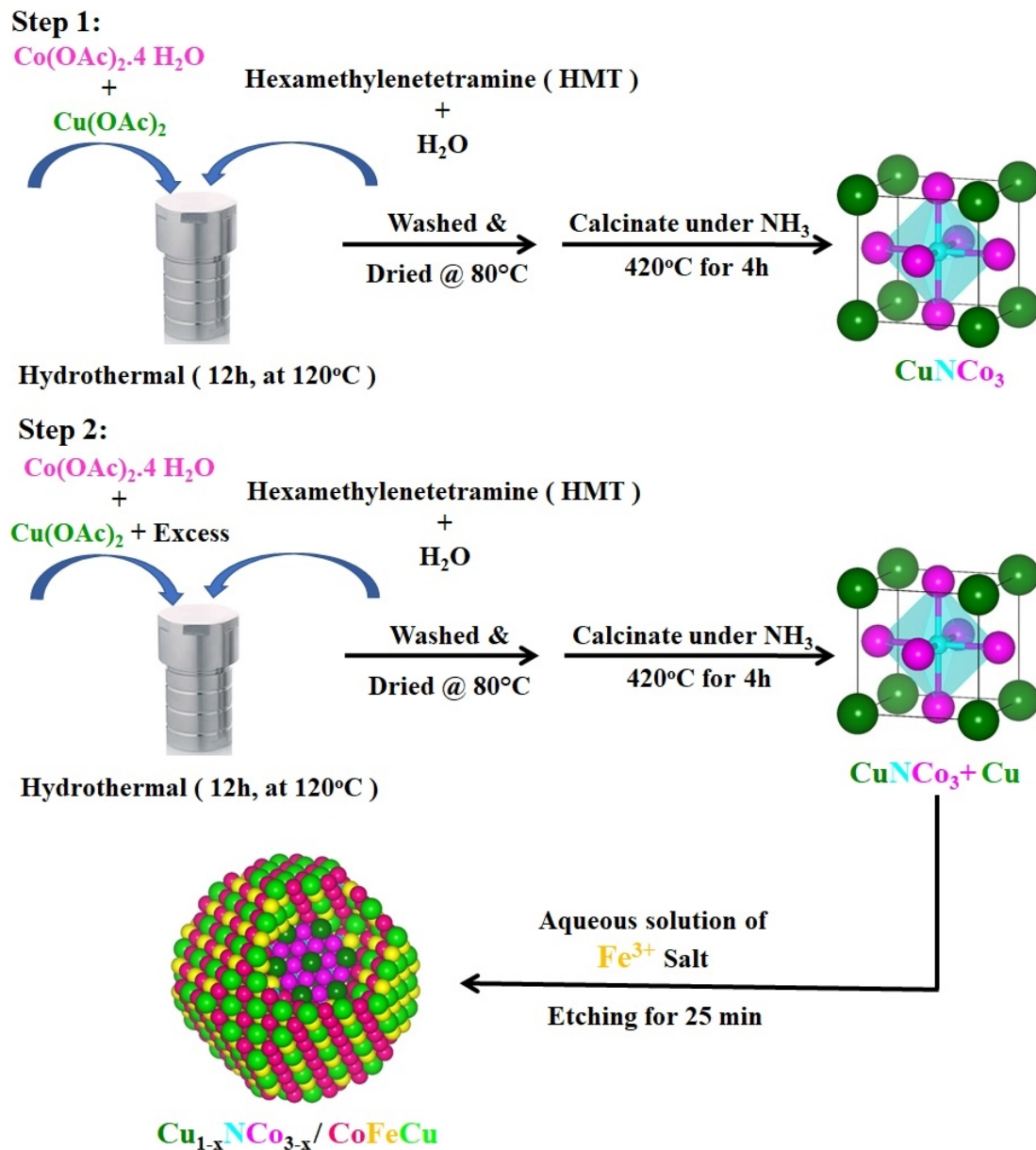


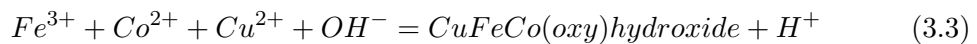
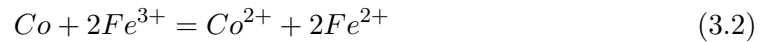
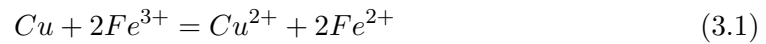
FIGURE 3.1: Schematic representation of Co_3CuN and $\text{Cu}_{1-x}\text{NCo}_{3-y}/\text{CuFeCo}$ synthesis.

3.4 Results and Discussion

3.4.1 Synthesis Mechanism of Co_3CuN and $\text{Cu}_{1-x}\text{NCo}_{3-y}/\text{CuFeCo}$

The fabrication procedure of the Co_3CuN and surface reconstructed $\text{Cu}_{1-x}\text{NCo}_{3-y}/\text{CuFeCo}$ are schematically illustrated in Figure 3.1. The formation mechanism of the core-shell is similar to the reported mechanism of core-shell CuNNi_3 [69]. As per the report published by Zhu et al. initially, copper was dissolved according to the chemical reaction (1) [69, 236]. After the addition of $\text{FeCl}_3 \cdot 6\text{H}_2\text{O}$ into an aqueous solution of Cu excess Co_3CuN ($\text{Co}_3\text{CuN} + \text{Cu}$), Co and Cu in the antiperovskite structure were partially

etched by Fe^{3+} according to the reactions 3.1 and 3.2. Significantly, Fe^{3+} , Cu^{2+} , and Co^{2+} ions were hydrolyzed to form a CoFeCu (oxy) hydroxide colloid and H^+ (reaction 3.3) [69, 237, 238]. Hydrolysis was promoted due to the consumption of H^+ . As a result, CuFeCo was deposited on the surface of the antiperovskite which leads to the formation of $\text{p-Cu}_{1-x}\text{NCo}_{3-y}/\text{CuFeCo}$ core-shell like material.



3.4.2 Structural Characterization

It is a well known fact that particle size plays an important role in any chemical reactivity. The nanoparticle with a small crystalline size increases the surface area and has good surface energy could enhance the chemical reactivity. The PXRD patterns of Co_3CuN are presented in Figure 3.2(a) and the sharp peak in the PXRD patterns reveals the pure phase of the Co_3CuN . All the peak positions and corresponding planes are indicated in Figure 3.2(a) which are well matched with the earlier reported [126] PXRD pattern.

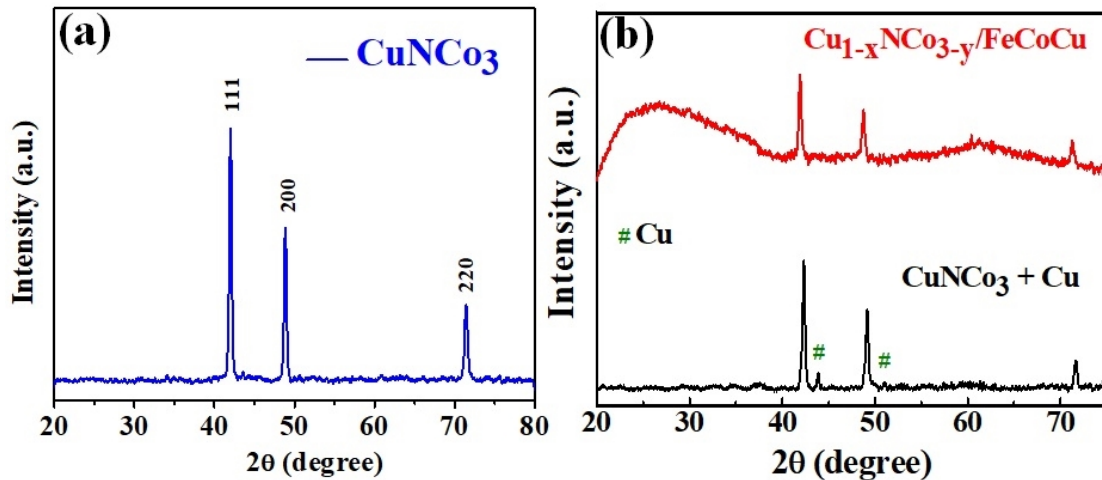


FIGURE 3.2: Powder XRD patterns of (a) Co_3CuN ; (b) Cu excess Co_3CuN (black line) and surface reconstructed Co_3CuN ($\text{Cu}_{1-x}\text{NCo}_{3-y}/\text{CuFeCo}$) (red).

The powder XRD pattern of the $\text{Co}_3\text{CuN} + \text{Cu}$ complex and the surface reconstructed CuNCo_3 ($\text{Cu}_{1-x}\text{NCo}_{3-y}/\text{CuFeCo}$) have been presented in Figure 3.2(b). In the case of Cu excess Co_3CuN , two small peaks at $2\theta = 43.93^\circ$ and 51.04° correspond to metallic Cu and the remaining three strong peaks correspond to the Co_3CuN . After etching

by Fe³⁺ (FeCl₃.6H₂O) the peak associated with metallic Cu was not observed in the case of Cu_{1-x}NCo_{3-y}/CuFeCo, suggesting that metallic copper successfully dissolved. Additionally, the three main peaks of Co₃CuN almost remain the same except there is a slight shift of the peak position towards the left side and there is a little drop in the intensity which assisted that the surface elements of the core material of Co₃CuN participate for making the amorphous shell around the core which is clearly illustrated in the PXRD pattern, the broad region between the 2θ range from 20° to 39°.

3.4.3 Morphological Characterization

To further understand the skeleton of the crystal structure and its morphology HRTEM was recorded for Co₃CuN and Cu_{1-x}NCo_{3-y}/CuFeCo. SEM image of Co₃CuN Shown in Figure 3.3(a) showed the nanowire morphology. The HRTEM images of Co₃CuN exhibited an assembly of nanoparticles into a nanowires presented in Figure 3.3(b). The average size of a Co₃CuN nanoparticle is about 50 nm. Figure 3.3(c) illustrated the lattice fringes of the Co₃CuN correspond to the (111) plane with an interplanar lattice spacing of 0.22 nm and the corresponding lattice constant of the unit cell of Co₃CuN is 3.75Å which nicely corroborates with our theoretically obtained optimized lattice constant of 3.74Å using density functional theory (DFT) and the crystal unit cell of Co₃CuN is presented in Figure 3.3(d). The stoichiometry of the sample is confirmed by EDS shown in Figure 3.3 which suggests the exact atomic ratio of 3:1:1 of the sample. The elemental mapping shown in Figure 3.4 confirmed the homogeneous distribution of the elements.

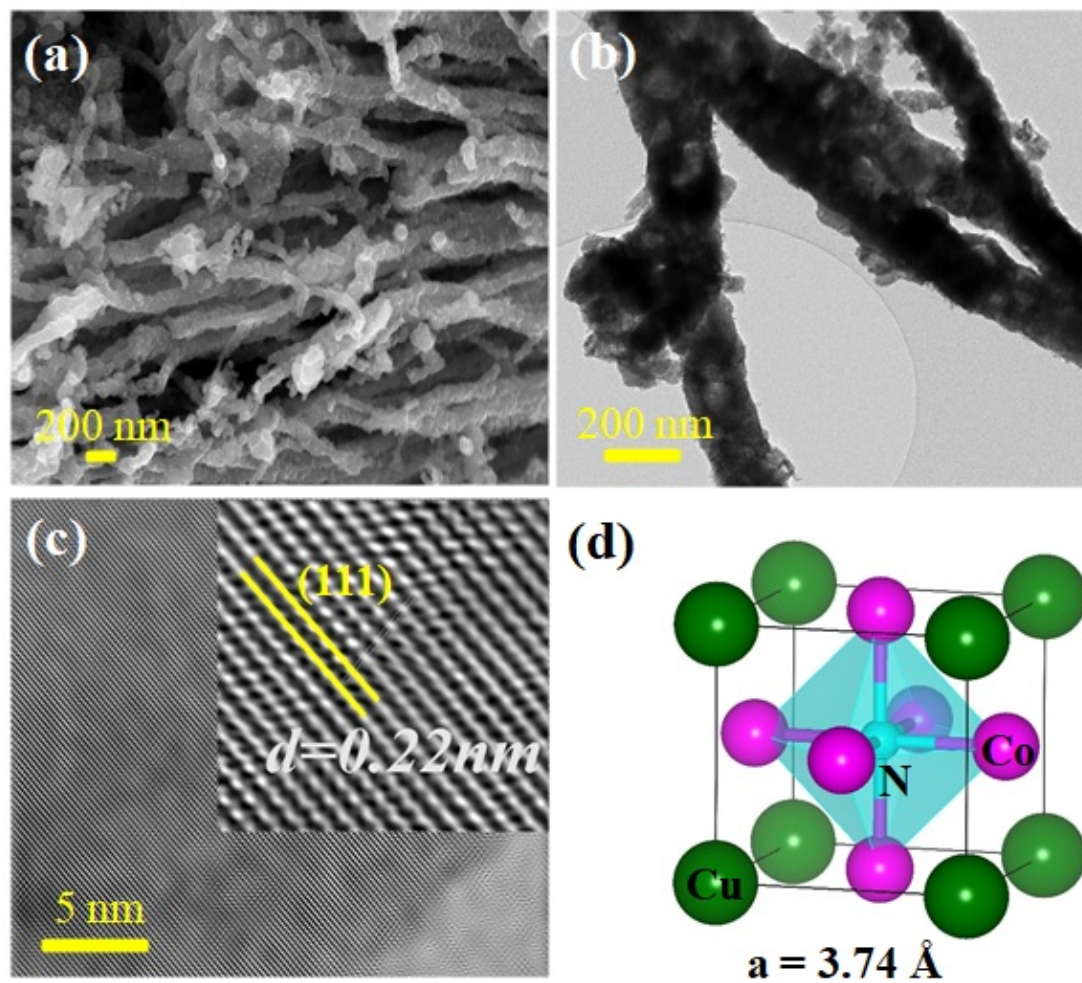


FIGURE 3.3: (a) SEM; (b) HRTEM image of CuNC_3 . (c) FFT image corresponds to the (111) planes of Co_3CuN ; (d) Unit cell representation of Co_3CuN .

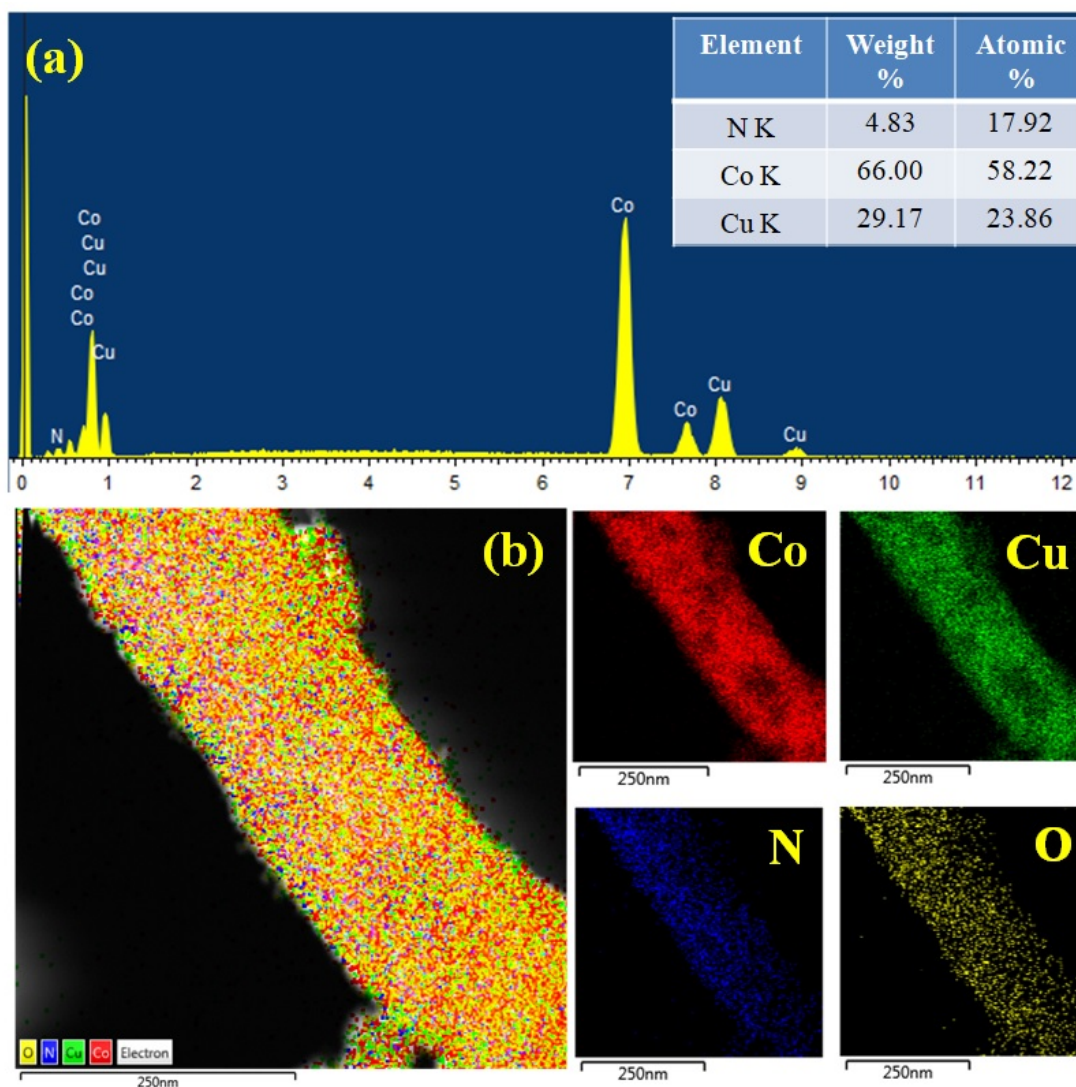


FIGURE 3.4: (a) EDAX analysis; (b) Elemental mapping of Co_3CuN .

The HRTEM image is shown in Figure 3.5a. demonstrated both the core and the shell-like region while the white dotted line differentiates the core and shell region. The FFT image of the core-shell has been recorded to analyze the detailed crystal nature of the core and shell which is illustrated 3.5b. The zoomed image presented in Figure 3.5b(i, ii, iii) represented the shell, core, and the interface region between the core and shell respectively. Figure 3.5b(i) illustrated the amorphous nature of the shell, Figure 3.5b(ii) illustrated the cubic crystalline region of the core (Co_3CuN), and Figure 3.5b(iii) demonstrated the interface region between the amorphous and crystalline system of the core-shell.

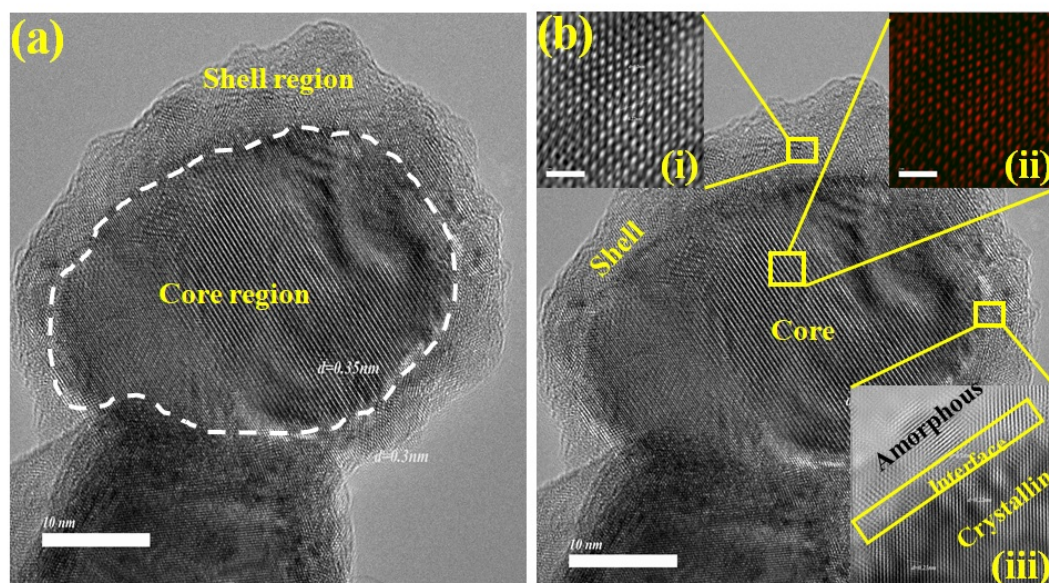


FIGURE 3.5: (a-b)HRTEM image of the core-shell of $\text{Cu}_{1-x}\text{NCo}_{3-y}/\text{CuFeCo}$.

The EDS data of the $\text{Cu}_{1-x}\text{NCo}_{3-y}/\text{CuFeCo}$ is presented in Figure 3.6(a). Elemental mapping and line-scan spectra shown in Figures 3.6(b) and 3.6(c), confirmed the presence of Co, Cu, Fe, and N. The elemental mapping obtained from the $\text{Cu}_{1-x}\text{NCo}_{3-y}/\text{CuFeCo}$ confirmed that the elements of the core consist of Co, Cu, and N whereas elements of the shell consist of Fe, Cu, and Co shown in Figure 3.6(b). Furthermore, line scan spectra shown in Figure 3.6(c) exhibited a strong signal of Co, Cu, and N at the core region which implies that the core consists of pure Co_3CuN . The strength of the Fe signal at the core is very small but it extended throughout the core-shell, which indicated the core-shell like structure. All the analysis confirmed the core-shell like the structure of the $\text{Cu}_{1-x}\text{NCo}_{3-y}/\text{CuFeCo}$

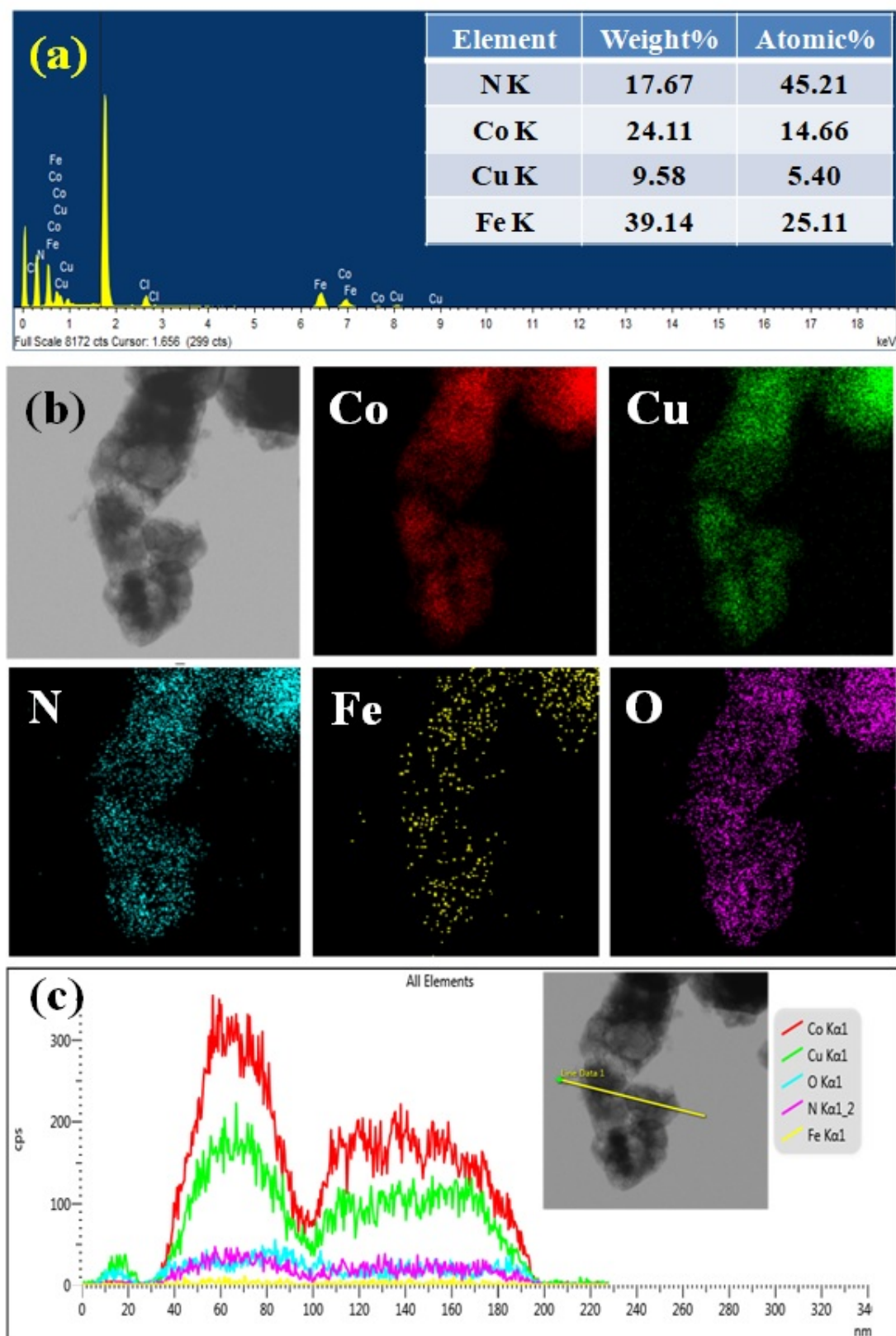


FIGURE 3.6: (a) Illustrates the elemental mapping of the core-shell ($\text{Cu}_{1-x}\text{NCo}_{3-y}/\text{CuFeCo}$) element (b) Line scan of the core-shell.

3.4.4 Electrochemical Characterization

The electrochemical performance of Co_3CuN and $\text{Cu}_{1-x}\text{NCo}_{3-y}/\text{CuFeCo}$ materials were tested in a LiPF_6 medium using a coin cell to analyze the LIBs' performance. It has been observed that Co_3CuN showed the first discharge capacity of 950 mAh/g presented in Figure 3.7(a). The conducting nature and the presence of the high amount (60%) of cobalt (Co) and also the presence of nitrogen (N) could lead to the enhancement of the capacity. However, from the second cycle, the reversible capacity obtained 412 mAh/g. Co_3CuN showed a reversible capacity of 210 mAh/g after 350 cycles with 50% retention presented in 3.7(b). The rate performance of the battery was measured with different current densities of 100, 200, 300, 400, and 500 mA/g and Co_3CuN showed a specific capacity of 225 mAh/g at a high current density of 500 mA/g (Figure 3.7(c)). The decay observed in the case of Co_3CuN with the increasing number of cycles could be due to the volume expansion of the cell as evident from the theoretical study shown in Figure 3.8 where with successive lithiation (1-5Li) inside the octahedral and tetrahedral interstitial void space a significant volume change was observed.

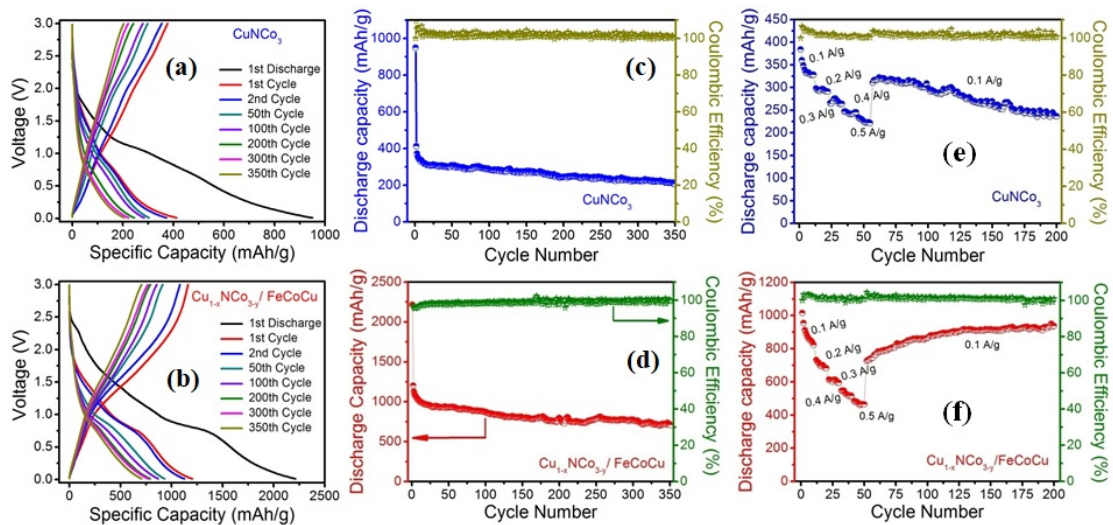


FIGURE 3.7: Charge-discharge profile in the half cell configuration (a) Co_3CuN and (c) $\text{Cu}_{1-x}\text{NCo}_{3-y}/\text{CuFeCo}$; Stability, efficiency and rate performance of (b) Co_3CuN and (d) $\text{Cu}_{1-x}\text{NCo}_{3-y}/\text{CuFeCo}$.

To further improve the performance of the battery we have modified the surface of Co_3CuN and the detailed synthesis protocol has been discussed in the experimental section. Several strategies have been implemented to control or absorb the volume expansion of the battery during the charging and discharging of metallic or conducting anode materials [194]. One such strategy is the preparation of core-shell nanostructure which could improve the performance by increasing the structural stability and storage capacity of the Li-ion batteries. It was reported that to enhance the electrochemical performance of the family of alkali ions batteries (AIBs) amorphization engineering

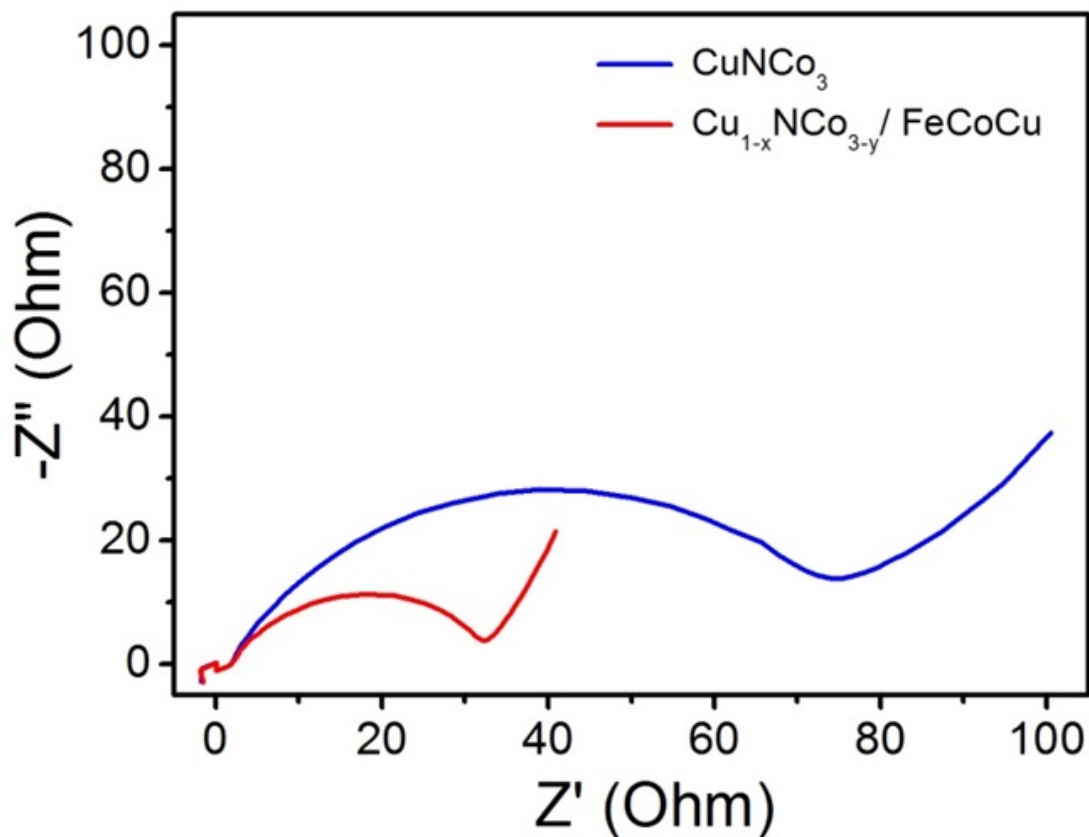


FIGURE 3.8: The Electrochemical impedance spectroscopic analysis for the cell (fresh cell and after 5 cycles) impedance of the pure and core-shell of Co_3CuN .

received much attention due to the unique functionalities of amorphous phases [22, 239–248]. Various important factors are there for the electrochemical performances of crystalline host material such as the available energetically equivalent sites for guest-ion occupation/transport, crystal orientation, structural stability, phase transition, the spatial dimension of ion migration, defects in crystal, and the stoichiometric limitation of ion insertion [249–251]. Compared to those crystalline electrodes, the amorphous counterparts could deliver much improved specific capacities and long-term cyclability over a wide potential window [22, 239, 243]. This is because the amorphous phases exhibit several advantages, such as improved ionic intercalation/deintercalation kinetics due to the existence of percolation pathways, a larger free volume, and a higher specific surface area to accommodate lattice distortions [239]. A thin amorphous layer (10 nm) around the surface of the pure Co_3CuN was decorated to improve the battery performance of Co_3CuN . The performance of the $\text{Cu}_{1-x}\text{NCo}_{3-y}/\text{CuFeCo}$ has been tested and observed the increase in the specific capacity more than twice as compared to the pure Co_3CuN presented in Figure 3.7b which is much higher than the earlier reported study based on the 3D carbide antiperovskite Fe_3SnC by Roy et al.[4] and Co_3ZnC by Chen et al [229]. The first discharge capacity of 2200 mAh/g at a current density of

100 mA/g was observed. After 350 cycles the reversible capacity becomes ~ 710 mAh/g which is very high as compared to the pure Co_3CuN with excellent stability (59 retention) shown in Figure 3.7b. The rate of performance has been verified with different current densities of 100, 200, 300, 400, and 500 mA/g and it shows the decay of the capacity with increasing the current densities but the capacity at 500 mA/g is ~ 465 mAh/g which is very high as compared to the Co_3CuN (225 mAh/g).

The capacity increases of the core-shell suggest the major role of the amorphous nature of the shell consists of multimetal oxyhydroxide of CuFeCo deposited on the crystalline surface of the Co_3CuN . The presence of the porosity, large surface area and presence of the multi redox center (see the XPS data in Figure 3.9) for Li-ion to react helped to allow more Li-ion to pass into the core-shell structure which could be the reason to improve the capacity and structural stability of the $\text{Cu}_{1-x}\text{NCo}_{3-y}/\text{CuFeCo}$. It is well-known fact that metal oxyhydroxide has very good electronic conducting properties [252–254]. After forming the metal oxyhydroxide shell on the surface of the core, the core and shell together in $\text{Cu}_{1-x}\text{NCo}_{3-y}/\text{CuFeCo}$ increased the electronic conductivity (Figure 3.8) of the system and accelerate the chemical redox reaction of Li-ion with the electrode and hence increase the performance of the battery. Electrochemical performance of the antiperovskite $\text{Cu}_{1-x}\text{NCo}_{3-y}/\text{CuFeCo}$ was comparable with the literature reports presented in Table 3.1 which indicate the best performance of our materials among any perovskite and anti-perovskite based reported materials to date according to our best knowledge.

We fabricated a practical LIB using $\text{Cu}_{1-x}\text{NCo}_{3-y}/\text{CuFeCo}$ as anode and $\text{LiNi}_{0.5}\text{Mn}_{0.3}\text{Co}_{0.2}\text{O}_2$ (NMC-532) as a cathode considering the above-mentioned advantages of the $\text{Cu}_{1-x}\text{NCo}_{3-y}/\text{CuFeCo}$. A very high reversible capacity of ~ 550 mAh/g (based on the anode weight) at an applied current density of 0.1 A/g was observed with more than 50 retention of capacity after 50 cycles (Figure 3.10).

3.4.5 Post-cycling characterisation of $\text{Cu}_{1-x}\text{NCo}_{3-y}/\text{CuFeCo}$

To check the morphology of $\text{Cu}_{1-x}\text{NCo}_{3-y}/\text{CuFeCo}$, we performed ex-situ post-cycling FESEM of the electrodes. FESEM images in Figure 3.11 of $\text{Cu}_{1-x}\text{NCo}_{3-y}/\text{CuFeCo}$ fresh, after 1st cycles and 100 cycles revealed that a uniform SEI layer developed on the electrode surface, which leads to the stable anodic performance. Furthermore, the morphology of the material was intact after 100 cycles which proved the robustness of the material.

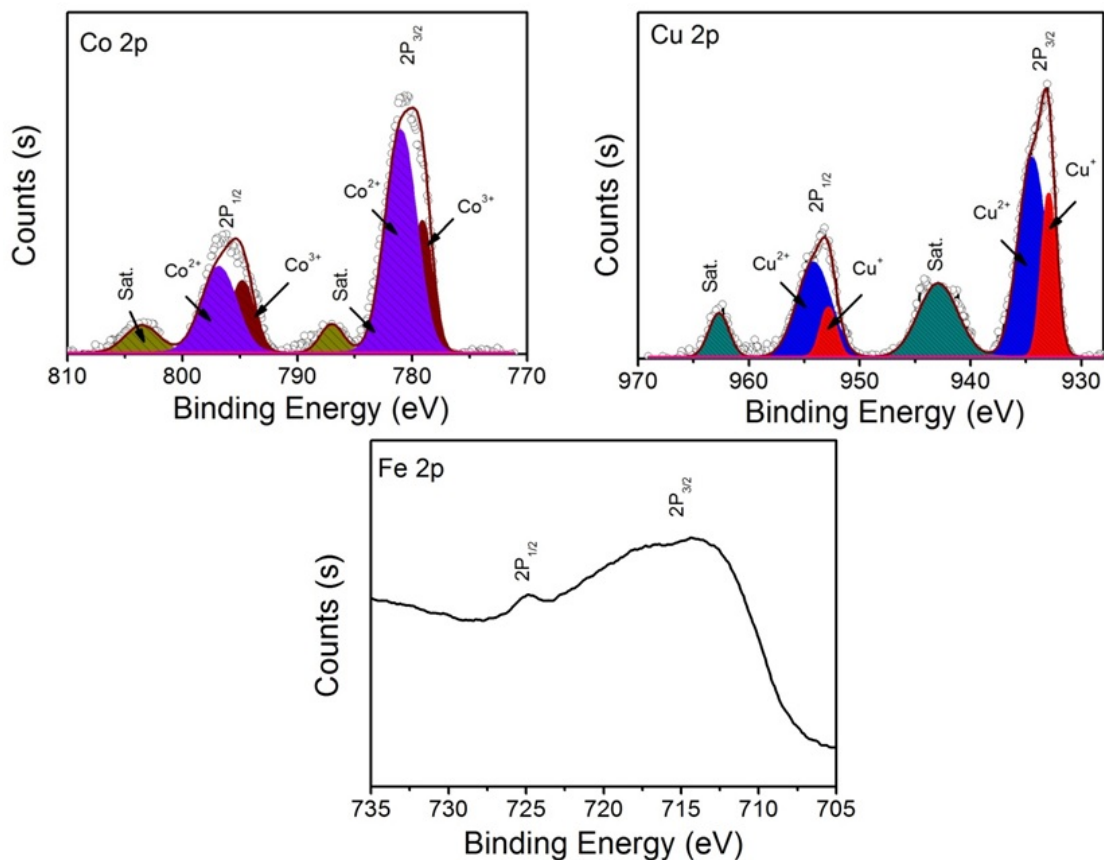
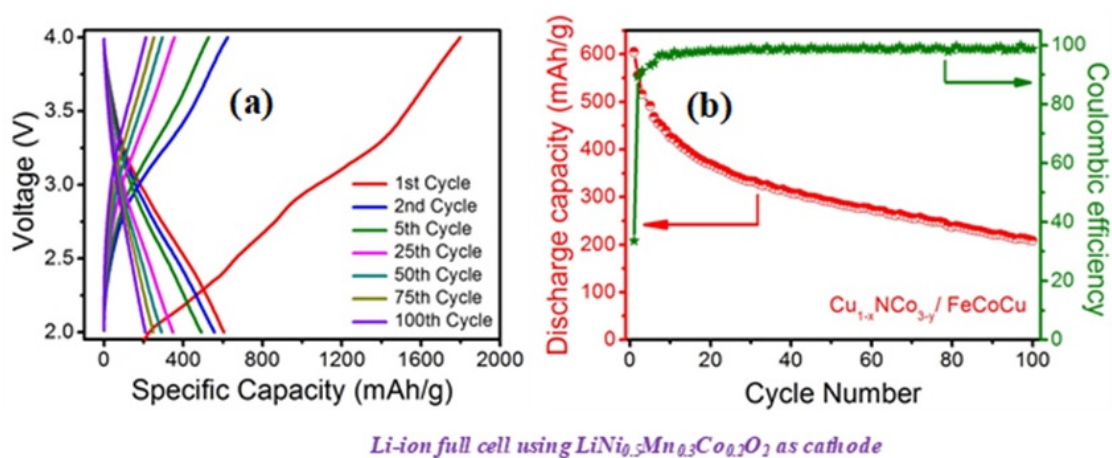


FIGURE 3.9: The XPS spectra of Fe, Co, and Cu elements of the core-shell of Co_3CuN .



Li-ion full cell using $\text{LiNi}_{0.5}\text{Mn}_{0.3}\text{Co}_{0.2}\text{O}_2$ as cathode

FIGURE 3.10: Battery performance: (a) Charge-discharge profile in the full cell configuration using NMC-532 as the cathode and $\text{Cu}_{1-x}\text{NCo}_{3-y}/\text{FeCoCu}$ as anode; (b) Stability and efficiency data of the full cell.

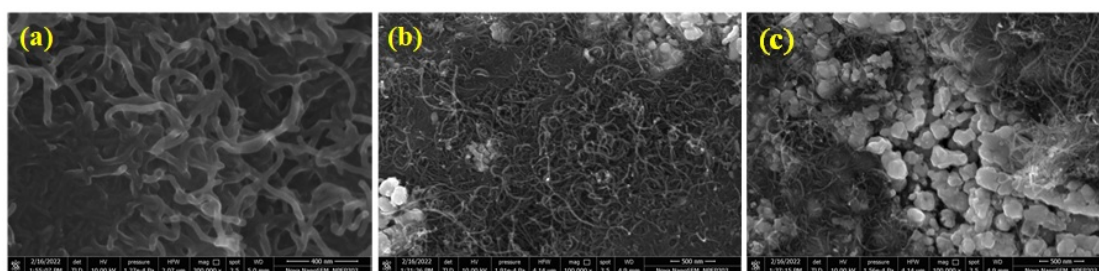


FIGURE 3.11: Post cycling ex-situ FESEM images of (a) fresh electrodes; (b) after 1st cycle; and (c) after 100th cycle of $\text{Cu}_{1-x}\text{NCo}_{3-y}/\text{CuFeCo}$ electrodes in the half cell configuration.

TABLE 3.1: Comparison table of capacity between perovskite and antiperovskite as an anode material for Li-ion battery

Materials	Initial DC	CD	First RC	Stable capacity	References
Co_3CuN Perovskite	2200 mAh/g	100 mA/g	1150 mAh/g	710 mAh/g	our Work
HoFeO_3 Perovskite	597 mAh/g	100 mA/g	352 mAh/g	120 mAh/g	[255]
$\text{Li}_{0.24}\text{La}_{0.59}\text{O}_3$ Perovskite	550 mAh/g	100 mA/g	301 mAh/g	1000 mAh/g	[256]
PbTiO_3 Perovskite	620 mAh/g	4.4 mA/g	410 mAh/g	70 mAh/g	[257]
PbZrO_3 Perovskite	368 mAh/g	3.87 mA/g	291 mAh/g	20 mAh/g	[257]
CsPbBr_3 Perovskite	376 mAh/g	30 mA/g	376 mAh/g	10 mAh/g	[258, 259]
CsPbI_3 Perovskite	151 mAh/g	40 mA/g	150 mAh/g	100 mAh/g	[260]
SrVO_3 Perovskite	551 mAh/g	2 A/g	347 mAh/g	2500 mAh/g	[261]
CaMnO_3 Perovskite	708 mAh/g	100 mA/g	208 mAh/g	500 mAh/g	[262]
CsPbBr_3 Perovskite	549 mAh/g	45 mA/g	480 mAh/g	1500 mAh/g	[263]
CsPbCr_3 Perovskite	612 mAh/g	50 mA/g	310 mAh/g	70 mAh/g	[264]
$\text{Fe}_3\text{SnC@CNF}$ Antiperovskite	1060 mAh/g	1 A/g	604 mAh/g	1000 mAh/g	[4]
$\text{Li}_{0.5}\text{La}_{0.5}\text{TiO}_3$ Perovskite	449 mAh/g	2 A/g	229 mAh/g	3000 mAh/g	[265]
Cs_4PbBr_6 Perovskite	377 mAh/g	45 mA/g	94 mAh/g	100 mAh/g	[266]
Cs_2CuBr_4 Perovskite	800 mAh/g	20 mA/g	420 mAh/g	– mAh/g	[267]
$\text{Nd}_{0.9}\text{Mn}_{0.1}\text{FeO}_3$ Perovskite	2550 mAh/g	100 mA/g	2400 mAh/g	50 mAh/g	[268]
SmFeO_3 Perovskite	450 mAh/g	5 mA/g	300 mAh/g	20 mAh/g	[269]
$\text{Co}_3\text{ZnC@CNF}$ Antiperovskite	1100 mAh/g	2 A/g	800 mAh/g	1500 mAh/g	[229]
SrSnO_3 Perovskite	714 mAh/g	50 mA/g	260 mAh/g	50 mAh/g	[270]
CaSnO_3 Perovskite	457 mAh/g	60 mA/g	380 mAh/g	45 mAh/g	[271]

3.5 Conclusions

Designing a new high capacitive antiperovskite material for alkali ions battery is an open problem. Here we report very first time a new strategies to boost the reversible capacity via surface modification of an antiperovskite that delivers better performance as compared to the pure antiperovskite material (Co₃CuN). 3D nitride antiperovskite Co₃CuN as an anode material provides a reversible capacity of ~ 408 mAhg⁻¹ at 0.1 A/g current density. After modifying the surface of pure Co₃CuN delivers a very high reversible capacity of ~ 1150 mAh/g at the same current density of 0.1 A/g which is more than twice as compared to the pure material. The full cell with a NMC-532 cathode delivered a high reversible capacity of ~ 500 mAhg⁻¹ with a very good stability 50 cycles with more than 50 capacity retention. Thus Co₃CuN with surface modification showed an excellent Li-storage performance as a new and efficient material that can be improved further. We believe that this work will open up various new possibilities to focus on 3D antiperovskite nitride systems to be explored in the field of energy storage.

Chapter 4

Growth and Properties of Epitaxial Heterostructure of Antiperovskite and Perovskite Using Pulsed Laser Deposition (PLD)

Abstract

Designing and growing the antiperovskite and perovskite heterostructure and exploring the corresponding interface properties is an interesting but challenging task due to their complex structural surface phase(s) and dissimilar chemical character. Herein, we report the growth of epitaxial heterostructure interface of magnetic intermetallic antiperovskite nitride Co_3CuN (CCN) on the non-magnetic insulating metal oxide single crystal substrate of LaAlO_3 (LAO) by using the physical thin film deposition technique of Pulsed Laser deposition or PLD. PLD is a well-known method of film growth in the field of oxide epitaxy because of its natural strength of true stoichiometry transfer from a single sintered target to the film. Its applicability to the growth of an intermetallic like CCN entails an optimization effort.

4.1 Introduction

Interfaces and interface systems are ubiquitous in nature and are a cornerstone of most advanced device systems. A significant amount of fundamental science that has emanated during the past few decades revolves under the peculiarities of the novel interface phenomena. The interface-driven devices are in regular use in a number of device concepts such as mobile phones, laptops, smartwatches, flexible devices, solar cells, LEDs, batteries, sensor devices, etc. Understanding the physics and chemistry of interface systems in heterostructures of interesting materials partners is therefore scientifically interesting and technologically important. All the physical and chemical interactions (Van der Waals and Coulomb) play a major role in defining the properties of heterostructures. All these opportunities afforded by the exciting properties and phenomena of interface systems motivated us to design a new heterostructure interface by using two different types of crystal systems namely the standard perovskite and the relatively less explored antiperovskite.

Heterostructure interfaces between two different materials represent, in most cases, a discontinuity of structural and chemical properties and by implication lead to the emergence of exciting new physical phenomena. Indeed, interfaces have played a huge role in all the emerging phenomena and technological applications in recent times. In particular, complex oxide-based heterostructures have already shown their utility of applicability in different fields of science and technology [272–274] Achieving the desired heterostructure functionalities [275] at the interface is quite challenging due to the presence of different factors like geometrical and chemical strains, compatibility, adaptability [272–274], etc.

As stated earlier in the introduction, the antiperovskite materials mostly behave as intermetallic compounds because the positions of cations and anions are interchanged vis a vis the standard perovskite structure (space group $Pm\bar{3}m$, no. 221) [27]. Many intriguing properties have been encountered in antiperovskite materials like their perovskite counterparts such as topological electronic behavior, magneto volume effect, itinerant antiferromagnetism, superconductivity, giant magnetoresistance, etc [43, 73, 85, 87, 104, 276–278]. Due to the presence of the strong spin-lattice coupling in most nitride antiperovskite materials, (X_3NA ; X: TM; A: semiconducting or metallic elements) these have attracted great attention due to their active engagement with the external perturbations like temperature, pressure, and magnetic field [42, 73, 278–283]

With different crystal facet-related chemical and geometrical effects, it is possible to tune the physical properties of the antiperovskite materials (e.g. nitride one in the present case, X_3NA) after the successful realization of the epitaxial thin film along with different crystallographic directions. In particular, the growth of epitaxial thin film of

nitride antiperovskite (X_3NA) on the single crystal oxide perovskite substrates of the form ABO_3 could be of great interest in tuning and extracting novel physical properties for multifunctional device applications. Therefore, herein we set out to design and grow a heterointerface between the antiperovskite nitride of Co_3CuN and a perovskite oxide of $LaAlO_3$ along the (001) direction using the physical vapor deposition technique of pulsed laser deposition (PLD) [42, 279–283] that has already been successful in the metal oxide perovskite domain. We decided to optimize the antiperovskite growth based on the same PLD technique so that this work could be further extended to multilayer growth using the two types of targets in situ in the same chamber even without breaking the vacuum.

In order to explore the antiperovskite/perovskite hetero-interface, it is first necessary to understand the different structures of the facets such as (001), (110), and (111) of both the perovskite oxide (ABO_3) and antiperovskite nitride (X_3NA) to evaluate whether the heterostructure is technically feasible along one or all of these directions. As shown in Figure 4.1, in the unit cell of X_3NA antiperovskite and that of ABO_3 perovskite the positions of cation and anion are reversed [42, 275].

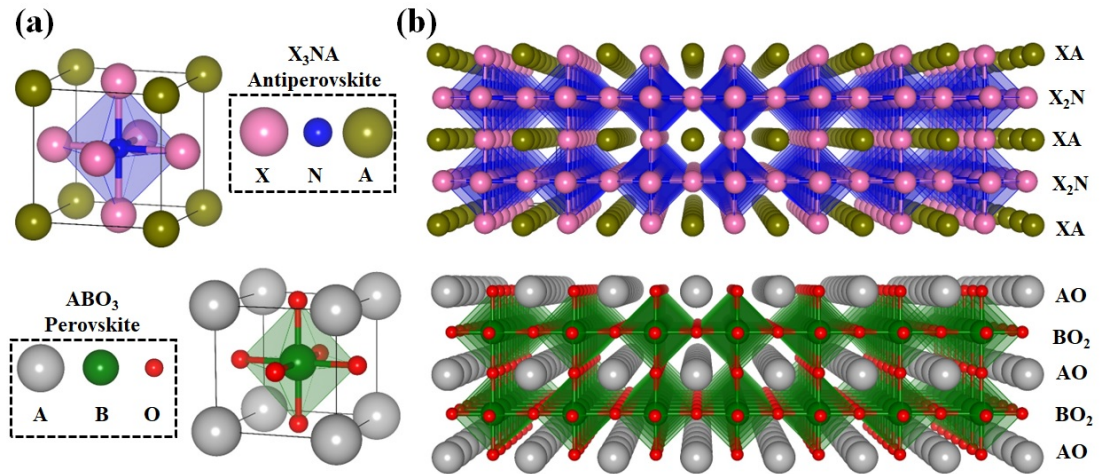


FIGURE 4.1: (a) Bulk and (b) surface structure of corresponding antiperovskite and perovskite.

To understand the surface chemistry at the interface of nitride antiperovskite and oxide perovskite it is necessary to know all possible surface terminations along (001) as shown in Figure 4.1(b). The fundamental differences between their anion and cation positions separate them from the perovskite-perovskite and antiperovskite-antiperovskite interfaces and help us to design a functional interface between the X_3NA and ABO_3 materials with novel properties that cannot be attained in the interfaces between two perovskites or two antiperovskites.

In the unit cell of normal perovskite structure ABO_3 , we see two possible surface terminations AO and BO_2 , and these cation-anion layers arrange alternatively along the

(001) direction. Similarly, for nitride antiperovskite of X_3NA , we can see the XA and X_2N alternating layers along the (001) direction (Figure 4.1(b)). It is noted that when the interface is formed between two oxide perovskite of ABO_3 and $A_1B_1O_3$ then only two interface configurations are possible, namely A_1O/BO_2 and B_1O_2/AO respectively [275]. Using the same analogy, for the two antiperovskites of X_3NA and X'_3NA' only two stable interface configurations are possible, namely $X'A/X_2N$ and X'_2N/XA . However, till now the experimental realization of the latter is not achieved, because as of now all the antiperovskite are polycrystalline [4] and no single-crystal antiperovskite is observed [275].

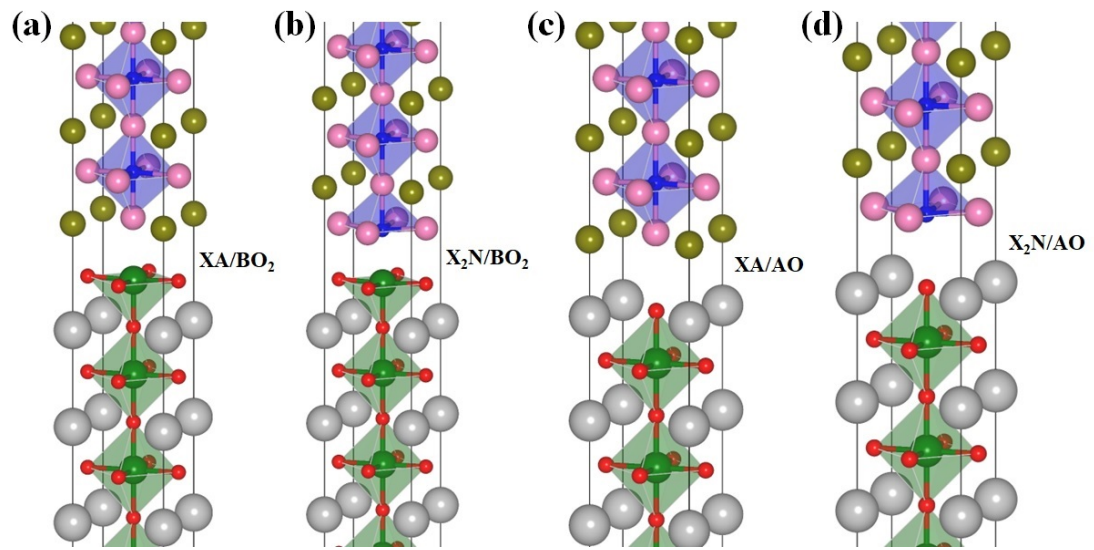


FIGURE 4.2: Four possible hetero-interface between antiperovskite and perovskite: (a) XA/BO_2 (b) X_2N/BO_2 (c) XA/AO (d) X_2N/AO .

Figure 4.2(a-d) illustrates that a total of four heterostructure interface systems are possible between X_3NA antiperovskite and ABO_3 perovskite material and these are XA/AO , X_2N/AO , XA/BO_2 , and X_2N/BO_2 , respectively. Now the beauty of these four different interfaces becomes clear when the chemical bonding between them comes into the picture. In most of the oxide perovskite, an ionic bond is present whereas in an antiperovskite metallic and covalent bonds are observed. So hybridization will occur between them at the interface and this will facilitate different functionalities which could lead to the field of device and technological applications which is not easily achievable in conventional oxide/oxide interface. It can also open up a new path for developing novel behavior associated with peculiar interface-borne phenomena [272–274].

In our study, we have chosen Co_3CuN , a nitride antiperovskite material, which is a 3D intermetallic and highly conducting ferromagnetic material [284] whereas $LaAlO_3$ is a single crystal highly insulating non-magnetic material with a bandgap of 6.3 eV [285, 286]. From the above properties of these two materials, it could be inferred that the

corresponding interface can have interesting attributes of the metal-insulator character as well as the magnetic-nonmagnetic intermediate character.

Structural details of the nitride antiperovskite Co_3CuN : 4.3 illustrates the bulk and the surface (001) structure of the CCN. In the bulk structure of CCN, the Cu atom is located at the corner, the Co atom is located at the face center, and the N atom is located at the body center with an atomic ratio of 3:1:1. The surface along the (001) direction of CCN is shown in Figure 4.3 (a) and (b), with two possible terminations as CuCo and Co_2N , respectively.

Structural details of the oxide perovskite LaAlO_3 : The bulk and surface structures of the single crystal oxide perovskite of LaAlO_3 (LAO) are presented in Figure 4.4. In the bulk, the O atom is located at the face center, the La atom is located at the corner, and the Al atom is located at the body center. These differences highlight the electronic character inversion between perovskite and antiperovskite. Along the (001) direction, AlO_2 and LaO terminations are present, as shown in Figure 4.4(a-b). It is reported that AlO_2 termination is more favorable as compared to the LaO termination due to the higher surface energy of AlO_2 ($2.41 \text{ eV}/\text{\AA}^2$) as compared to LaO ($0.14 \text{ eV}/\text{\AA}^2$) [287–289].

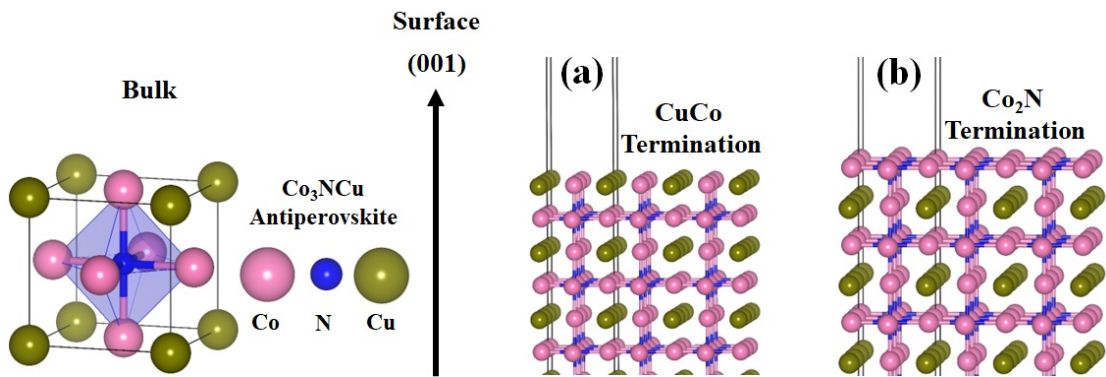


FIGURE 4.3: Bulk and surface (001) structure of Co_3CuN (a-d).

The construction of epitaxial thin film depends on the crystal lattice parameter of the substrate (LaAlO_3) and the film (Co_3CuN). The lattice mismatch between the film and substrate creates compressive and tensile strain in the system and this strain plays a tremendous role in the emerging functionalities of the interface material. Herein, we have chosen LaAlO_3 , a cubic nonconducting single crystal oxide perovskite of lattice constant 3.78\AA as a substrate and the corresponding lattice constant of the film Co_3CuN is 3.75\AA , which is conducting ferromagnetic material, both the lattice constants being compatible for the growth of the epitaxial thin film. The synthesis protocol for the Co_3CuN antiperovskite compound and its physical deposition by PLD are discussed below.

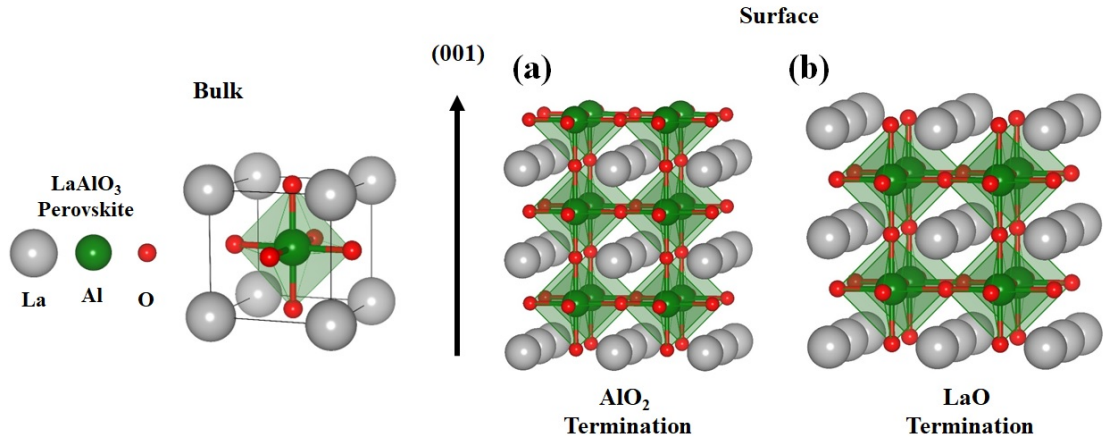


FIGURE 4.4: Bulk and surface (001) structure of LaAlO₃ (a-b).

4.2 Experimental Sections

4.2.1 Synthesis of Target Material Co₃CuN (CCN)

The hydrothermal method was used to synthesize the antiperovskite nitride Co₃CuN. In a typical synthesis, 1.5 mmol cobalt acetate, 0.5 mmol copper acetate, and 4 mmol HMT were dissolved in 50 mL deionized water and mixed it properly. The mixture was then transferred into a 100 mL Teflon-lined autoclave and then heated at 120°C for 12 h. After cooling down to room temperature, the precipitate was collected through centrifugation (1000 rpm for 15 minutes) and washed with deionized water and ethanol 3 to 4 times. The collected product was dried in a vacuum oven at 80°C overnight. The dried product was then ground well and calcined at 420°C for 4 h under NH₃ atmosphere in a tube furnace. After cooling down to room temperature, the furnace atmosphere was replaced with N₂ flow. The final product was collected for further characterization. To obtain a large amount (several grams) of CCN to make a PLD target we synthesized this material in many cycles and we were able to get a pure phase of CCN every single time. This signifies the reproducibility of the process and the high stoichiometric quality of the target material. After that, we made a pallet of 13 mm (millimeter) diameter by applying 8-ton pressure.

4.2.2 Structural Characterization of Target Material Co₃CuN (CCN)

The XRD pattern of the target material is presented in Figure 4.5(a) and the sharp peak in the PXRD patterns reveals the pure and single-phase character of the Co₃CuN. All the peak positions and corresponding planes are indicated in Figure 4.5(a) which are well-matched with the earlier reported [126] PXRD pattern. To understand the morphology

of the sample we recorded SEM images which are presented in Figure 4.5(b) which suggest that Co_3CuN has both types of morphologies present, particle-like, and rod-like. This morphology was further clarified by HRTEM images presented in Figure 4.5(c). The FFT image implies the (111) planes with a lattice spacing of 0.22\AA (Figure 4.5d) and we obtain experimental lattice parameter 3.75\AA using the Bragg's law ($2d\sin\theta = n\lambda$) which matches well with the reported lattice parameter 3.74\AA (Figure 4.5(d)). The elemental mapping of bulk CCN is presented in Figure 4.6(b) which implies the uniformity of the material and Figure 4.6(a) represents the EDX of the pure phase CCN which tells the exact stoichiometry of the material.

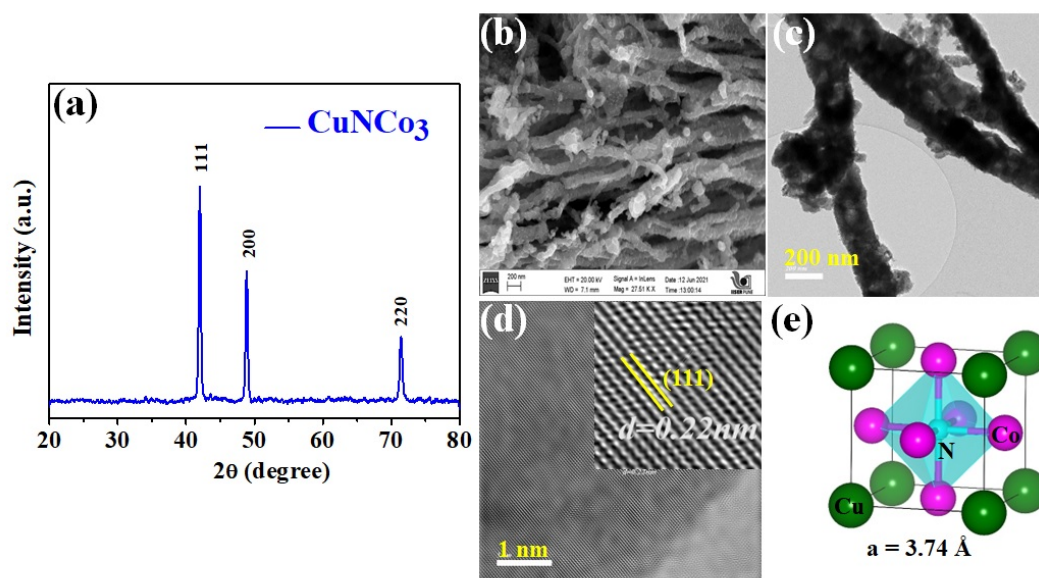


FIGURE 4.5: (a) XRD of Co_3CuN (b) SEM image (c-d) HRTEM image (e) Optimized Co_3CuN .

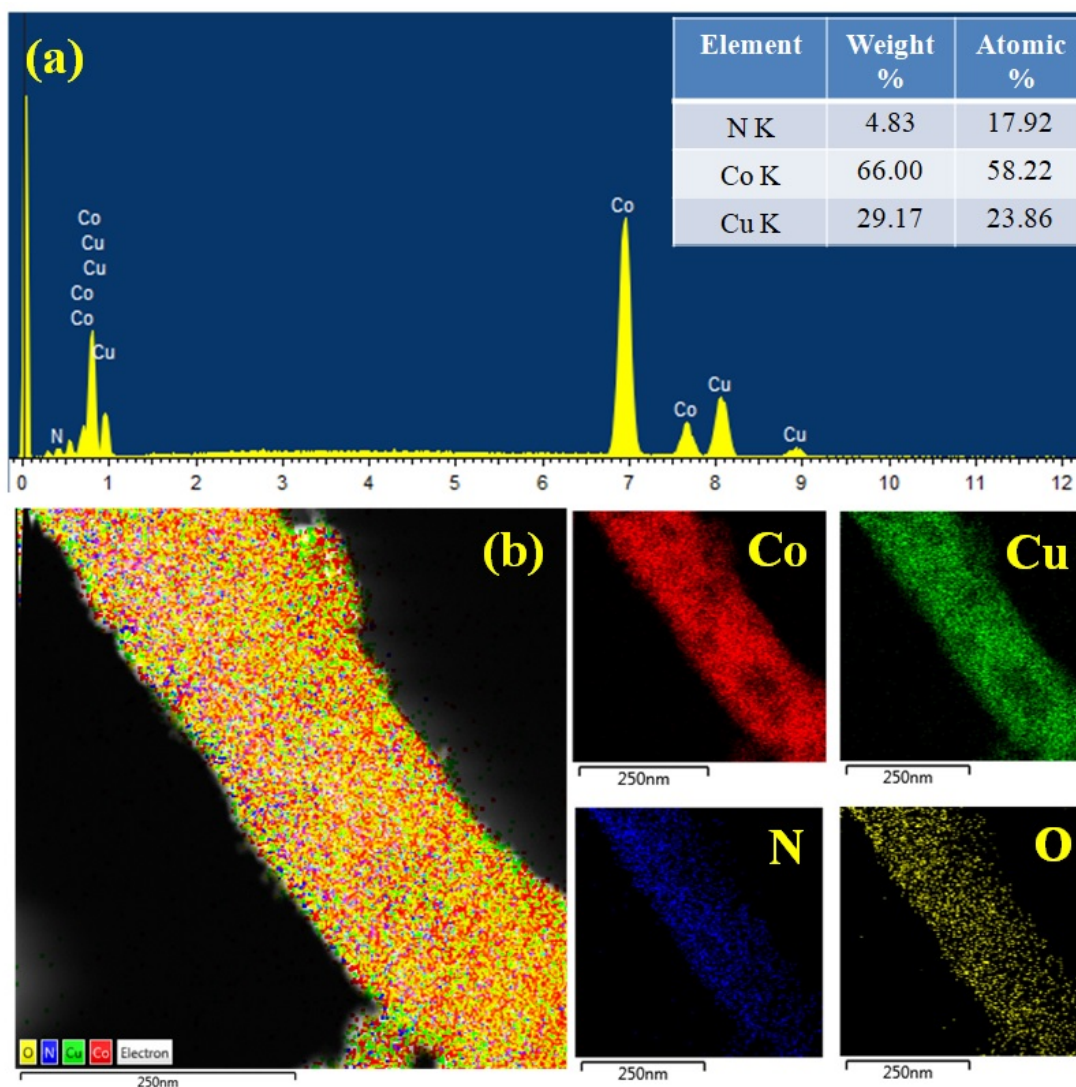


FIGURE 4.6: (a) EDAX analysis; (b) Elemental mapping of Co_3CuN .

4.2.3 Fabrication of Co₃CuN thin Film Using PLD

The Co₃CuN (CCN) thin films were grown on the surface of LaAlO₃ (LAO) along (001) direction by using the pulse excimer laser deposition (PLD) technique: the UV laser parameters being (KrF laser, wavelength $\lambda = 248$ nm). We deposited the films in an N₂ atmosphere and the corresponding growth condition for the deposition of the nitride antiperovskite (CCN) film on LAO (001) were: growth temperature 500°C, laser energy density 3.5 J/cm², pulse repetition rate 5Hz, and the nitrogen pressure of 100 mTorr. The distance between the substrate and target was 40 mm. After growth, the system was cooled to room temperature in the presence of the same N₂ pressure.

After growth the system was cooled till room temperature in the presence of same N₂ pressure.

Pulsed Laser Deposition (PLD) Process

Many methods are there to grow the epitaxial thin film in the laboratory such as pulsed laser deposition (PLD), Molecular beam epitaxy (MBE), Chemical solution deposition (CSD), etc. In the thin-film community, all the above processes have equal importance. First Dijkkamp et al. [290] synthesized epitaxial thin film in 1986 using pulsed laser deposition (PLD) technique since then PLD become more popular in thin-film material society. After that, most of the oxide thin film deposition PLD technique has commonly been used [291–294]. The figure 4.7 illustrates the schematic representation of the PLD process. In the thin film deposition process, the thin film material which is known as the target material is made by laboratory process or collected from the commercial market. The target material is then processed through heat treatment and made in different sizes of pallets, 25 mm, 13 mm, etc. Thin film is deposited in a high vacuum PLD chamber (10⁻⁷ MBR). The target material mounts through a rotating holder and ablates the target material with a laser pulse of a certain wavelength (KrF laser of wavelength $\lambda = 248$ nm). During ablation by laser on the target material, it produces a highly energetic beam which is called plumed and this plumed is a mixture of ions, atoms, and molecules deposited on the surface of the substrate which placed at a distance 40 to 50 mm from the target material. The substrate mounted on the substrate holder which connected with a heater. Depending on the material property like oxide, nitride, and others the PLD chamber is filled with gas like O₂ N₂, Argon, NH₃, etc with required deposition pressure by control way. The plumed interact with the substrate material with many different growth conditions like gas pressure, temperature, laser energy, laser spot, etc. By tuning these growth conditions one could able to grow high-quality thin film using PLD.

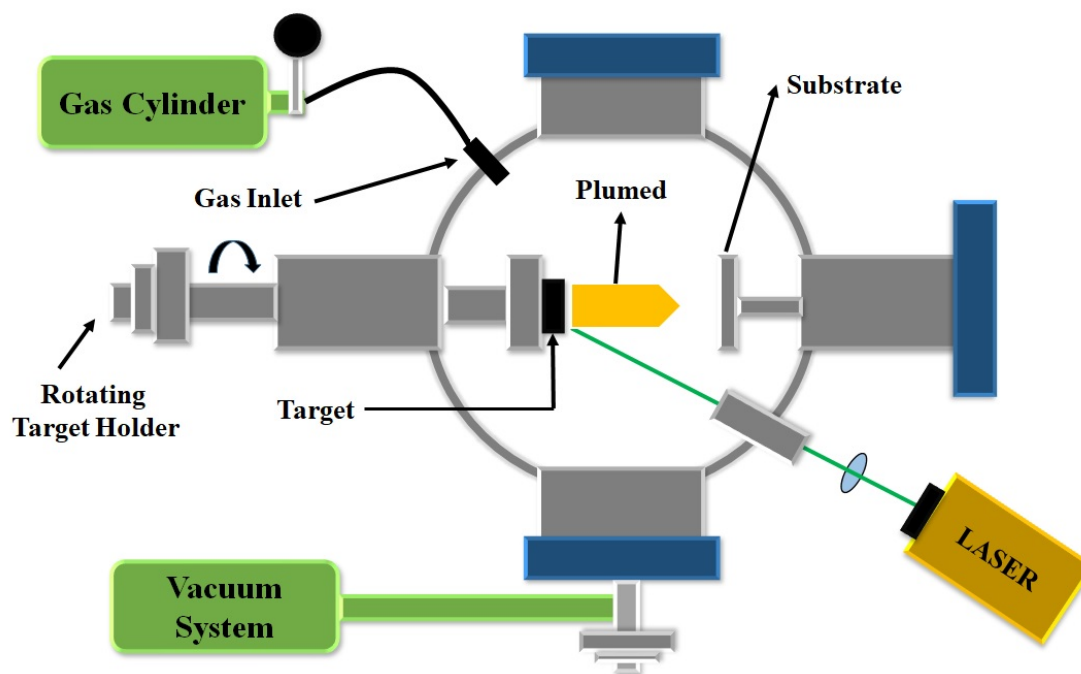


FIGURE 4.7: Schematic of PLD processes

4.2.4 Structural Characterization of Co_3CuN thin film

To understand the growth of the film phase and its quality we recorded the x-ray diffraction (XRD) data of the film presented in Figure 4.8(a). It signifies that film is grown along the (001) direction (with 001 and 002 signatures) mimicking the LAO substrate, at the 2θ positions of 23.94° and 48.91° closer to the shoulder peaks of the LAO substrate at 23.73° and 48.62° (Figure 4.8(b-c)). The positions of the CCN thin-film peak(s) on the LAO substrate match well with earlier reported XRD data by Zhenzhen et al. where they deposited the film through the chemical vapor deposition technique [284]. It is for the first time, that we can grow the CCN film on the single crystal substrate LAO through a physical deposition technique using PLD, which is important for its easy functional integration with other metal oxide systems which can be grown very well by PLD. The SEM and EDX images presented in Figures 4.9(a, c) show that the film stoichiometry is properly maintained (3:1:1) (Figure 4.9(c)) and the AFM image shows the smoothness and uniformity of the film (Figure 4.9(b)). We have grown ~ 40 nm thin film on LAO substrate shown in Figure 4.10 and the thickness measured by cross-sectional SEM imaging method.

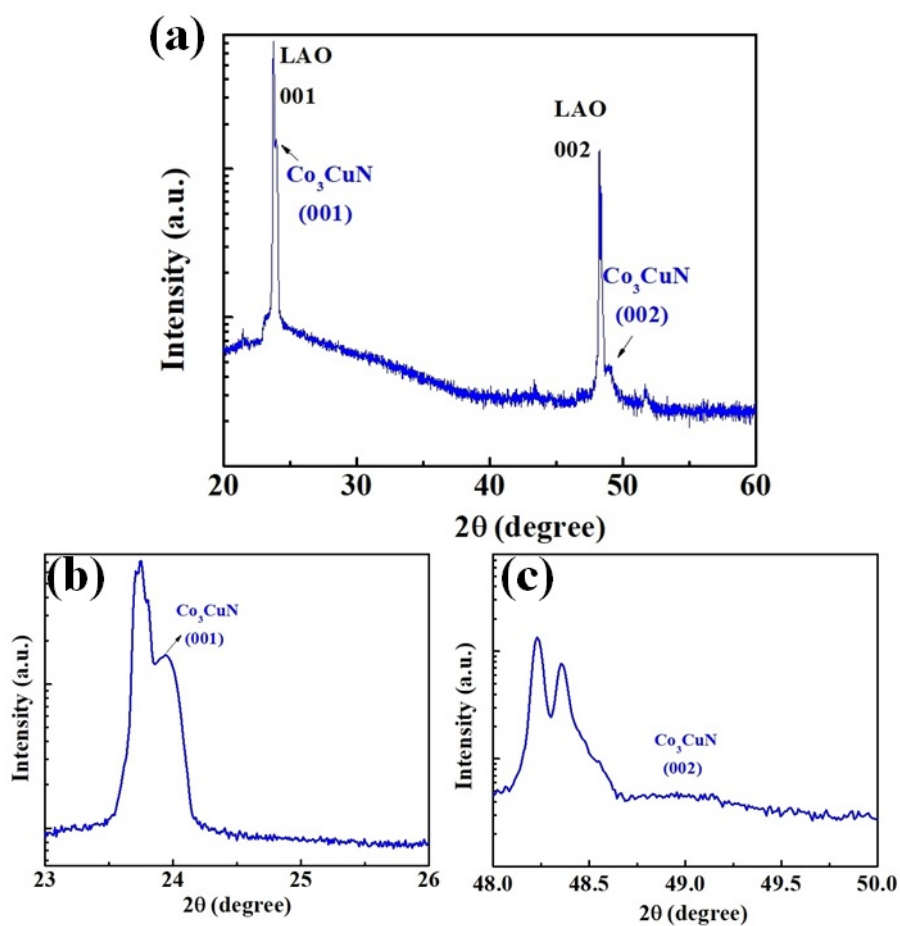


FIGURE 4.8: (a-c) Thin film XRD of Co_3CuN .

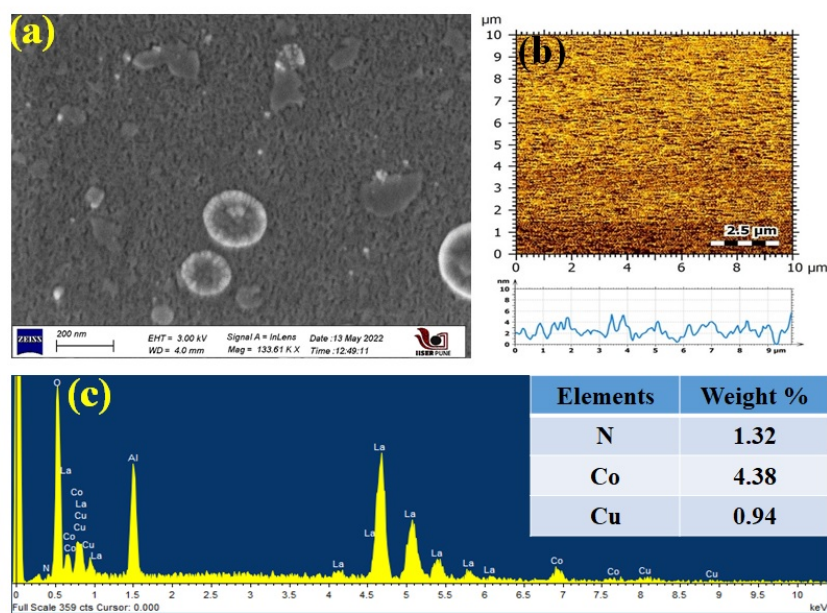


FIGURE 4.9: SEM EDX and AFM image of the thin film of Co_3CuN .

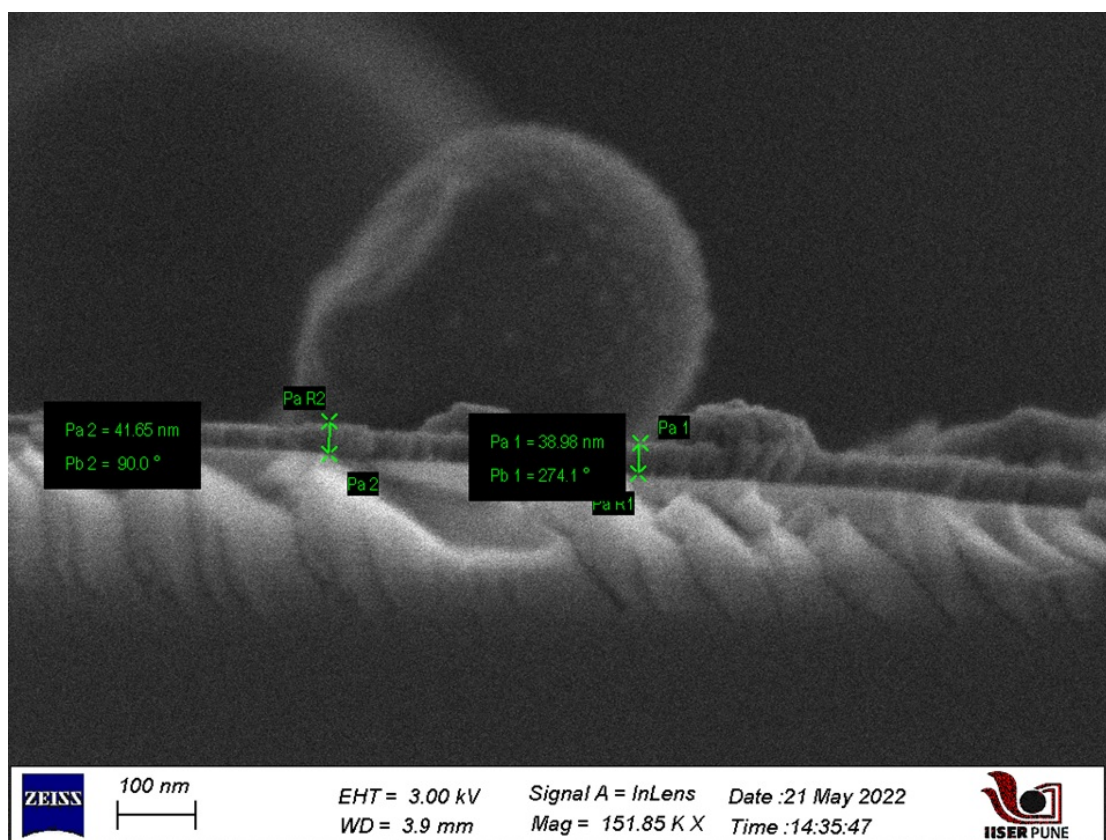


FIGURE 4.10: Thickness of CCN film ~ 40 nm.

4.3 Results and Discussion

Figure 4.8(a) illustrates that no extra phases are observed suggesting the purity of the phase. Both CCN (001) and CCN (002) diffraction peaks are observed along with the substrate peak. The CCN(002) diffraction peak is weak which could be attributed to the effect of the structure (strain) or atomic scattering factor [49, 54, 154, 295–297]. It has also been verified that Mn, Fe, and Co-based thin film of antiperovskite also shows weak peak intensity [298–300].

4.3.1 XRD analysis of the CCN thin film

The relative strain arises in the epitaxial heterostructure thin film, which depends on the corresponding lattice constants of the substrate and the film. The relative strain can be calculated using the formula given below [301].

$$\epsilon = \frac{a_s - a_f}{a_f} \quad (4.1)$$

Where ϵ denotes the strain of the system a_s (LAO) and a_f (CCN) denotes the substrate and film lattice constants respectively. Generally, two types of strain are observed in epitaxial heterostructure thin film and these being tensile and compressive strain[301]. The +Ve and -Ve values of ϵ the decide the tensile and compressive nature of the system and all these strains could be realized by noting the right or left shift of the XRD peak position [301].

Herein, for the nitride antiperovskite (CCN) and oxide perovskite (LAO) epitaxial heterostructure (CCN/LAO) thin-film the relative strain is +1.1 % (considering the experimental lattice constant of the substrate a_{LAO} is 3.79Å and a_{CCN} is 3.75Å) which is a tensile strain as the substrate lattice constant is larger than the film lattice constant ($a_{LAO} \geq a_{CCN}$). This in-plane tensile strain compresses the c-axis and reducing the corresponding d-value. This causes a right shift of the peaks (increasing 2θ). Figure 4.11 indeed illustrates the right shift of the XRD peak of the CCN/LAO epitaxial thin film. The XRD peak position of the 001 planes of pure LAO substrate is at 23.73° which gets right-shifted at 23.94° after the film is formed suggesting the tensile strain generated in the system. This happens purely due to the in-plane (Figure 4.2) strong interaction between the atoms at the interface [301, 302]. The presence of dangling bonds at the top of the surface of both the substrate and film always try to minimize their charge neutrality and these phenomena assists to produce an interaction between the atoms which create strain and introduce new physics and chemistry with different bond lengths and

bond angles at the interface. These leads to exciting emergent functional properties in the system[301].

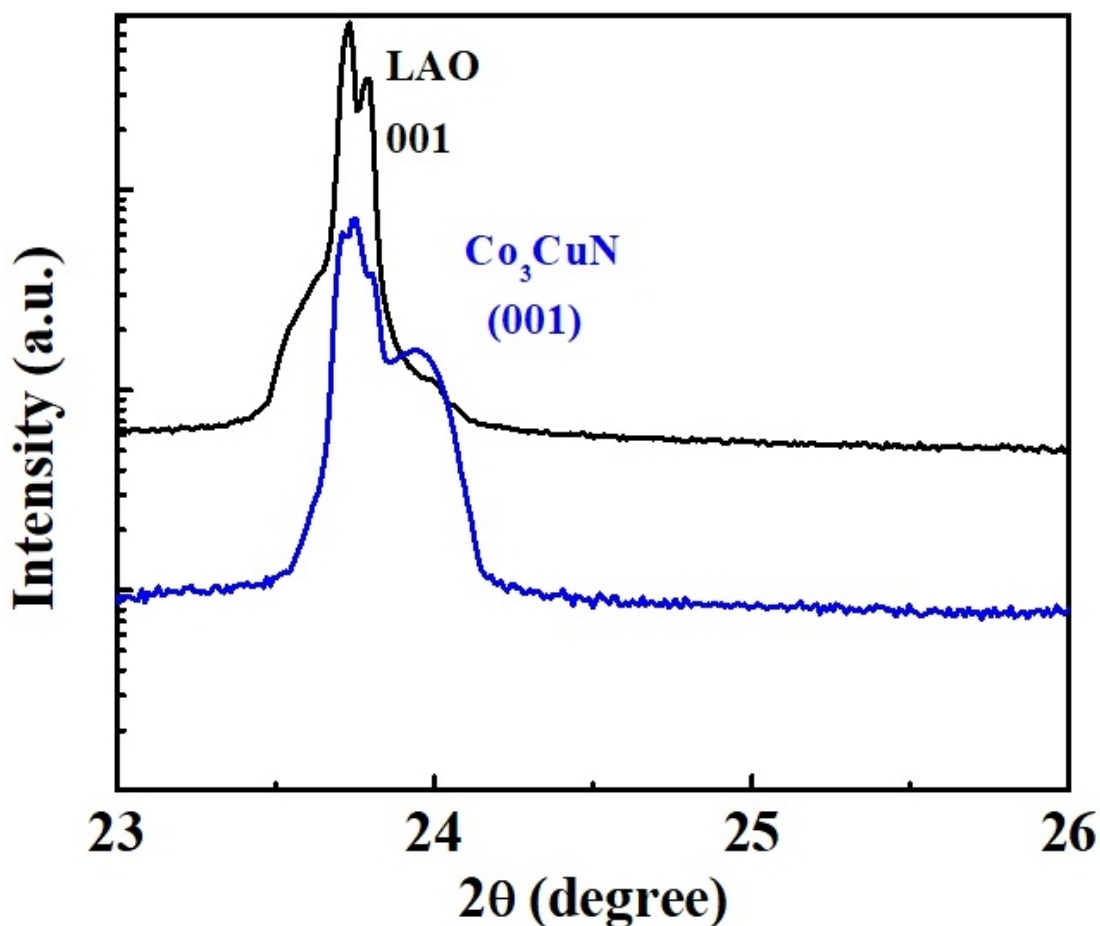


FIGURE 4.11: Shifting of XRD peak of CCN film on LAO substrate.

4.3.2 Raman Spectroscopy Analysis of the CCN thin film

The Raman spectrum of the bulk Co_3CuN (CCN), pure substrate LAO and the epitaxial film CCN/LAO were recorded to understand the presence of different vibrational modes and relative strain in the system. The figure 4.12 illustrates the corresponding Raman spectra of all three systems. For CCN we observed the vibrational modes of Co-N bonds at 470 cm^{-1} (E_g), 517 cm^{-1} (F_{2g}) and 674 cm^{-1} (A_{1g}). Till now, CCN has no scientific report based on the Raman spectrum but the structure of CCN could be correlated with Co_4N material for which similar Raman modes are present [303]. At lower frequency we observed vibrational mode for Cu-Co at 188 cm^{-1} [304]. Since all the modes of CCN attributed the crystallinity similar to Co_4N [303, 305].

We separately plotted the Raman spectrum for LAO substrate (Figure 4.12 block curve) as a reference and all the corresponding vibrational frequency modes of LAO (001)

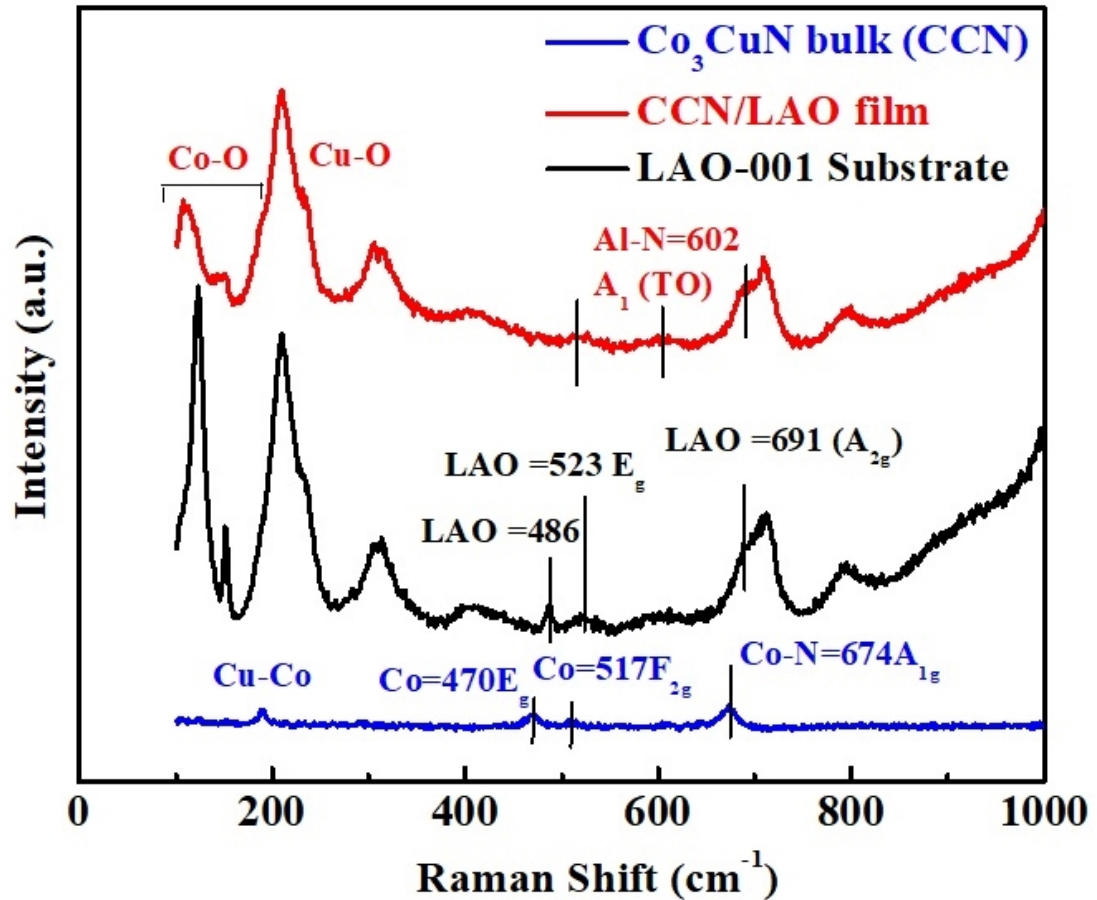


FIGURE 4.12: The Raman spectrum of Bulk CCN, LAO substrate and CCN film

substrate seen at 480 cm^{-1} , 523 cm^{-1} (E_g) and 691 cm^{-1} (A_{2g}) matches well with the earlier reported Raman spectrum [306].

It has been observed that the thin film Raman spectra of CCN (Figure 4.12 red curve) shifted as compared to the bulk CCN. The major peaks seem to be dominated by the LAO substrate as expected, but a mismatch is present between the Raman spectrum of film and substrate at lower and higher frequencies. Figure 4.13 presents the mismatch between the film and substrate which is attributed to the presence of strain in the system. At lower frequencies of the film, the vibrational modes correspond to metal-oxide bonds as shown in Figure 4.12, suggesting the presence of Co-O and Cu-O bond vibrations [307, 308]. At 602 cm^{-1} (A_1 -TO) Al-N vibrational mode is present with a small intensity. [309, 310]. All the Raman spectra signify the bond formation between atoms at the interface of nitride antiperovskite and perovskite.

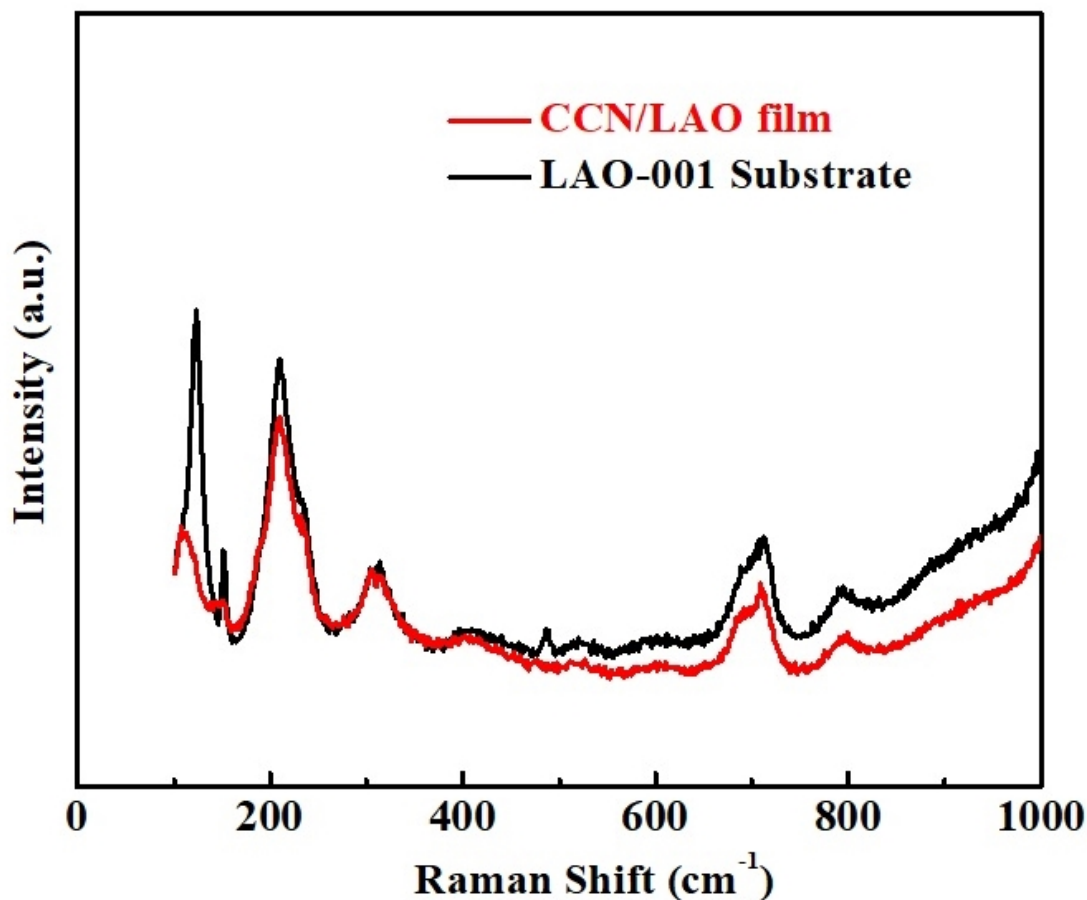


FIGURE 4.13: The Raman spectrum overlap of LAO substrate and CCN film

4.3.3 XPS Analysis of the bulk and thin film of CCN

The XPS spectra of Co 2p, Cu 2p, and N 1s are presented in the Figure ?? The binding energy (B.E.) of Co 780.0 eV-781.5 eV (Figure ?? a) corresponds to the Co-N suggesting the hybridization between the Co 3d and N 2p orbitals due to the atomic position of Co (face center) and N (body center) in the unit cell of Co_3CuN [49, 284, 303, 311]. The B.E. of 932.4 eV in Figure 4.14(b) signifies the Cu-N bonding which implies the hybridization between the Cu 3d and N 2p orbitals as discussed earlier in the $\text{Mn}_{3.6}\text{Cu}_{0.4}\text{N}$ system [312, 313]. The N 1s spectra (Figure ?? c) shows a peak at 398.5 signifies the hybridized between Co (Cu) 3d with N 2p which could be attributed to the diverse covalency of the system [284]. Another peak at B. E. of 398 eV is attributed because of the residual surface contaminants which harmonize with the published work by Hui et al. [284, 314]. We also recorded the XPS spectra of the bulk CCN target and the corresponding data are presented in Figure 4.15. It can be seen that all the XPS spectra match well with thin-film spectra suggesting the pure and stoichiometric phase formation in the CCN thin film.

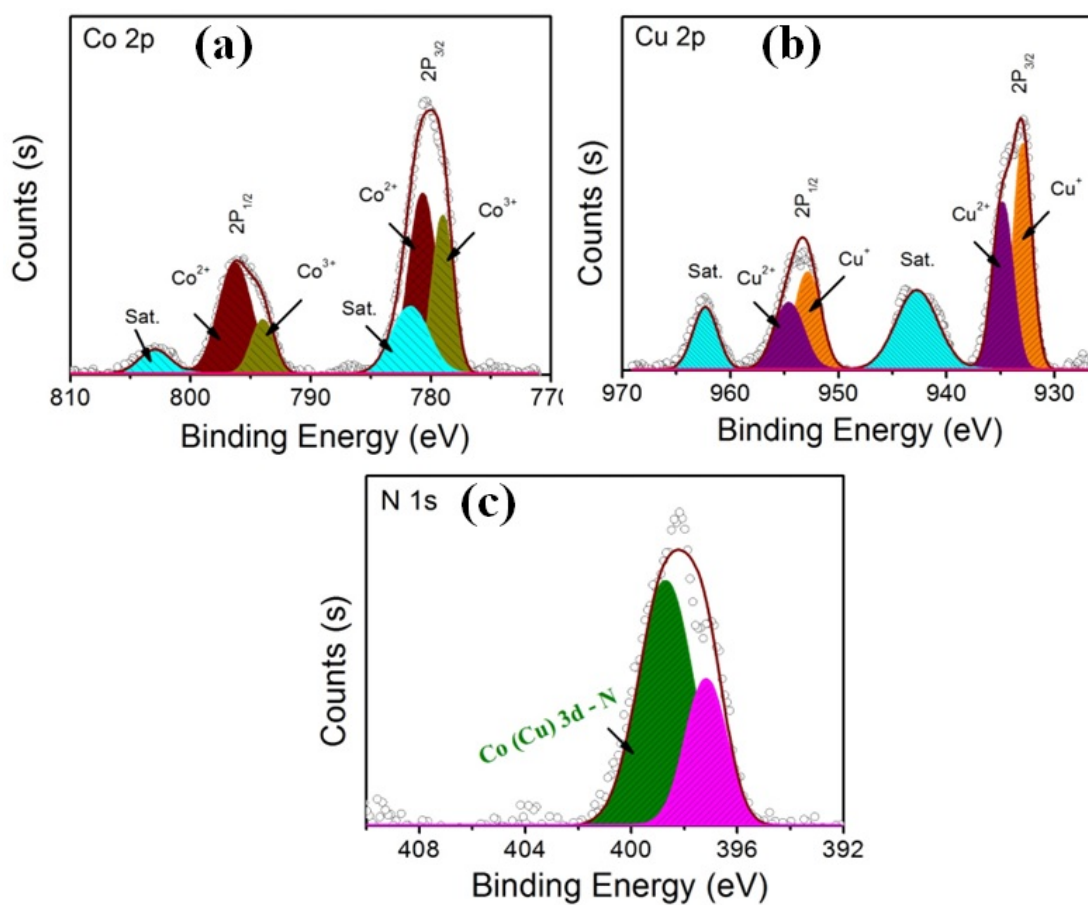


FIGURE 4.14: XPS spectra of the CCN thin film (a) Co 2p , (b) Cu 2p and (c) N 1s.

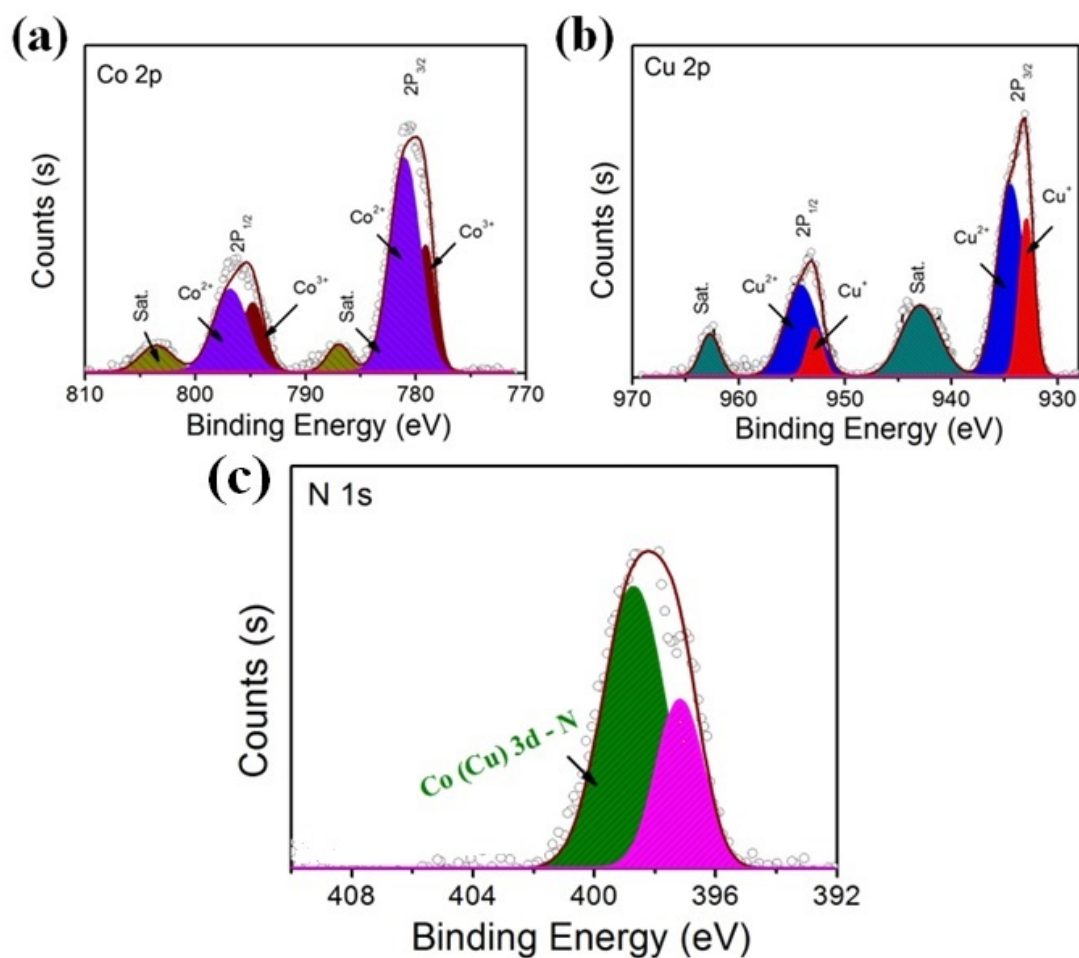


FIGURE 4.15: XPS spectra of the bulk CCN (a) Co 2p , (b) Cu 2p and (c) N 1s.

4.3.4 Resistance vs Temperature (RT) Plot

We have performed temperature-dependent resistance measurement using four-probe inside a close cycle refrigerator (CCR) (Current source: Keithley 6221 AC and DC). The figure 4.16 illustrates the R vs T plot of the CCN film on the LAO (001) substrate and it shows excellent conducting nature. At low temperature of 10K and room temperature (300K) the resistance of the CCN film is 68.6 ohm and 134 ohms respectively. From the theoretical study by Hui et al. [49, 284] it is observed that the presence of the finite number of states at the Fermi level (E_F) in the density of states (DOS) where Co 3d orbital contributes more and the hybridization (see Figure 4.14 b and c) between the (Cu) Co 3d and N 2p orbitals play important role in the conducting nature of the film.

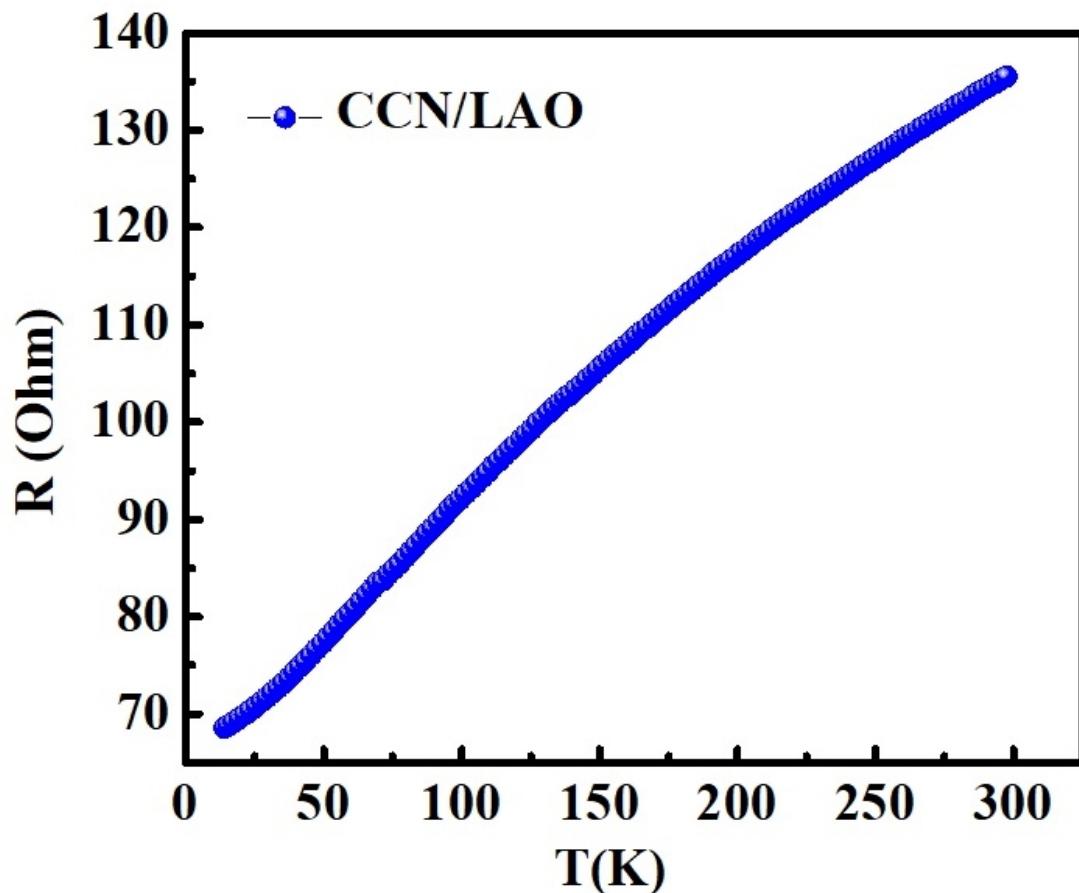


FIGURE 4.16: Resistance vs Temperature or RT plot.

All the experimental characterization of the CCN film on the LAO substrate provide the information about its phase formation and its stability. Quintela et al.[275] predicted that X_2N/BO_2 (see Figure 4.2b) interface is energetically more favored where they have discussed the result based on $Mn_3GaN/LaAlO_3$ system which is very much similar to our system $Co_3CuN/LaAlO_3$. They have proposed that due to the similarities between the Wyckoff position of anion and cation of antiperovskite and perovskite the coulombic

and Van der Waals interaction between the atom at the interface plays a significant role to stabilize the system (Figure 4.2(a-d)). Multiple bond-building at the interface of nitride antiperovskite and oxide perovskite could trigger many properties and exciting functionalities such as large magnetoresistance, Nernst effect, spin transfer, and Hall effect spintronics devices, etc [315–319]. We are seeking the experimental realization and application of the above properties and many other properties with this new class of epitaxial heterointerface material between two chemically inverted structures of oxide perovskite and nitride antiperovskite.

4.4 Conclusions

Designing a single crystal antiperovskite material film is an extremely important task for exploring real high-tech applications of this interesting intermetallic material. In our study, we have attempted to grow the epitaxial heterostructure interface between the nitride antiperovskite (Co_3CuN) and oxide perovskite (LaAlO_3) with a physical deposition technique of PLD. The presence of electronic elemental inversion of these two materials at the interface could allow the tuning and control of their properties and could help in multiple applications. The conducting nature of the film shows its electronic transport characteristic. We believe that with successful growth of epitaxial thin film of this CCN antiperovskite on the single crystal oxide perovskite LAO could open new and exciting avenues for future material design.

Summary and Future Outlook

Thesis Summary

In the thesis, my whole study focused on "Antiperovskite" based material, especially carbide and nitride antiperovskite. Antiperovskite is a twin brother of perovskite material because of the electronic inversion of the atomic positions. It is well a fact that Perovskite dominates in every domain of science and technology over the last 20 to 30 years. The chemical and structural flexibility of the perovskite help to rule the material world. Now the time come for antiperovskite to rule the world but it's challenging. In our study, we have shown the different applications of carbide and nitride antiperovskite. In carbide antiperovskite, we have discussed how electrochemical lithiation can control the magnetic spin polarization in the system. In nitride antiperovskite, we are the first to design high-capacity anode material for Li-ion batteries by constructing the core-shell of the nitride material. Our next work is also based on nitride antiperovskite material here we have discussed the growth and properties of epitaxial heterostructure thin film of nitride antiperovskite on perovskite using pulsed laser deposition (PLD) technique. The outcome of my study about antiperovskite material discusses below.

My first study on the 3D carbide antiperovskite material and it is combined theoretical and experimental study, we introduce the concept of iono-spintronics or Spintronic Battery wherein the accumulation and de-accumulation of Li-ion in the antiperovskite Fe_3SnC anode of a Li-ion half-cell concurrently and reversibly stores charge and spin; the latter mimicked by the experimental observation of non-monotonic changes in magnetization as a result of degree of lithiation, nominally depicted as $(\text{Li}_{x=1-4}\text{Fe}_3\text{SnC})$. It is noted experimentally that lithiation leads to a biphasic system in this particular case because of the affinity of Sn to form an alloy with Li. Thus with progressive lithiation changes occur in the stoichiometries and properties of the two phases, namely the Sn-Li alloy phase and lithiated or partially lithiated Fe_3C phase. The computer (DFT) calculations have been performed accordingly to account for these changes.

Given the structural and strain-related changes in magnetization upon lithiation and its degree, and their connection to spin polarization outlined here, we believe that this study would have broader and more interesting implications for a variety of structurally interesting materials systems, not limited only to the anti-perovskite intermetallic case discussed herein, wherein the structure-magnetism-spin polarization connection is acute.

Also, the biphasic character encountered here may not occur in other systems wherein selective preferred interaction, as that of Sn in the present case, is not a possibility. With the rapid evolution of the fields such as the internet of things (IoT) a new breed of low-power consuming spintronics devices with novel functionalities is desired. Towards this end, effects such as concurrent storage of spins mediated by traditional battery architecture described here could add an interesting dimension.

In the next study we have designing a new high capacitive antiperovskite material for alkali ions battery which is an open problem. Here we report very first time a new strategies to boost the reversible capacity via surface modification of an antiperovskite that delivers better performance as compared to the pure antiperovskite material (Co_3CuN). 3D nitride antiperovskite Co_3CuN as an anode material provides a reversible capacity of $\sim 408 \text{ mAhg}^{-1}$ at 0.1 A/g current density. After modifying the surface of pure Co_3CuN delivers a very high reversible capacity of $\sim 1150 \text{ mAh/g}$ at the same current density of 0.1 A/g which is more than twice as compared to the pure material. The full cell with a NMC-532 cathode delivered a high reversible capacity of $\sim 500 \text{ mAhg}^{-1}$ with a very good stability 50 cycles with more than 50 capacity retention. Thus Co_3CuN with surface modification showed an excellent Li-storage performance as a new and efficient material that can be improved further. We believe that this work will open up various new possibilities to focus on 3D antiperovskite nitride systems to be explored in the field of energy storage.

In the last chapter we have designing a single crystal antiperovskite material film is an extremely important task for exploring real high-tech applications of this interesting intermetallic material. In our study, we have attempted to grow the epitaxial heterostructure interface between the nitride antiperovskite (Co_3CuN) and oxide perovskite (LaAlO_3) with a physical deposition technique of PLD. The presence of electronic elemental inversion of these two materials at the interface could allow the tuning and control of their properties and could help in multiple applications. The conducting nature of the film shows its electronic transport characteristic. We believe that with successful growth of epitaxial thin film of this CCN antiperovskite on the single crystal oxide perovskite LAO could open new and exciting avenues for future material design.

Future Outlook

The structural beauty of the antiperovskite attracts great attention in the research community. Working on antiperovskite material motivates us to further work on different types of antiperovskite material like oxide antiperovskite, halide antiperovskite, etc. Here we want to discuss a few future works on antiperovskite material.

1. The electronic inversion of antiperovskite material could help to design a highly efficient catalyst for water splitting, CO₂ reduction, etc.
2. Tuning the high concentration element present at the face center and corner of the unit cell of antiperovskite could help to design multi-functional material for future applications.
3. Designing oxide antiperovskite and oxide perovskite epitaxial interface by PLD.
4. Study of magnetic spin polarization through electrochemical lithiation in commercial cathode and anode material for Li-ion batteries.

Appendix A

Experimental and Battery Details

In this chapter, we have discussed about experimental and computational methodologies employed in this thesis. First we have discussed about the experimental details and its outline. Then we have showed the theoretical derivation of the Schrödinger equation and Born-Oppenheimer approximation.

A.1 Experimental Details

In material science, synthesis is the most important step in solid-state chemistry research. The samples may be prepared as a polycrystalline powder, single crystal, or thin film. Glass and amorphous are from another class of materials. In this chapter, we will discuss only the methods of synthesis of polycrystalline materials. The X-ray single crystal method is generally used to discover and design new materials. Polycrystalline material passes some difficulty in the determination of crystal structure. However, powder XRD is excellent for polycrystalline materials. There are several methods to synthesize the different crystal materials such as solid-state, hydrothermal, flux method, etc. Each method is controlled by several controllable and/or uncontrollable parameters. The parameter influences the obtaining of phase, morphology, and size of the crystal. Here, in my thesis, I will discuss solid-state and hydrothermal synthesis. The experimental and theoretical (DFT) method was used in my thesis which will be discussed in the following sections. Where we will discuss the material synthesis methods and different characterization techniques such as XRD, SEM, TEM, XPS, SQUID, PLD, etc. The theoretical DFT calculations that have been performed to support the experimental results will be discussed in very brief in the following sections.

A.1.1 Synthesis Methods

There are various synthesis methods to synthesize the powder or polycrystalline sample. Here in my thesis we discussed about two synthesis methods which are Hydrothermal and vacuum sealed quartz tube methods and the details of these two methods has discussed below.

A.1.1.1 Solid-state Method

The solid-state synthesis method is the simplest. The number of syntheses controlling the parameters is small, but it is challenging to manage. This method is commonly used to synthesize single crystals and polycrystalline powders of metals and monovalent cations [1]. Thermal effects play an essential role in crystallization during phase change, and it is carried out in two stages: germination and growth. Germination begins at a point where the phases remain unbalanced, a condition that can be favored by various factors, such as crucible wall, impurity, and shapelessness. This step consists of "germs" in the reaction mixture. Growth occurs in several stages: atom reorganization, absorption on solid surfaces, dispersion, and final settling of particles. Continuous layers, therefore, converge on the face of the crystal, which sees its volume increase. [320, 321]

The solid-state synthesis can be done into two steps:

Preliminary treatment: The desired amount of precursor is weighed and then crushed in an agate mortar in this step. The resulting powder is placed in a crucible or a porcelain basket and preheated between 350 and 400°C for a few hours. This operation allows the decomposition of the primary reagents and removes volatile products such as NH₃, NO₂, CO₂, and H₂O, leaving only oxides. The mixture is then placed in the ground at the outlet of the oven so that it becomes more uniform and the grain size is smaller [321].

Crystal growth: After the germination phase, and under the influence of the concentration gradient, the cations are transferred to the germ, creating an orderly layer. This transfer is favorable by heating to a very high temperature. After cooling, the crystals are separated from the current by hot and sometimes boiling water.[320, 321]

The disadvantage of this method is that it is prolonged and requires a lot of energy. The reaction occurs at high temperatures (500–2000°C) for several hours and at the same time for several days. Heating at this temperature can cause the desired compound to decompose. Experimentally, oxides and nitrates are harmful reagents in synthesizing single crystals, and they often give small-sized crystals that are insufficient for X-ray



FIGURE A.1: Equipment used in solid-state synthesis

single-crystal scattering. Mechanical grinding can reduce grain size and increase the specific surface, increasing the reaction. The cooling rate is crucial for obtaining a single crystal with good crystals. The cooling rate should be as slow as possible, and the crystallization temperature should be below 50°C [320, 321].

A.1.1.2 Hydrothermal and Sealed Glass Tube Method

Hydrothermal is an efficient chemical synthesis method used to synthesize single crystals, polycrystalline substances, and nanoparticles of different sizes. Synthesis occurs inside a closed autoclave with pressure and temperature. The hydrothermal method usually occurs in water at temperatures between 180 and 300°C . The furnace can be an autoclave (Fig. 2) or a sealed glass tube (Fig. 3). Several materials have been synthesized using the hydrothermal method [320, 321].

The hydrothermal conditions of the aqueous medium correspond to temperatures and pressures above 100°C and 1 bar, respectively. These conditions allow changing the chemistry of the cation in a sufficient amount of solution. They favor the formation of complex metastable structures of low symmetry and involve more minor changes in enthalpy and entropy than in the "normal" state. Hydrothermal conditions are also among the geological processes during which many minerals were formed. In the laboratory, such a situation is achieved by heating a solution in a closed enclosure (autoclave and sealed glass tube) at 200 - 400°C .

The thermodynamic properties of water up to temperatures of 1000°C and pressures of several tens of kilobars are well known. Quantitative data are collected in numerous review articles. There are three essential points to remember[320, 321].

As the temperature increases, the water dielectric constant decreases. It is increased by increasing the pressure. Therefore, hydrothermal solutions are characterized by low dielectric constants and electrolytes that are entirely isolated under normal conditions that preferably form pairs of ions or complexes with a common electrostatic charge[320, 321].



FIGURE A.2: Autoclave

As the temperature rises, the viscosity of the water decreases, which leads to more mobility of the dissolved species than average.



FIGURE A.3: Sealed glass tube

The ionic product of water increases strongly with temperature. Conductivity measurement allows establishing the law of change of ionic product as a function of temperature.

Herein, my thesis work has focused on carbide and nitride antiperovskite materials. For carbide Antiperovskite sealed glass tube method was used, the detailed synthesis procedure discusses in chapter 3. On the other hand, for nitride antiperovskite we have followed the hydrothermal synthesis method as this method helps to stabilize the unusual oxidation state as this state is observed in all antiperovskite materials, in chapter 4 we have discussed the synthesis protocol nitride antiperovskite.

Different experimental methods were used for different antiperovskite materials. For carbide polycrystalline materials solid states synthesis approach was used. On the other hand, nitride antiperovskite nanoparticles were synthesized using a hydrothermal process. Several solid-state synthesis methods for synthesizing polycrystalline materials and nanoparticle materials will be discussed in the following sections.

After synthesized all the materials we have put them for battery performance testing (as anode or cathode) using battery tester before that we need make the electrode and assembled the cell which is discussed below.

A.2 Fabrication of the Battery Coin Cell

The demand for rechargeable alkali ion batteries especially Li-ion batteries dominating the worldwide commercial market. Day by day the usage and demand of high energy density and long-life cycle batteries increases. From very small devices to very large devices huge power sources are required in modern-day technology. To understand the basic construction of any commercialized battery we first need to understand the lab-scale construction of the battery such as constructions of a coin cell, pouch cell, cylindrical cell, etc. In this following section, we will discuss the basic construction protocol of a coin cell battery.

A.2.1 Protocol of Working Electrode Preparation

Many steps are involve for the battery electrode preparation. Here we will discussed the steps required for the prepeation of Li-ion battery electrode.

- Prepare a mixture of PVDF and NMP with the required proportion
- Weighing the active material, C black, the binder with desire ratio best on availability of the active materials.
- Mix the above weighing sample properly with NMP for 30 min to make a good slurry.
- Make slurry coating uniformly on a metal foil (Copper for anode and aluminum of cathode).
- Dry the coating in air or vacuum at 80 to 100oC overnight inside an oven.
- Hot press the coated metal foil between to steel plate.
- Punch the dried coated metal foil into discs of 8 mm in diameter and weigh these discs.

A.2.2 Assembly of coin cell

- Keep electrolyte inside glovebox as LiPF_6 is photosensitive.
- Punch the lithium foil as a counter electrode of the same diameter as coated metal foil electrode and keep it inside an argon glove box.
- Assemble the separator (celgard), coin cell cases, spring, and spacers into the glovebox.

- Place the working electrode after adding two drops of electrolyte into the cell cup. Place the separators and add another three drops of electrolyte. Add two more drops of electrolyte before adding a lithium counter electrode to it. After that place two stainless steel spacers and a spring on the lithium disc.
- Close the cell using the cell cap and crimp using the compact crimping machine.
- The cell is ready for testing and can be taken out of the glovebox.

A.2.3 Testing of the Coin Cell

- Measure the open-circuit voltage (OCV) using a multi meter.
- Define the voltage window for testing the cell based on the active material used in the working electrode.
- Calculate the theoretical capacity for the cell using the calculation shown below.

Weight of the electrode disc with the current collector = W_{ED}

Weight of the uncoated current collector disc of the same diameter = W_{CC}

Weight of the active electrode material $W_{EM} = W_{ED} - W_{CC}$

Weight of the active material in the electrode $W_{AM} = W_{EM} \times 0.8$ (80% active material)

The theoretical capacity of the electrode disc $C_{ED} = W_{AM} \times C$

Where C is the theoretical specific capacity of the active material which is defined as; $C = \frac{n \times F}{M.W \times 3.6}$; Where n is the number of Li-ions that material can take, F = Faraday's constant = 96500 Cmol⁻¹, M.W = Molecular weight of the electrode material gmol⁻¹.

- Test the coin cell with different C-rate during the charge-discharge cycle.

A.3 Electrochemical Energy Storage

A.3.1 Battery

A battery is a device that stores chemical energy, which is converted into electrical energy during the discharge process[322]. The main components of the battery are shown in the figureA.4. Unlike supercapacitors, batteries are entirely a Faraday device. Charge storage takes place throughout the electrodes through oxidation and reduction. This implies that batteries form bulk storage despite surface storage. Batteries have a specific electrochemical potential where the Faraday reaction occurs through the transfer of electrons. EDLCs exhibit capacitive behavior consistent with the absorption of ions on the surface of the electrode, and time scales are in seconds. Pseudo-capacitors undergo a Faraday reaction with interpolation, reflected in their charge-discharge. The battery charging-discharging time scale varies from minutes to hours. The batteries have a high power concentration and a specific potential window that can be tuned based on the selected electrolyte. Battery power density can be increased by using high rate power materials. There is also a wide range of battery operating possibilities. Aqueous electrolyte-based batteries run up to 1.23 V because water splitting is thermally possible outside of this. Using a non-aqueous battery, the potential window can be extended up to 4V.

In this work, the electrochemical energy storage devices are the primary focus and hence will be described more elaborately. The primary components of an electrochemical energy storage device are:

Cathode: The positive electrode which undergoes reduction during the discharge process.

Anode: The negative electrode which undergoes oxidation during the discharge reaction.

Separator: A material that prevents cathode and anode to be in direct contact with each other hence preventing the short circuiting of the half cells.

Electrolyte: A medium which facilitates ion flow from one direction to another. Based on the type of device it can be aqueous, alkaline or organic.

The major electrochemical energy storage and conversion devices are capacitors, supercapacitors, batteries and fuel cells.

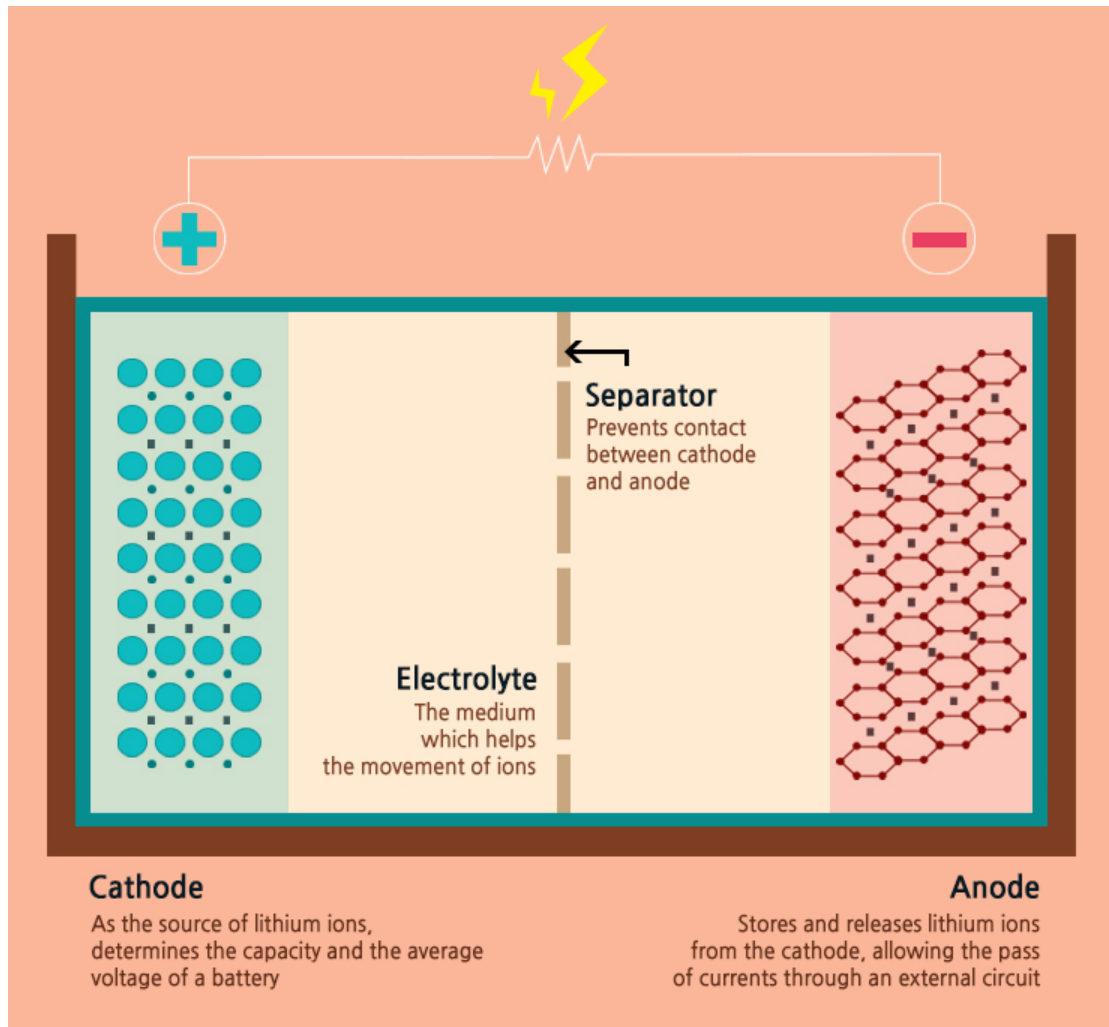


FIGURE A.4: Battery Components (From internet)

A.3.2 Capacitor

The conventional capacitors compose of two conducting plates separated by a dielectric medium (ϵ) with finite distance (d). This is called as the parallel plate configuration of capacitors. The capacitance C is calculated by the following equation:

$$\text{Capacitance } C = \epsilon \times \frac{A}{d}$$

The A is the area of the plates and d is the distance between them. ϵ is the permittivity of the dielectric. The unit of the capacitance is Farad (F) and the typical capacitors for general applications have the capacitance in the range of picofarad (pF) to millifarads (mF). The capacitor stores the potential energy between the plates in terms of electric energy. The process is non-Faradaic in nature. The capacitors have very high-power density but very low energy density.

A.3.3 Supercapacitor

A supercapacitor differs from a capacitor in terms of the amount of energy it can store. Supercapacitors are known as ultracapacitors since they have high energy density and capacity as compared to conventional capacitors [323, 324]. A supercapacitor employs porous carbon material as electrodes and stores charge electrostatically. The supercapacitors have high power density as the charge storage/release happens at very high rates. The supercapacitors are employed in the applications where instant power is required. They are further classified into two types depending upon the charge storage process, 1) Electrochemical Double Layer Capacitors (EDLCs) and 2) Pseudo capacitors.

Electrochemical Double Layer Capacitors (EDLCs): The EDLCs store charge in the electrical double layer created at the electrode/electrolyte interface hence the name EDLC [325]. These are highly stable and robust as no chemical reaction is involved in charge storage. The energy storage in the electrical double layer capacitor (EDLC) takes place by the charge separation at the interface between the electrolyte and electrode. The electrolyte is usually aqueous solution of salts like H_2SO_4 or KOH . The charging and discharging processes in the EDLC ideally involve no electron transfer across the electrical double layer at the electrode/electrolyte interface. Thus they are non-Faradaic in nature. EDLCs have remarkably long cycle life because of electrostatic charge storage and absence of chemical reaction.

Pseudo capacitors: The pseudo capacitors are similar to EDLC except that they involve redox process along with double layer for the charge storage [326]. Sometimes intercalation also takes place in pseudo capacitors [322, 327]. In pseudo capacitors, surface confined redox reactions (Faradaic reactions) occur in the material. The electron transfer in a pseudo-capacitive material brings a net charge into the material. This is neutralized through the intercalation of ions of the opposite charge from the electrolyte into the electrode. This is the reason why they are compared to batteries. However, the difficulties for ion transport and substantial solid phase changes in pseudo capacitors makes them inferior to the EDLCs in terms of power density.

A.3.4 Types of Batteries

Batteries are classified broadly on the basis of their function and life cycle. The two categories into which batteries are divided majorly are 1) primary batteries and 2) secondary batteries.

A.3.4.1 Primary Batteries

These batteries have a fixed life span and can't be recharged once their cycle life is finished. They stop functioning once the chemicals are used up and the components need to be replaced for further generation of electricity.

A.3.4.2 Secondary Batteries

Also popularly called as rechargeable batteries now, these batteries have a longer life span and can be recharged over multiple cycles. The chemical processes taking place in such batteries are reversible. There are various types of batteries have been used earlier but due to their short comings many batteries had developed and these batteries are: Baghdad Battery (250 B.C.), Voltaic Pile (1749), Daniel cell (1836), Lead Acid Battery (1859), Leclanché Cell (1866), Zinc-carbon Cell (1886), Nickel-Cadmium (Ni-Cd) Battery (1899), Na-Sulphur Battery (1967) and Nickel-metal hydride Battery (1970). Finally, we arrived with a new battery technology of Li ion battery in short it is called as LIB.

Lithium (Li) ion Batteries: The Li ion battery era started in 1980 with the contribution of American scientist John B. Goodenough when he proposed a Li containing oxide LiCoO_2 (LCO) as a cathode material. Same year, Rachid Yazami from Morocco discovered graphite anode with solid electrolyte [15, 16]. The first Li ion battery prototype was built by Japan in 1985 and the Li ion battery commercialization was done by Sony in 1991. Li ion batteries have electromotive force up to 3.6 V and are now commercially used for large scale as well as small scale applications. Li polymer batteries were also developed using a polymer or gel-based electrolyte to mitigate the issues associated with the use of liquid electrolytes which are generally carbonates based and are flammable, posing a threat to the safety of the device.

Since the non-aqueous rechargeable batteries are into the business, many other battery chemistries are into the research. To increase the energy and power density of the current Li ion battery technology, other technologies such as Li-Sulphur, Li-air batteries, Li metal batteries, Li- CO_2 batteries, Zn-air batteries, Redox-flow batteries are being the topic of research and development[328]. These batteries are at the early stage of development and it will take some time for them to come at par with Li ion battery systems [329, 330]

As the Li reserves are known to be reserved in the earth's crust, alternatives are being hunted. Among them, Sodium (Na) ion batteries have already gained the attention and are commercial [331, 332]. Along with these, Magnesium (Mg), Potassium (K) and

Calcium (Ca) ion batteries are also being explored [193, 333, 334]. Nonetheless, being heavier than Li, Na and other ion batteries would never be closer to Li ion batteries in terms of energy and power density. Nevertheless, in large scale applications where weight is not a concern, Na ion batteries have already flourished as a possible replacement to Li ion batteries [335].

Bibliography

- [1] Hongxia Zhong, Chunbao Feng, Hai Wang, Dan Han, Guodong Yu, Wenqi Xiong, Yunhai Li, Mao Yang, Gang Tang, and Shengjun Yuan. Structure–composition–property relationships in antiperovskite nitrides: Guiding a rational alloy design. *ACS Applied Materials & Interfaces*, 13(41):48516–48524, 2021.
- [2] James Dawson, Theodosios Famprakis, and Karen E Johnston. Anti-perovskites for solid-state batteries: recent developments, current challenges and future prospects. *Journal of Materials Chemistry A*, 2021.
- [3] Zhi Deng, Dixing Ni, Diancheng Chen, Ying Bian, Shuai Li, Zhaoxiang Wang, and Yusheng Zhao. Anti-perovskite materials for energy storage batteries. *InfoMat*, 4(2):e12252, 2022.
- [4] Kingshuk Roy, Vinila Chavan, Sk Mujaffar Hossain, Sattwick Haldar, Ramanathan Vaidhyanathan, Prasenjit Ghosh, and Satishchandra B Ogale. Fe₃snC@cnf: A 3 d antiperovskite intermetallic carbide system as a new robust high-capacity lithium-ion battery anode. *ChemSusChem*, 13(1):196–204, 2020.
- [5] AN Ogude and JD Bradley. Ionic conduction and electrical neutrality in operating electrochemical cells: Pre-college and college student interpretations. *Journal of chemical education*, 71(1):29, 1994.
- [6] Bora Timurkutluk, Cigdem Timurkutluk, Mahmut D Mat, and Yuksel Kaplan. Anode-supported solid oxide fuel cells with ion conductor infiltration. *International journal of energy research*, 35(12):1048–1055, 2011.
- [7] Kathryn R Bullock. Lead/acid batteries. *Journal of power sources*, 51(1-2):1–17, 1994.
- [8] Richard S Treptow. The lead-acid battery: Its voltage in theory and in practice. *Journal of chemical education*, 79(3):334, 2002.
- [9] Anthony Green. The characteristics of the nickel-cadmium battery for energy storage. *Power engineering journal*, 13(3):117–121, 1999.

- [10] Majharul Haque Khan, ASW Kurny, et al. Characterization of spent household zinc-carbon dry cell batteries in the process of recovery of value metals. *Journal of Minerals and Materials Characterization and Engineering*, 11(06):641, 2012.
- [11] Francois Putois. Market for nickel-cadmium batteries. *Journal of Power Sources*, 57(1-2):67–70, 1995.
- [12] Kwo-Hsiung Young. Research in nickel/metal hydride batteries 2017, 2018.
- [13] Michael A Zelinsky, John M Koch, and Kwo-Hsiung Young. Performance comparison of rechargeable batteries for stationary applications (ni/mh vs. ni-cd and vrla). *Batteries*, 4(1):1, 2017.
- [14] John M Koch, Kwo-Hsiung Young, Jean Nei, Chaolan Hu, and Benjamin Reichman. Performance superlattice metal comparison hydride between alloys in ab sealed 5 and cells. *Nickel Metal Hydride Batteries 2017*, page 298, 2018.
- [15] Christophe Pillot. The rechargeable battery market and main trends 2015-2025. In *Avicenne Energy, Presentation at 18th International Meeting on Lithium Batteries, Chicago (USA)*, 2016.
- [16] Christophe Pillot. The rechargeable battery market and main trends 2014–2025. In *31st International Battery Seminar & Exhibit*, pages 5–7, 2015.
- [17] William EW Roediger, Alison Duncan, Olympia Kapaniris, and Sue Millard. Reducing sulfur compounds of the colon impair colonocyte nutrition: implications for ulcerative colitis. *Gastroenterology*, 104(3):802–809, 1993.
- [18] Naoki Nitta, Feixiang Wu, Jung Tae Lee, and Gleb Yushin. Li-ion battery materials: present and future. *Materials today*, 18(5):252–264, 2015.
- [19] MH Rossouw and MM Thackeray. Lithium manganese oxides from li₂mno₃ for rechargeable lithium battery applications. *Materials research bulletin*, 26(6):463–473, 1991.
- [20] Dipanwita Majumdar, Manas Mandal, and Swapan Kumar Bhattacharya. Journey from supercapacitors to supercapatteries: recent advancements in electrochemical energy storage systems. *Emergent Materials*, 3(3):347–367, 2020.
- [21] Alternative Fuels Data Center. Us department of energy. *Natural Gas Vehicle Emissions*, 2013.
- [22] Jingru Zhang, Dongliang Bai, Zhiwen Jin, Hui Bian, Kang Wang, Jie Sun, Qian Wang, and Shengzhong Liu. 3d–2d–0d interface profiling for record efficiency all-inorganic cspbri₂ perovskite solar cells with superior stability. *Advanced energy materials*, 8(15):1703246, 2018.

- [23] Eun-Bi Kim, M Shaheer Akhtar, Hyung-Shik Shin, Sadia Ameen, and Mohammad Khaja Nazeeruddin. A review on two-dimensional (2d) and 2d-3d multidimensional perovskite solar cells: Perovskites structures, stability, and photovoltaic performances. *Journal of Photochemistry and Photobiology C: Photochemistry Reviews*, 48:100405, 2021.
- [24] Ehsan Elahi, Ghulam Dastgeer, Abdul Subhan Siddiqui, Supriya A Patil, Muhammad Waqas Iqbal, and Pradeep Raj Sharma. A review on two-dimensional (2d) perovskite material-based solar cells to enhance the power conversion efficiency. *Dalton Transactions*, 2022.
- [25] Richard Weihrich, Korbinian Köhler, Florian Pielhofer, and Sebastian Haumann. From 3d intermetallic antiperovskites to 2d half antiperovskites. *Encyclopedia of Inorganic and Bioinorganic Chemistry*, pages 1–36, 2011.
- [26] Alexandra Morscher, Matthew S Dyer, Benjamin B Duff, Guopeng Han, Jacinthe Gamon, Luke M Daniels, Yun Dang, T Wesley Surta, Craig M Robertson, Frédéric Blanc, et al. $\text{Li}_6\text{SiO}_4\text{Cl}_2$: a hexagonal argyrodite based on antiperovskite layer stacking. *Chemistry of Materials*, 33(6):2206–2217, 2021.
- [27] Sergey V Krivovichev. Minerals with antiperovskite structure: a review. *Zeitschrift für Kristallographie-Crystalline Materials*, 223(1-2):109–113, 2008.
- [28] Xian Zhang, Kai Liu, Jian-Qiao He, Hui Wu, Qing-Zhen Huang, Jian-Hua Lin, Zhong-Yi Lu, and Fu-Qiang Huang. Antiperovskite chalcogenides $\text{Ba}_3(\text{FeS}_4)\text{Cl}$, $\text{Ba}_3(\text{FeS}_4)\text{Br}$ and $\text{Ba}_3(\text{FeSe}_4)\text{Br}$ with spin super-super exchange. *Scientific reports*, 5(1):1–8, 2015.
- [29] Axel Widera and Herbert Schäfer. Das Zustandsdiagramm Sr-Sn und die Verbindung Sr_3SnO . *Journal of the Less Common Metals*, 77(1):29–36, 1981.
- [30] Enamul Haque and M Anwar Hossain. First-principles study of mechanical, thermodynamic, transport and superconducting properties of Sr_3SnO . *Journal of Alloys and Compounds*, 730:279–283, 2018.
- [31] YF Lee, F Wu, R Kumar, F Hunte, J Schwartz, and J Narayan. Epitaxial integration of dilute magnetic semiconductor Sr_3SnO with Si (001). *Applied Physics Letters*, 103(11):112101, 2013.
- [32] Mohamed Oudah, Atsutoshi Ikeda, Jan Niklas Hausmann, Shingo Yonezawa, Toshiyuki Fukumoto, Shingo Kobayashi, Masatoshi Sato, and Yoshiteru Maeno. Superconductivity in the antiperovskite Dirac-metal oxide Sr_3SnO . *Nature communications*, 7(1):1–6, 2016.

- [33] D Samal, H Nakamura, and H Takagi. Molecular beam epitaxy of three-dimensional dirac material sr3pbo. *APL Materials*, 4(7):076101, 2016.
- [34] M Hassan, A Shahid, and Q Mahmood. Structural, electronic, optical and thermoelectric investigations of antiperovskites a3sno (a= ca, sr, ba) using density functional theory. *Solid State Communications*, 270:92–98, 2018.
- [35] Andrew L Goodwin, Simon AT Redfern, Martin T Dove, David A Keen, and Matthew G Tucker. Ferroelectric nanoscale domains and the 905 k phase transition in sr sn o 3: A neutron total-scattering study. *Physical Review B*, 76(17):174114, 2007.
- [36] Leila Ben Amor, Bisma Belgacem, Jean-Sébastien Filhol, Marie-Liesse Doublet, Mouna Ben Yahia, and Rached Ben Hassen. New p-type al-substituted srsno 3 perovskites for tco applications? *Chemical Communications*, 56(17):2566–2569, 2020.
- [37] Daigorou Hirai, Hidetake Tanaka, Daisuke Nishio-Hamane, and Zenji Hiroi. Synthesis of anti-perovskite-type carbides and nitrides from metal oxides and melamine. *RSC advances*, 8(73):42025–42031, 2018.
- [38] David J Singh, Qiang Xu, and Khuong P Ong. Strain effects on the band gap and optical properties of perovskite srsno3 and basno3. *Applied Physics Letters*, 104(1):011910, 2014.
- [39] Yajun Zhang, MPK Sahoo, and Jie Wang. Tuning the band gap and polarization of basno 3/srsno 3 superlattices for photovoltaic applications. *Physical Chemistry Chemical Physics*, 19(10):7032–7039, 2017.
- [40] Qiang Gao, Hengli Chen, Kaifeng Li, and Qinzhuang Liu. Band gap engineering and room-temperature ferromagnetism by oxygen vacancies in srsno3 epitaxial films. *ACS applied materials & interfaces*, 10(32):27503–27509, 2018.
- [41] Yanjun Ma, Anthony Edgeton, Hanjong Paik, Brendan D Faeth, Christopher T Parzyck, Betül Pamuk, Shun-Li Shang, Zi-Kui Liu, Kyle M Shen, Darrell G Schlom, et al. Realization of epitaxial thin films of the topological crystalline insulator sr3sno. *Advanced Materials*, 32(34):2000809, 2020.
- [42] Yonggang Wang, Hao Zhang, Jinlong Zhu, Xujie Lü, Shuai Li, Ruqiang Zou, and Yusheng Zhao. Antiperovskites with exceptional functionalities. *Advanced Materials*, 32(7):1905007, 2020.
- [43] M Bilal, S Jalali-Asadabadi, Rashid Ahmad, and Iftikhar Ahmad. Electronic properties of antiperovskite materials from state-of-the-art density functional theory. *Journal of Chemistry*, 2015, 2015.

- [44] Masatomo Uehara, Akira Uehara, Katsuya Kozawa, Takahiro Yamazaki, and Yoshihide Kimishima. New antiperovskite superconductor $\text{zn}\text{nni}\text{3}$, and related compounds $\text{cd}\text{nni}\text{3}$ and $\text{in}\text{nni}\text{3}$. *Physica C: Superconductivity and its applications*, 470:S688–S690, 2010.
- [45] Hao Cheng, Ai-Jie Mao, Si-Min Yang, Hao Tian, Si-Yu Jin, Miao Yu, and Xiao-Yu Kuang. Semiconductor-to-metal reconstructive phase transition and superconductivity of anti-perovskite $\text{ca}\text{3}\text{pn}$ under hydrostatic pressure. *Journal of Materials Chemistry C*, 8(37):13072–13078, 2020.
- [46] Akira Iyo, Hiroshi Fujihisa, Yoshito Gotoh, Shigeyuki Ishida, Hiroki Ninomiya, Yoshiyuki Yoshida, Hiroshi Eisaki, Hishiro T Hirose, Taichi Terashima, and Kenji Kawashima. Structural phase transitions and superconductivity induced in antiperovskite phosphide $\text{capd}\text{3p}$. *Inorganic Chemistry*, 59(17):12397–12403, 2020.
- [47] Masatomo Uehara, Akira Uehara, Katsuya Kozawa, and Yoshihide Kimishima. New antiperovskite-type superconductor $\text{znnyni}\text{3}$. *Journal of the Physical Society of Japan*, 78(3):033702–033702, 2009.
- [48] Akira Iyo, Izumi Hase, Hiroshi Fujihisa, Yoshito Gotoh, Shigeyuki Ishida, Hiroki Ninomiya, Yoshiyuki Yoshida, Hiroshi Eisaki, Hishiro T Hirose, Taichi Terashima, et al. Antiperovskite superconductor $\text{lapd}\text{3p}$ with noncentrosymmetric cubic structure. *Inorganic Chemistry*, 60(23):18017–18023, 2021.
- [49] Zhenzhen Hui, Xianwu Tang, Dingfu Shao, Hechang Lei, Jie Yang, Wenhai Song, Hongmei Luo, Xuebin Zhu, and Yuping Sun. Epitaxial antiperovskite superconducting $\text{cunni}\text{3}$ thin films synthesized by chemical solution deposition. *Chemical Communications*, 50(84):12734–12737, 2014.
- [50] Takuto Kawakami, Tetsuya Okamura, Shingo Kobayashi, and Masatoshi Sato. Topological crystalline materials of $j=3/2$ electrons: Antiperovskites, dirac points, and high winding topological superconductivity. *Physical Review X*, 8(4):041026, 2018.
- [51] CMI Okoye. Optical properties of the antiperovskite superconductor $\text{mgcni}\text{3}$. *Journal of Physics: Condensed Matter*, 15(6):833, 2003.
- [52] CMI Okoye. Structural, elastic and electronic properties of new antiperovskite-type superconductor $\text{zn}\text{nni}\text{3}$ from first-principles. *Physica B: Condensed Matter*, 405(6):1562–1570, 2010.
- [53] David Ernsting, David Billington, Thomas E Millichamp, Rebecca A Edwards, Hazel A Sparkes, Nikolai D Zhigadlo, Sean R Giblin, Jonathan W Taylor,

- Jonathan A Duffy, and Stephen B Dugdale. Vacancies, disorder-induced smearing of the electronic structure, and its implications for the superconductivity of anti-perovskite $\text{MgCo}_3\text{Ni}_2\text{S}_8$. *Scientific Reports*, 7(1):1–9, 2017.
- [54] WH Cao, B He, CZ Liao, LH Yang, LM Zeng, and C Dong. Preparation and properties of antiperovskite-type nitrides: InNi_3 and InCo_3 . *Journal of Solid State Chemistry*, 182(12):3353–3357, 2009.
- [55] Hüseyin Murat Tütüncü and GP Srivastava. Theoretical examination of superconductivity in the cubic antiperovskite Cr_3GaN under pressure. *Journal of Applied Physics*, 114(5):053905, 2013.
- [56] BenMaan I Jawdat, Bing Lv, Xiyu Zhu, Yuyi Xue, and Ching-wu Chu. High-pressure and doping studies of the superconducting antiperovskite SrPt_3P . *Physical Review B*, 91(9):094514, 2015.
- [57] M Bilal, Banaras Khan, HA Rahnamaye Aliabad, Muhammad Maqbool, S Jalali Asadabadi, and Iftikhar Ahmad. Thermoelectric properties of SbNi_3C_3 and BiNi_3C_3 for thermoelectric devices and alternative energy applications. *Computer Physics Communications*, 185(5):1394–1398, 2014.
- [58] M Bilal, M Shafiq, B Khan, HA Rahnamaye Aliabad, S Jalali Asadabadi, Rashid Ahmad, Iftikhar Ahmad, et al. Antiperovskite compounds SbNi_3S_3 and BiNi_3S_3 : Potential candidates for thermoelectric renewable energy generators. *Physics Letters A*, 379(3):206–210, 2015.
- [59] Upasana Rani, Peeyush Kumar Kamlesh, Akash Shukla, and Ajay Singh Verma. Emerging potential antiperovskite materials AN_3 (a= p, as, sb, bi; x= sr, ca, mg) for thermoelectric renewable energy generators. *Journal of Solid State Chemistry*, 300:122246, 2021.
- [60] Yoshihiko Okamoto, Akira Sakamaki, and Koshi Takenaka. Thermoelectric properties of antiperovskite calcium oxides Ca_3PbO and Ca_3SnO . *Journal of Applied Physics*, 119(20):205106, 2016.
- [61] DM Hoat. Structural, optoelectronic and thermoelectric properties of antiperovskite compounds AE_3PbS (ae= ca, sr and ba): a first principles study. *Physics Letters A*, 383(14):1648–1654, 2019.
- [62] Y Benmalem, A Abbad, W Benstaali, HA Bentounes, T Seddik, and T Lantri. Thermoelectric, electronic and structural properties of CuMn_3 cubic antiperovskite. *Journal of Computational Electronics*, 17(3):881–887, 2018.

- [63] Masayuki Ochi and Kazuhiko Kuroki. Comparative first-principles study of antiperovskite oxides and nitrides as thermoelectric material: multiple dirac cones, low-dimensional band dispersion, and high valley degeneracy. *Physical Review Applied*, 12(3):034009, 2019.
- [64] Shuai Lin, Peng Tong, Bosen Wang, Jianchao Lin, Yanan Huang, and Yuping Sun. Good thermoelectric performance in strongly correlated system snco_3 with antiperovskite structure. *Inorganic chemistry*, 53(7):3709–3715, 2014.
- [65] Muhammad Bilal, Iftikhar Ahmad, Saeid Jalali Asadabadi, Rashid Ahmad, and Muhammad Maqbool. Thermoelectric properties of metallic antiperovskites axd_3 (a= ge, sn, pb, al, zn, ga; x= n, c; d= ca, fe, co). *Electronic Materials Letters*, 11(3):466–480, 2015.
- [66] Wen Fong Goh and Warren E Pickett. Topological and thermoelectric properties of double antiperovskite pnictides. *Journal of Physics: Condensed Matter*, 32(34):345502, 2020.
- [67] Enamul Haque and M Anwar Hossain. Dft based study on structural stability and transport properties of sr_3asn : A potential thermoelectric material. *Journal of Materials Research*, 34(15):2635–2642, 2019.
- [68] Md Taslimur Rahman, Enamul Haque, and M Anwar Hossain. Elastic, electronic and thermoelectric properties of sr_3mn (m= sb, bi) under pressure. *Journal of Alloys and Compounds*, 783:593–600, 2019.
- [69] Yanping Zhu, Gao Chen, Yijun Zhong, Yubo Chen, Nana Ma, Wei Zhou, and Zongping Shao. A surface-modified antiperovskite as an electrocatalyst for water oxidation. *Nature communications*, 9(1):1–9, 2018.
- [70] K Das, MA Ali, MM Hossain, SH Naqib, AKMA Islam, and MM Uddin. Dynamical stability, vibrational, and optical properties of anti-perovskite a_3bx (ti_3tln , ni_3snn , and co_3alc) phases: A first principles study. *AIP Advances*, 10(9):095226, 2020.
- [71] J Ramanna, N Yedukondalu, K Ramesh Babu, and G Vaitheeswaran. Ab initio study of electronic structure, elastic and optical properties of anti-perovskite type alkali metal oxyhalides. *Solid state sciences*, 20:120–126, 2013.
- [72] Samad Iqbal, G Murtaza, R Khenata, Asif Mahmood, Abdullah Yar, M Muzammil, and Matiullah Khan. Electronic and optical properties of ca_3mn (m= ge, sn, pb, p, as, sb and bi) antiperovskite compounds. *Journal of Electronic Materials*, 45(8):4188–4196, 2016.

- [73] Peng Tong, Bo-Sen Wang, and Yu-Ping Sun. Mn-based antiperovskite functional materials: Review of research. *Chinese Physics B*, 22(6):067501, 2013.
- [74] H Sakakibara, H Ando, Y Kuroki, S Kawai, K Ueda, and H Asano. Magnetic properties and anisotropic magnetoresistance of antiperovskite nitride $\text{mn}_3\text{gan}/\text{co}_3\text{fen}$ exchange-coupled bilayers. *Journal of Applied Physics*, 117(17):17D725, 2015.
- [75] WS Kim, EO Chi, JC Kim, HS Choi, and NH Hur. Close correlation among lattice, spin, and charge in the manganese-based antiperovskite material. *Solid state communications*, 119(8-9):507–510, 2001.
- [76] XH Zhang, Y Yin, Q Yuan, JC Han, ZH Zhang, JK Jian, JG Zhao, and B Song. Magnetoresistance reversal in antiperovskite compound $\text{mn}_3\text{cu}_0.5\text{zn}_0.5\text{n}$. *Journal of Applied Physics*, 115(12):123905, 2014.
- [77] K Kamishima, T Goto, H Nakagawa, N Miura, M Ohashi, N Mori, T Sasaki, and T Kanomata. Giant magnetoresistance in the intermetallic compound mn_3gac . *Physical Review B*, 63(2):024426, 2000.
- [78] Wei Xia, Yang Zhao, Feipeng Zhao, Keegan Adair, Ruo Zhao, Shuai Li, Ruqiang Zou, Yusheng Zhao, and Xueliang Sun. Antiperovskite electrolytes for solid-state batteries. *Chemical Reviews*, 2022.
- [79] Jingfeng Zheng, Hong Fang, Longlong Fan, Yang Ren, Puru Jena, and Yiyang Wu. Antiperovskite k_3oi for k-ion solid state electrolyte. *The Journal of Physical Chemistry Letters*, 12(30):7120–7126, 2021.
- [80] Yutao Li, Weidong Zhou, Sen Xin, Shuai Li, Jinlong Zhu, Xujie Lü, Zhiming Cui, Quanxi Jia, Jianshi Zhou, Yusheng Zhao, et al. Fluorine-doped antiperovskite electrolyte for all-solid-state lithium-ion batteries. *Angewandte Chemie International Edition*, 55(34):9965–9968, 2016.
- [81] James A Dawson, Tavleen S Attari, Hungru Chen, Steffen P Emge, Karen E Johnston, and M Saiful Islam. Elucidating lithium-ion and proton dynamics in anti-perovskite solid electrolytes. *Energy & Environmental Science*, 11(10):2993–3002, 2018.
- [82] Jun Dai, Ming-Gang Ju, Liang Ma, and Xiao Cheng Zeng. $\text{Bi}(\text{sb})\text{nca}_3$: Expansion of perovskite photovoltaics into all-inorganic anti-perovskite materials. *The Journal of Physical Chemistry C*, 123(11):6363–6369, 2019.
- [83] Dan Han, Chunbao Feng, Mao-Hua Du, Tao Zhang, Shizhe Wang, Gang Tang, Thomas Bein, and Hubert Ebert. Design of high-performance lead-free quaternary

- antiperovskites for photovoltaics via ion type inversion and anion ordering. *Journal of the American Chemical Society*, 143(31):12369–12379, 2021.
- [84] Guo-Ping Li, Si-Qi Lu, Xin Chen, Wei-Qiang Liao, Yuan-Yuan Tang, and Ren-Gen Xiong. A three-dimensional m3ab-type hybrid organic–inorganic antiperovskite ferroelectric: [c3h7fn] 3 [sncl6] cl. *Chemistry–A European Journal*, 25(72):16625–16629, 2019.
- [85] Rui Yu, Hongming Weng, Zhong Fang, Xi Dai, and Xiao Hu. Topological node-line semimetal and dirac semimetal state in antiperovskite cu 3 pdn. *Physical review letters*, 115(3):036807, 2015.
- [86] Yuan Fang and Jennifer Cano. Higher-order topological insulators in antiperovskites. *Physical Review B*, 101(24):245110, 2020.
- [87] Yan Sun, Xing-Qiu Chen, Seiji Yunoki, Dianzhong Li, and Yiyi Li. New family of three-dimensional topological insulators with antiperovskite structure. *Physical review letters*, 105(21):216406, 2010.
- [88] Timothy H Hsieh, Junwei Liu, and Liang Fu. Topological crystalline insulators and dirac octets in antiperovskites. *Physical Review B*, 90(8):081112, 2014.
- [89] Youngho Kang and Seungwu Han. Antiperovskite oxides as promising candidates for high-performance ferroelectric photovoltaics: First-principles investigation on ba4as2o and ba4sb2o. *ACS Applied Materials & Interfaces*, 12(39):43798–43804, 2020.
- [90] Zhong-Xia Wang, Yi Zhang, Yuan-Yuan Tang, Peng-Fei Li, and Ren-Gen Xiong. Fluoridation achieved antiperovskite molecular ferroelectric in [(ch3) 2 (f-ch2ch2) nh] 3 (cdcl3)(cdcl4). *Journal of the American Chemical Society*, 141(10):4372–4378, 2019.
- [91] Jeong-Hyeon Kim, Seul-Gi Kim, and Nam-Gyu Park. Effect of chemical bonding nature of post-treatment materials on photovoltaic performance of perovskite solar cells. *ACS Energy Letters*, 6(10):3435–3442, 2021.
- [92] Marc De Graef and Michael E McHenry. *Structure of materials: an introduction to crystallography, diffraction and symmetry*. Cambridge University Press, 2012.
- [93] LL Boyer and PJ Edwardson. Perovskite to antiperovskite in abf3 compounds. *Ferroelectrics*, 104(1):417–422, 1990.
- [94] Dingfu Shao, Wenjian Lu, Peng Tong, Shuai Lin, Jianchao Lin, and Yuping Sun. Prediction of superconductivity in 3 d transition-metal based antiperovskites via

- magnetic phase diagram. *Journal of the Physical Society of Japan*, 83(5):054704, 2014.
- [95] Rainer Niewa. Alkaline-earth metal nitrides of the main-group elements: Crystal structures and properties of inverse perovskites. *Zeitschrift für anorganische und allgemeine Chemie*, 639(10):1699–1715, 2013.
- [96] BV Beznosikov. Predicted nitrides with an antiperovskite structure. *Journal of Structural Chemistry*, 44(5):885–888, 2003.
- [97] CR Groom, IJ Bruno, MP Lightfoot, and SC Ward. *Acta crystallogr., sect. b: Struct. sci., cryst. eng. mater.*, 2016.
- [98] DE Cox and AW Sleight. Mixed-valent $\text{Ba}_2\text{Bi}_3\text{O}_6$: structure and properties vs temperature. *Acta Crystallographica Section B: Structural Crystallography and Crystal Chemistry*, 35(1):1–10, 1979.
- [99] H Boller. Komplexcarbid und-nitrid mit aufgefülltem u_3si -typ. *Monatshefte für Chemie/Chemical Monthly*, 99(6):2444–2449, 1968.
- [100] Mm R Fruchart, R Madar, M Barberon, Mme E Fruchart, and MG Lorthioir. Transitions magnétiques et déformations cristallographiques associées dans les nitrures du type perovskite znmn_3n et snmn_3n . *Le Journal de Physique Colloques*, 32(C1):C1–982, 1971.
- [101] Yusheng Zhao and Luke L Daemen. Superionic conductivity in lithium-rich antiperovskites. *Journal of the American Chemical Society*, 134(36):15042–15047, 2012.
- [102] T Takayama, K Kuwano, D Hirai, Y Katsura, A Yamamoto, and H Takagi. Strong coupling superconductivity at 8.4 k in an antiperovskite phosphide $\text{sr pt}_3\text{p}$. *Physical Review Letters*, 108(23):237001, 2012.
- [103] Ernst Bauer, Gerfried Hilscher, Herwig Michor, Ch Paul, Ernst-Wilhelm Scheidt, A Griбанov, Yu Seropegin, H Noël, M Sigrist, and Peter Rogl. Heavy fermion superconductivity and magnetic order in noncentrosymmetric cept_3si . *Physical review letters*, 92(2):027003, 2004.
- [104] T He, Q Huang, AP Ramirez, Y Wang, KA Regan, N Rogado, MA Hayward, MK Haas, JS Slusky, K Inumara, et al. Superconductivity in the non-oxide perovskite mgcni_3 . *Nature*, 411(6833):54–56, 2001.
- [105] JohnÁS O Evans. Negative thermal expansion materials. *Journal of the Chemical Society, Dalton Transactions*, (19):3317–3326, 1999.

- [106] Jun Chen, Lei Hu, Jinxia Deng, and Xianran Xing. Negative thermal expansion in functional materials: controllable thermal expansion by chemical modifications. *Chemical Society Reviews*, 44(11):3522–3567, 2015.
- [107] K Takenaka and H Takagi. Zero thermal expansion in a pure-form antiperovskite manganese nitride. *Applied Physics Letters*, 94(13):131904, 2009.
- [108] T Hamada and K Takenaka. Giant negative thermal expansion in antiperovskite manganese nitrides. *Journal of Applied Physics*, 109(7):07E309, 2011.
- [109] Rongjin Huang, Laifeng Li, Fangshuo Cai, Xiangdong Xu, and Lihe Qian. Low-temperature negative thermal expansion of the antiperovskite manganese nitride Mn_3Cu codoped with Ge and Si. *Applied Physics Letters*, 93(8):081902, 2008.
- [110] K Takenaka, K Asano, M Misawa, and H Takagi. Negative thermal expansion in Ge-free antiperovskite manganese nitrides: Tin-doping effect. *Applied Physics Letters*, 92(1):011927, 2008.
- [111] BY Qu and BC Pan. Nature of the negative thermal expansion in antiperovskite compound Mn_3Zn . *Journal of Applied Physics*, 108(11):113920, 2010.
- [112] P Tong, Despina Louca, Graham King, Anna Llobet, JC Lin, and YP Sun. Magnetic transition broadening and local lattice distortion in the negative thermal expansion antiperovskite $\text{Cu}_1\text{XSn}_2\text{Mn}_3$. *Applied Physics Letters*, 102(4):041908, 2013.
- [113] Cong Wang, Lihua Chu, Qingrong Yao, Ying Sun, Meimei Wu, Lei Ding, Jun Yan, Yuanyuan Na, Weihua Tang, Guannan Li, et al. Tuning the range, magnitude, and sign of the thermal expansion in intermetallic $\text{Mn}_3(\text{Zn}, \text{M})\text{X}_n$ ($\text{M} = \text{Ag}, \text{Ge}$). *Physical Review B*, 85(22):220103, 2012.
- [114] Ying Sun, Cong Wang, Yongchun Wen, Lihua Chu, Hui Pan, Man Nie, and Meibo Tang. Negative thermal expansion and magnetic transition in anti-perovskite structured $\text{Mn}_3\text{Zn}_1\text{X}_n$ compounds. *Journal of the American Ceramic Society*, 93(8):2178–2181, 2010.
- [115] K Takenaka, T Hamada, D Kasugai, and N Sugimoto. Tailoring thermal expansion in metal matrix composites blended by antiperovskite manganese nitrides exhibiting giant negative thermal expansion. *Journal of Applied Physics*, 112(8):083517, 2012.
- [116] Zhen Chen, Rongjin Huang, Xinxin Chu, Zhixiong Wu, Zhuonan Liu, Yuan Zhou, and Laifeng Li. Negative thermal expansion and nearly zero temperature coefficient

- of resistivity in anti-perovskite manganese nitride mn_3cun co-doped with ag and sn. *Cryogenics*, 52(11):629–631, 2012.
- [117] TA Mary, JSO Evans, T Vogt, and AW Sleight. Negative thermal expansion from 0.3 to 1050 kelvin in zrw_2o_8 . *Science*, 272(5258):90–92, 1996.
- [118] Yonggang Wang, Ting Wen, Changyong Park, Curtis Kenney-Benson, Michael Pravica, Wenge Yang, and Yusheng Zhao. Robust high pressure stability and negative thermal expansion in sodium-rich antiperovskites na_3obr and na_4oi_2 . *Journal of Applied Physics*, 119(2):025901, 2016.
- [119] Rudolf Zeller. Spin-polarized dft calculations and magnetism. *Computational Nanoscience: Do It Yourself*, 31:419–445, 2006.
- [120] Tat-Sang Choy, Jian Chen, and Selman Hershfield. Correlation between spin polarization and magnetic moment in ferromagnetic alloys. *Journal of applied physics*, 86(1):562–564, 1999.
- [121] J-M Tarascon and Michel Armand. Issues and challenges facing rechargeable lithium batteries. In *Materials for sustainable energy: a collection of peer-reviewed research and review articles from Nature Publishing Group*, pages 171–179. World Scientific, 2011.
- [122] Ernest Ahiavi, James A Dawson, Ulas Kudu, Matthieu Courty, M Saiful Islam, Oliver Clemens, Christian Masquelier, and Theodosios Famprikis. Mechanochemical synthesis and ion transport properties of na_3ox ($x = \text{cl, br, i}$ and bh_4) antiperovskite solid electrolytes. *Journal of Power Sources*, 471:228489, 2020.
- [123] F Grandjean and A Gerard. Study by mossbauer spectroscopy of the series of perovskite carbides $\text{m}_3\text{m}'\text{c}$ with $\text{m} = \text{fe}$ or mn , and $\text{m}' = \text{al, ga, ge, zn, sn}$. *Journal of Physics F: Metal Physics*, 6(3):451, 1976.
- [124] BS Wang, P Tong, YP Sun, XB Zhu, ZR Yang, WH Song, and JM Dai. Observation of spin-glass behavior in antiperovskite compound sn_3cfe . *Applied Physics Letters*, 97(4):042508, 2010.
- [125] BS Wang, P Tong, YP Sun, LJ Li, W Tang, WJ Lu, XB Zhu, ZR Yang, and WH Song. Enhanced giant magnetoresistance in ni-doped antiperovskite compounds $\text{gacmn}_3\text{-xni}_x$ ($x = 0.05, 0.10$). *Applied Physics Letters*, 95(22):222509, 2009.
- [126] Jiayi Zhang, Xiao Zhao, Li Du, Yutao Li, Longhai Zhang, Shijun Liao, John B Goodenough, and Zhiming Cui. Antiperovskite nitrides $\text{cunco}_3\text{-xv}_x$: Highly efficient and durable electrocatalysts for the oxygen-evolution reaction. *Nano Letters*, 19(10):7457–7463, 2019.

- [127] Shancang Li, Li Da Xu, and Shanshan Zhao. The internet of things: a survey. *Information systems frontiers*, 17(2):243–259, 2015.
- [128] Pham Nam Hai, Shinobu Ohya, Masaaki Tanaka, Stewart E Barnes, and Sadamichi Maekawa. Electromotive force and huge magnetoresistance in magnetic tunnel junctions. *Nature*, 458(7237):489–492, 2009.
- [129] Pham Nam Hai. Electromotive force and huge magnetoresistance in magnetic tunnel junctions with zinc-blende mnas nano-magnets. In *APS March Meeting Abstracts*, volume 2010, pages L36–010, 2010.
- [130] Arne Brataas, Yaroslav Tserkovnyak, Gerrit EW Bauer, and Bertrand I Halperin. Spin battery operated by ferromagnetic resonance. *Physical Review B*, 66(6):060404, 2002.
- [131] Yiqun Xie, Mingyan Chen, Zewen Wu, Yibin Hu, Yin Wang, Jian Wang, and Hong Guo. Two-dimensional photogalvanic spin-battery. *Physical Review Applied*, 10(3):034005, 2018.
- [132] ShiJing Gong, HangChen Ding, WanJiao Zhu, ChunGang Duan, Ziqiang Zhu, and JunHao Chu. A new pathway towards all-electric spintronics: electric-field control of spin states through surface/interface effects. *Science China Physics, Mechanics and Astronomy*, 56(1):232–244, 2013.
- [133] Tomoyasu Taniyama, Eiji Wada, Mitsuru Itoh, and Masahito Yamaguchi. Electrical and optical spin injection in ferromagnet/semiconductor heterostructures. *NPG Asia Materials*, 3(7):65–73, 2011.
- [134] Sergio O Valenzuela. Nonlocal electronic spin detection, spin accumulation and the spin hall effect. *International Journal of Modern Physics B*, 23(11):2413–2438, 2009.
- [135] Zeang Zhao, Jiangtao Wu, Xiaoming Mu, Haosen Chen, H Jerry Qi, and Daining Fang. Origami by frontal photopolymerization. *Science advances*, 3(4):e1602326, 2017.
- [136] V Sivakumar, CA Ross, N Yabuuchi, Y Shao-Horn, K Persson, and G Ceder. Electrochemical control of the magnetic moment of cro₂. *Journal of The Electrochemical Society*, 155(8):P83, 2008.
- [137] G Tewodros Aregai, K Vijaya Babu, B Vikram Babu, PSV Subba Rao, and V Veeraiah. Structural, electrical and electrochemical studies of copper substituted layered lini_{1/3}co_{1/3}mn_{1/3}o₂ cathode materials. *South African journal of chemical engineering*, 27:43–52, 2019.

- [138] Carlos M Costa, Karla J Merazzo, Renato Gonçalves, Charles Amos, and Senentxu Lanceros-Méndez. Magnetically active lithium-ion batteries towards battery performance improvement. *Iscience*, 24(6):102691, 2021.
- [139] Christian Reitz, Christian Suchomski, Di Wang, Horst Hahn, and Torsten Brezesinski. In situ tuning of magnetization via topotactic lithium insertion in ordered mesoporous lithium ferrite thin films. *Journal of Materials Chemistry C*, 4(38):8889–8896, 2016.
- [140] Qingyun Zhang, Xi Luo, Luning Wang, Lifang Zhang, Bilal Khalid, Jianghong Gong, and Hui Wu. Lithium-ion battery cycling for magnetism control. *Nano letters*, 16(1):583–587, 2016.
- [141] Junru Wang, Feng Li, Bo Yang, Xiaobiao Liu, and Mingwen Zhao. Half-metallic $\text{Li}_3\text{V}_2\text{O}_7$: a potential anode material for li-ion spin batteries. *Journal of Materials Chemistry A*, 5(40):21486–21490, 2017.
- [142] Lei Gao, Hao Zhang, Yuechao Wang, Shuai Li, Ruo Zhao, Yonggang Wang, Song Gao, Lunhua He, Hai-Feng Song, Ruqiang Zou, et al. Mechanism of enhanced ionic conductivity by rotational nitrite group in antiperovskite Na_3O_2 . *Journal of Materials Chemistry A*, 8(40):21265–21272, 2020.
- [143] MH Braga, Jorge Amaral Ferreira, V Stockhausen, JE Oliveira, and A El-Azab. Novel Li_3O based glasses with superionic properties for lithium batteries. *Journal of Materials Chemistry A*, 2(15):5470–5480, 2014.
- [144] Martin Jansen. Volume effect or paddle-wheel mechanism—fast alkali-metal ionic conduction in solids with rotationally disordered complex anions. *Angewandte Chemie International Edition in English*, 30(12):1547–1558, 1991.
- [145] Yonggang Wang, Qingfei Wang, Zhenpu Liu, Zhengyang Zhou, Shuai Li, Jinlong Zhu, Ruqiang Zou, Yingxia Wang, Jianhua Lin, and Yusheng Zhao. Structural manipulation approaches towards enhanced sodium ionic conductivity in Na -rich antiperovskites. *Journal of Power Sources*, 293:735–740, 2015.
- [146] Xujie Lü, Gang Wu, John W Howard, Aiping Chen, Yusheng Zhao, Luke L Dae-men, and Quanxi Jia. Li-rich anti-perovskite Li_3OCl films with enhanced ionic conductivity. *Chemical Communications*, 50(78):11520–11522, 2014.
- [147] Zhi Deng, Balachandran Radhakrishnan, and Shyue Ping Ong. Rational composition optimization of the lithium-rich $\text{Li}_3\text{OCl}_{1-x}\text{Br}_x$ anti-perovskite superionic conductors. *Chemistry of Materials*, 27(10):3749–3755, 2015.

- [148] Eliana Quartarone and Piercarlo Mustarelli. Electrolytes for solid-state lithium rechargeable batteries: recent advances and perspectives. *Chemical Society Reviews*, 40(5):2525–2540, 2011.
- [149] AM Tishin. Magnetocaloric effect: Current situation and future trends. *Journal of Magnetism and Magnetic Materials*, 316(2):351–357, 2007.
- [150] BG Shen, JR Sun, FX Hu, HW Zhang, and ZH Cheng. Recent progress in exploring magnetocaloric materials. *Advanced Materials*, 21(45):4545–4564, 2009.
- [151] Stuart A Wolf and Daryl Treger. Spintronics: A new paradigm for electronics for the new millennium. *IEEE Transactions on Magnetism*, 36(5):2748–2751, 2000.
- [152] Clarence Zener. Interaction between the d-shells in the transition metals. ii. ferromagnetic compounds of manganese with perovskite structure. *Physical Review*, 82(3):403, 1951.
- [153] Peter ER Blanchard, Emily Reynolds, Brendan J Kennedy, Justin A Kimpton, Maxim Avdeev, and Alexei A Belik. Anomalous thermal expansion in orthorhombic perovskite srro3: Interplay between spin-orbit coupling and the crystal lattice. *Physical Review B*, 89(21):214106, 2014.
- [154] Bing He, Cheng Dong, Lihong Yang, Xiaochao Chen, Linhui Ge, Libin Mu, and Youguo Shi. Cunni3: a new nitride superconductor with antiperovskite structure. *Superconductor Science and Technology*, 26(12):125015, 2013.
- [155] S Mollah. The physics of the non-oxide perovskite superconductor mgcni3. *Journal of Physics: Condensed Matter*, 16(43):R1237, 2004.
- [156] Yang Zhao, Xifei Li, Bo Yan, Dongbin Xiong, Dejun Li, Stephen Lawes, and Xueliang Sun. Recent developments and understanding of novel mixed transition-metal oxides as anodes in lithium ion batteries. *Advanced Energy Materials*, 6(8):1502175, 2016.
- [157] Y Yuan, L Yang, B He, E Pervaiz, Z Shao, and M Yang. Cobalt–zinc nitride on nitrogen doped carbon black nanohybrids as a non-noble metal electrocatalyst for oxygen reduction reaction. *Nanoscale*, 9(19):6259–6263, 2017.
- [158] Dimitri D Vaughn II, Jose Araujo, Praveen Meduri, Juan F Callejas, Michael A Hickner, and Raymond E Schaak. Solution synthesis of cu3pdn nanocrystals as ternary metal nitride electrocatalysts for the oxygen reduction reaction. *Chemistry of Materials*, 26(21):6226–6232, 2014.

- [159] Paolo Giannozzi, Stefano Baroni, Nicola Bonini, Matteo Calandra, Roberto Car, Carlo Cavazzoni, Davide Ceresoli, Guido L Chiarotti, Matteo Cococcioni, Ismaila Dabo, et al. Quantum espresso: a modular and open-source software project for quantum simulations of materials. *Journal of physics: Condensed matter*, 21(39):395502, 2009.
- [160] David Vanderbilt. Soft self-consistent pseudopotentials in a generalized eigenvalue formalism. *Physical review B*, 41(11):7892, 1990.
- [161] Kari Laasonen, Alfredo Pasquarello, Roberto Car, Changyol Lee, and David Vanderbilt. Car-parrinello molecular dynamics with vanderbilt ultrasoft pseudopotentials. *Physical Review B*, 47(16):10142, 1993.
- [162] Kevin F Garrity, Joseph W Bennett, Karin M Rabe, and David Vanderbilt. Pseudopotentials for high-throughput dft calculations. *Computational Materials Science*, 81:446–452, 2014.
- [163] John P Perdew, Kieron Burke, and Matthias Ernzerhof. Generalized gradient approximation made simple. *Physical review letters*, 77(18):3865, 1996.
- [164] Hendrik J Monkhorst and James D Pack. Special points for brillouin-zone integrations. *Physical review B*, 13(12):5188, 1976.
- [165] Gianluca Prandini, Antimo Marrazzo, Ivano E Castelli, Nicolas Mounet, and Nicola Marzari. Precision and efficiency in solid-state pseudopotential calculations. *npj Computational Materials*, 4(1):1–13, 2018.
- [166] Zhongxue Chen, Yuliang Cao, Jiangfeng Qian, Xinping Ai, and Hanxi Yang. Facile synthesis and stable lithium storage performances of sn-sandwiched nanoparticles as a high capacity anode material for rechargeable li batteries. *Journal of Materials Chemistry*, 20(34):7266–7271, 2010.
- [167] Hangjun Ying and Wei-Qiang Han. Metallic sn-based anode materials: application in high-performance lithium-ion and sodium-ion batteries. *Advanced Science*, 4(11):1700298, 2017.
- [168] Zhixin Dong, Qi Wang, Ruibo Zhang, Natasha A Chernova, Fredrick Omenya, Dongsheng Ji, and M Stanley Whittingham. Reaction mechanism of the sn₂fe anode in lithium-ion batteries. *ACS omega*, 4(27):22345–22355, 2019.
- [169] Huajun Tian, Fengxia Xin, Xiaoliang Wang, Wei He, and Weiqiang Han. High capacity group-iv elements (si, ge, sn) based anodes for lithium-ion batteries. *Journal of Materiomics*, 1(3):153–169, 2015.

- [170] Jun Song Chen, Yan Ling Cheah, Yuan Ting Chen, N Jayaprakash, Srinivasan Madhavi, Yan Hui Yang, and Xiong Wen Lou. Sno₂ nanoparticles with controlled carbon nanocoating as high-capacity anode materials for lithium-ion batteries. *The Journal of Physical Chemistry C*, 113(47):20504–20508, 2009.
- [171] Elangbam Chitra Devi and Shougaijam Dorendrajit Singh. Tracing the magnetization curves: a review on their importance, strategy, and outcomes. *Journal of Superconductivity and Novel Magnetism*, 34(1):15–25, 2021.
- [172] Elangbam Chitra Devi and Shougaijam Dorendrajit Singh. Manifestation of magnetic characteristics of zinc ferrite nanoparticles using the langevin function. *Journal of Superconductivity and Novel Magnetism*, 34(2):617–622, 2021.
- [173] Hans H Stadelmaier and LJ Huetter. Ternary carbides of the transition metals nickel, cobalt, iron, manganese with zinc and tin. *Acta Metallurgica*, 7(6):415–419, 1959.
- [174] James E Saal, Scott Kirklin, Muratahan Aykol, Bryce Meredig, and Christopher Wolverton. Materials design and discovery with high-throughput density functional theory: the open quantum materials database (oqmd). *Jom*, 65(11):1501–1509, 2013.
- [175] Scott Kirklin, James E Saal, Bryce Meredig, Alex Thompson, Jeff W Doak, Muratahan Aykol, Stephan Rühl, and Chris Wolverton. The open quantum materials database (oqmd): assessing the accuracy of dft formation energies. *npj Computational Materials*, 1(1):1–15, 2015.
- [176] JI Langford, RJ Cernik, and D Louer. The breadth and shape of instrumental line profiles in high-resolution powder diffraction. *Journal of applied crystallography*, 24(5):913–919, 1991.
- [177] Yoji Imai, Yasuhiko Takahashi, and Toshiya Kumagai. Relations of electronic energies and magnetic moments of tetra-3d metal (mn, fe, co and ni) nitrides calculated using a plane-wave basis method. *Journal of Magnetism and Magnetic Materials*, 322(18):2665–2669, 2010.
- [178] M Sifkovits, H Smolinski, S Hellwig, and W Weber. Interplay of chemical bonding and magnetism in fe₄n, fe₃n and ζ-fe₂n. *Journal of magnetism and magnetic materials*, 204(3):191–198, 1999.
- [179] Y Wang. Phys. rev. b: Condens. matter mater. phys. 2006.
- [180] Keita Ito, Kazuaki Okamoto, Kazunori Harada, Tatsunori Sanai, Kaoru Toko, Shigenori Ueda, Yoji Imai, Taichi Okuda, Koji Miyamoto, Akio Kimura, et al.

- Negative spin polarization at the fermi level in fe4n epitaxial films by spin-resolved photoelectron spectroscopy. *Journal of applied physics*, 112(1):013911, 2012.
- [181] Hongshi Li, Xuan Li, Dongrin Kim, Gejian Zhao, Delin Zhang, Zhitao Diao, Tingyong Chen, and Jian-Ping Wang. High spin polarization in epitaxial fe4n thin films using cr and ag as buffer layers. *Applied Physics Letters*, 112(16):162407, 2018.
- [182] Vinodkumar Etacheri, Rotem Marom, Ran Elazari, Gregory Salitra, and Doron Aurbach. Challenges in the development of advanced li-ion batteries: a review. *Energy & Environmental Science*, 4(9):3243–3262, 2011.
- [183] Poulomi Roy and Suneel Kumar Srivastava. Nanostructured anode materials for lithium ion batteries. *Journal of Materials Chemistry A*, 3(6):2454–2484, 2015.
- [184] John B Goodenough and Kyu-Sung Park. The li-ion rechargeable battery: a perspective. *Journal of the American Chemical Society*, 135(4):1167–1176, 2013.
- [185] Changju Chae, Hyung-Joo Noh, Jung Kyoo Lee, Bruno Scrosati, and Yang-Kook Sun. A high-energy li-ion battery using a silicon-based anode and a nanostructured layered composite cathode. *Advanced Functional Materials*, 24(20):3036–3042, 2014.
- [186] Xin Su, Qingliu Wu, Juchuan Li, Xingcheng Xiao, Amber Lott, Wenquan Lu, Brian W Sheldon, and Ji Wu. Silicon-based nanomaterials for lithium-ion batteries: a review. *Advanced Energy Materials*, 4(1):1300882, 2014.
- [187] Hanna Bryngelsson, Jonas Eskhult, Leif Nyholm, Merja Herranen, Oscar Alm, and Kristina Edström. Electrodeposited sb and sb/sb2o3 nanoparticle coatings as anode materials for li-ion batteries. *Chemistry of materials*, 19(5):1170–1180, 2007.
- [188] Tong Shen, Xin-hui Xia, Dong Xie, Zhu-jun Yao, Yu Zhong, Ji-ye Zhan, Dong-huang Wang, Jian-bo Wu, Xiu-li Wang, and Jiang-ping Tu. Encapsulating silicon nanoparticles into mesoporous carbon forming pomegranate-structured microspheres as a high-performance anode for lithium ion batteries. *Journal of Materials Chemistry A*, 5(22):11197–11203, 2017.
- [189] Jin-Yi Li, Quan Xu, Ge Li, Ya-Xia Yin, Li-Jun Wan, and Yu-Guo Guo. Research progress regarding si-based anode materials towards practical application in high energy density li-ion batteries. *Materials Chemistry Frontiers*, 1(9):1691–1708, 2017.
- [190] Bin Wang, Xianglong Li, Xianfeng Zhang, Bin Luo, Meihua Jin, Minghui Liang, Shadi A Dayeh, ST Picraux, and Linjie Zhi. Adaptable silicon-carbon nanocables

- sandwiched between reduced graphene oxide sheets as lithium ion battery anodes. *ACS nano*, 7(2):1437–1445, 2013.
- [191] Kingshuk Roy, Malik Wahid, Dhanya Puthusseri, Apurva Patrike, Subas Muduli, Ramanathan Vaidhyanathan, and Satishchandra Ogale. High capacity, power density and cycling stability of silicon li-ion battery anodes with a few layer black phosphorus additive. *Sustainable energy & fuels*, 3(1):245–250, 2019.
- [192] Dhanya Puthusseri, Malik Wahid, and Satishchandra Ogale. Conversion-type anode materials for alkali-ion batteries: state of the art and possible research directions. *ACS omega*, 3(4):4591–4601, 2018.
- [193] John Muldoon, Claudiu B Bucur, and Thomas Gregory. Quest for nonaqueous multivalent secondary batteries: magnesium and beyond. *Chemical reviews*, 114(23):11683–11720, 2014.
- [194] Liwei Su, Yu Jing, and Zhen Zhou. Li ion battery materials with core-shell nanostructures. *Nanoscale*, 3(10):3967–3983, 2011.
- [195] Hyesun Kim and Jaephil Cho. Superior lithium electroactive mesoporous si@carbon core-shell nanowires for lithium battery anode material. *Nano letters*, 8(11):3688–3691, 2008.
- [196] YuHong Xu, GePing Yin, YuLin Ma, PengJian Zuo, and XinQun Cheng. Nano-sized core/shell silicon@carbon anode material for lithium ion batteries with polyvinylidene fluoride as carbon source. *Journal of Materials Chemistry*, 20(16):3216–3220, 2010.
- [197] Yong-Sheng Hu, Rezan Demir-Cakan, Maria-Magdalena Titirici, Jens-Oliver Müller, Robert Schlögl, Markus Antonietti, and Joachim Maier. Superior storage performance of a si@si_{0.9}x/c nanocomposite as anode material for lithium-ion batteries. *Angewandte Chemie International Edition*, 47(9):1645–1649, 2008.
- [198] Pengfei Gao, Jianwei Fu, Jun Yang, Rongguan Lv, Jiulin Wang, Yanna Nuli, and Xiaozhen Tang. Microporous carbon coated silicon core/shell nanocomposite via in situ polymerization for advanced li-ion battery anode material. *Physical Chemistry Chemical Physics*, 11(47):11101–11105, 2009.
- [199] Liangbing Hu, Hui Wu, Seung Sae Hong, Lifeng Cui, James R McDonough, Sy Bohy, and Yi Cui. Si nanoparticle-decorated si nanowire networks for li-ion battery anodes. *Chemical Communications*, 47(1):367–369, 2011.
- [200] Liwei Su, Zhen Zhou, and Manman Ren. Core double-shell si@sio₂@c nanocomposites as anode materials for li-ion batteries. *Chemical communications*, 46(15):2590–2592, 2010.

- [201] Gaelle Derrien, Jusef Hassoun, Stefania Panero, and Bruno Scrosati. Nanostructured sn-c composite as an advanced anode material in high-performance lithium-ion batteries. *Advanced Materials*, 19(17):2336–2340, 2007.
- [202] Min Gyu Kim, Soojin Sim, and Jaephil Cho. Novel core-shell sn-cu anodes for lithium rechargeable batteries prepared by a redox-transmetalation reaction. *Advanced Materials*, 22(45):5154–5158, 2010.
- [203] Zhen Xiao, Yang Xia, Zhaohui Ren, Zhenya Liu, Gang Xu, Chunying Chao, Xiang Li, Ge Shen, and Gaorong Han. Facile synthesis of single-crystalline mesoporous α - Fe_2O_3 and Fe_3O_4 nanorods as anode materials for lithium-ion batteries. *Journal of Materials Chemistry*, 22(38):20566–20573, 2012.
- [204] Theivanayagam Muraliganth, Arumugam Vadivel Murugan, and Arumugam Manthiram. Facile synthesis of carbon-decorated single-crystalline Fe_3O_4 nanowires and their application as high performance anode in lithium ion batteries. *Chemical communications*, (47):7360–7362, 2009.
- [205] Wei-Ming Zhang, Xing-Long Wu, Jin-Song Hu, Yu-Guo Guo, and Li-Jun Wan. Carbon coated Fe_3O_4 nanospindles as a superior anode material for lithium-ion batteries. *Advanced Functional Materials*, 18(24):3941–3946, 2008.
- [206] Xiaoming Sun, Junfeng Liu, and Yadong Li. Oxides@ c core-shell nanostructures: One-pot synthesis, rational conversion, and li storage property. *Chemistry of Materials*, 18(15):3486–3494, 2006.
- [207] Jian Yan, Afriyanti Sumboja, Eugene Khoo, and Pooi See Lee. V_2O_5 loaded on SnO_2 nanowires for high-rate li ion batteries. *Advanced Materials*, 23(6):746–750, 2011.
- [208] Ping Wu, Ning Du, Hui Zhang, Jingxue Yu, and Deren Yang. Cnts@ SnO_2 @ c coaxial nanocables with highly reversible lithium storage. *The Journal of Physical Chemistry C*, 114(51):22535–22538, 2010.
- [209] Liwen Ji, Zhan Lin, Bingkun Guo, Andrew J Medford, and Xiangwu Zhang. Assembly of carbon- SnO_2 core-sheath composite nanofibers for superior lithium storage. *Chemistry—A European Journal*, 16(38):11543–11548, 2010.
- [210] Yu-Sheng Lin, Jenq-Gong Duh, and Min-Hsiu Hung. Shell-by-shell synthesis and applications of carbon-coated SnO_2 hollow nanospheres in lithium-ion battery. *The Journal of Physical Chemistry C*, 114(30):13136–13141, 2010.
- [211] Xiong Wen Lou, Chang Ming Li, and Lynden A Archer. Designed synthesis of coaxial SnO_2 @ carbon hollow nanospheres for highly reversible lithium storage. *Advanced Materials*, 21(24):2536–2539, 2009.

- [212] Xiong Wen Lou, Da Deng, Jim Yang Lee, and Lynden A Archer. Preparation of $\text{SnO}_2/\text{carbon}$ composite hollow spheres and their lithium storage properties. *Chemistry of Materials*, 20(20):6562–6566, 2008.
- [213] Rong Yang, Wei Zhao, Jie Zheng, Xuanzhou Zhang, and Xingguo Li. One-step synthesis of carbon-coated tin dioxide nanoparticles for high lithium storage. *The Journal of Physical Chemistry C*, 114(47):20272–20276, 2010.
- [214] Hui Qiao, Zhi Zheng, Lizhi Zhang, and Lifeng Xiao. $\text{SnO}_2@ \text{C}$ core-shell spheres: synthesis, characterization, and performance in reversible Li-ion storage. *Journal of materials science*, 43(8):2778–2784, 2008.
- [215] Baohua Zhang, Xiaoyuan Yu, Chunyu Ge, Xianming Dong, Yueping Fang, Zesheng Li, and Hongqiang Wang. Novel 3-d superstructures made up of $\text{SnO}_2@ \text{C}$ core-shell nanochains for energy storage applications. *Chemical Communications*, 46(48):9188–9190, 2010.
- [216] C Lai, HZ Zhang, GR Li, and XP Gao. Mesoporous polyaniline/ TiO_2 microspheres with core-shell structure as anode materials for lithium ion battery. *Journal of Power Sources*, 196(10):4735–4740, 2011.
- [217] Sangaraju Shanmugam, Alexandra Gabashvili, David S Jacob, Jimmy C Yu, and Aharon Gedanken. Synthesis and characterization of $\text{TiO}_2@ \text{C}$ core-shell composite nanoparticles and evaluation of their photocatalytic activities. *Chemistry of Materials*, 18(9):2275–2282, 2006.
- [218] Hyesun Kim, Min Gyu Kim, Tae Joo Shin, Hyun-Jun Shin, and Jaephil Cho. $\text{TiO}_2@ \text{Sn}$ core-shell nanotubes for fast and high density Li-ion storage material. *Electrochemistry communications*, 10(11):1669–1672, 2008.
- [219] Jae-Hun Kim, Soon Hyung Kang, Kai Zhu, Jin Young Kim, Nathan R Neale, and Arthur J Frank. Ni–NiO core-shell inverse opal electrodes for supercapacitors. *Chemical Communications*, 47(18):5214–5216, 2011.
- [220] Gao-Ren Li, Zi-Long Wang, Fu-Lin Zheng, Yan-Nan Ou, and Ye-Xiang Tong. $\text{ZnO}@ \text{MOF}$ core/shell nanocables: facile electrochemical synthesis and enhanced supercapacitor performances. *Journal of Materials Chemistry*, 21(12):4217–4221, 2011.
- [221] Bhekumuzi Prince Gumbi. *Comparison of metachromatic titration versus a novel nano-gold tagging technique for the detection and quantification of polydiallyldimethylammonium chloride in water samples*. PhD thesis, 2013.

- [222] X-C Xiao, L-Y Chu, W-M Chen, Shu Wang, and Yan Li. Positively thermo-sensitive monodisperse core-shell microspheres. *Advanced Functional Materials*, 13(11):847–852, 2003.
- [223] Jin Luo, Lingyan Wang, Derrick Mott, Peter N Njoki, Yan Lin, Ting He, Zhichuan Xu, Bridgid N Wanjana, I-Im S Lim, and Chuan-Jian Zhong. Core/shell nanoparticles as electrocatalysts for fuel cell reactions. *Advanced Materials*, 20(22):4342–4347, 2008.
- [224] Yajun Wang, Alexandra S Angelatos, and Frank Caruso. Template synthesis of nanostructured materials via layer-by-layer assembly. *Chemistry of Materials*, 20(3):848–858, 2008.
- [225] Frank Caruso. Nanoengineering of particle surfaces. *Advanced materials*, 13(1):11–22, 2001.
- [226] Hao Zeng, Jing Li, ZL Wang, JP Liu, and Shouheng Sun. Bimagnetic core/shell $\text{FePt}/\text{Fe}_3\text{O}_4$ nanoparticles. *Nano letters*, 4(1):187–190, 2004.
- [227] Peter Reiss, Myriam Protiere, and Liang Li. Core/shell semiconductor nanocrystals. *small*, 5(2):154–168, 2009.
- [228] Manman Ren, Zhen Zhou, Xueping Gao, and Jie Yan. Core-shell materials for lithium ion batteries. *Progress in Chemistry*, 20(05):771, 2008.
- [229] Tao Chen, Baorui Cheng, Rengpeng Chen, Yi Hu, Hongling Lv, Guoyin Zhu, Yanrong Wang, Lianbo Ma, Jia Liang, Zuoxiu Tie, et al. Hierarchical ternary carbide nanoparticle/carbon nanotube-inserted n-doped carbon concave-polyhedrons for efficient lithium and sodium storage. *ACS Applied Materials & Interfaces*, 8(40):26834–26841, 2016.
- [230] Kwing To Lai, Iryna Antonyshyn, Yurii Prots, and Martin Valldor. Anti-perovskite li-battery cathode materials. *Journal of the American Chemical Society*, 139(28):9645–9649, 2017.
- [231] Xiaodan Jia, Yufei Zhao, Guangbo Chen, Lu Shang, Run Shi, Xiaofeng Kang, Geoffrey IN Waterhouse, Li-Zhu Wu, Chen-Ho Tung, and Tierui Zhang. Ni₃Fe nanoparticles derived from ultrathin nife-layered double hydroxide nanosheets: an efficient overall water splitting electrocatalyst. *Advanced Energy Materials*, 6(10):1502585, 2016.
- [232] Yu Gu, Shuai Chen, Jun Ren, Yi Alec Jia, Chengmeng Chen, Sridhar Komarneni, Dongjiang Yang, and Xiangdong Yao. Electronic structure tuning in ni₃fen/r-go

- aerogel toward bifunctional electrocatalyst for overall water splitting. *ACS nano*, 12(1):245–253, 2018.
- [233] Shulin Zhao, Meng Li, Min Han, Dongdong Xu, Jing Yang, Yue Lin, Nai-En Shi, Yanan Lu, Rui Yang, Bitao Liu, et al. Defect-rich ni₃fen nanocrystals anchored on n-doped graphene for enhanced electrocatalytic oxygen evolution. *Advanced Functional Materials*, 28(18):1706018, 2018.
- [234] Zijian Li, Haeseong Jang, Danni Qin, Xiaoli Jiang, Xuqiang Ji, Min Gyu Kim, Lijie Zhang, Xien Liu, and Jaephil Cho. Alloy-strain-output induced lattice dislocation in ni₃fen/ni₃fe ultrathin nanosheets for highly efficient overall water splitting. *Journal of Materials Chemistry A*, 9(7):4036–4043, 2021.
- [235] Xiaolei Liu, Xingshuai Lv, Peng Wang, Qianqian Zhang, Baibiao Huang, Zeyan Wang, Yuanyuan Liu, Zhaoke Zheng, and Ying Dai. Improving the her activity of ni₃fen to convert the superior oer electrocatalyst to an efficient bifunctional electrocatalyst for overall water splitting by doping with molybdenum. *Electrochimica Acta*, 333:135488, 2020.
- [236] Yanping Zhu, Gao Chen, Xiaomin Xu, Guangming Yang, Meilin Liu, and Zongping Shao. Enhancing electrocatalytic activity for hydrogen evolution by strongly coupled molybdenum nitride@ nitrogen-doped carbon porous nano-octahedrons. *ACS Catalysis*, 7(5):3540–3547, 2017.
- [237] Yongqi Zhang, Guichong Jia, Huanwen Wang, Bo Ouyang, Rajdeep Singh Rawat, and Hong Jin Fan. Ultrathin cnts@ feooh nanoflake core/shell networks as efficient electrocatalysts for the oxygen evolution reaction. *Materials Chemistry Frontiers*, 1(4):709–715, 2017.
- [238] Lei Wang, Yang Yang, Yajun Zhang, Qiang Rui, Beibei Zhang, Zhiqiang Shen, and Yingpu Bi. One-dimensional hematite photoanodes with spatially separated pt and feooh nanolayers for efficient solar water splitting. *Journal of Materials Chemistry A*, 5(32):17056–17063, 2017.
- [239] Fangyu Xiong, Haizheng Tao, and Yuanzheng Yue. Role of amorphous phases in enhancing performances of electrode materials for alkali ion batteries. *Frontiers in Materials*, 6:328, 2020.
- [240] Dongxue Wang, Zhixuan Wei, Yunxiang Lin, Nan Chen, Yu Gao, Gang Chen, Li Song, and Fei Du. Intercalation pseudocapitance in a nasicon-structured na₂crti(po₄)₃@ carbon nanocomposite: towards high-rate and long-lifespan sodium-ion-based energy storage. *Journal of Materials Chemistry A*, 7(36):20604–20613, 2019.

- [241] Min Zhou, Yang Xu, Chengliang Wang, Qianwen Li, Junxiang Xiang, Liying Liang, Minghong Wu, Huaping Zhao, and Yong Lei. Amorphous tio₂ inverse opal anode for high-rate sodium ion batteries. *Nano Energy*, 31:514–524, 2017.
- [242] Satoshi Nakata, Takuya Togashi, Tsuyoshi Honma, and Takayuki Komatsu. Cathode properties of sodium iron phosphate glass for sodium ion batteries. *Journal of Non-Crystalline Solids*, 450:109–115, 2016.
- [243] Jongsoon Kim, Dong-Hwa Seo, Hyungsub Kim, Inchul Park, Jung-Keun Yoo, Sung-Kyun Jung, Young-Uk Park, William A Goddard III, and Kisuk Kang. Unexpected discovery of low-cost maricite nafepo₄ as a high-performance electrode for na-ion batteries. *Energy & Environmental Science*, 8(2):540–545, 2015.
- [244] Vinod Mathew, Sungjin Kim, Jungwon Kang, Jihyeon Gim, Jinju Song, Joseph Paul Baboo, Wangeun Park, Docheon Ahn, Junhee Han, Lin Gu, et al. Amorphous iron phosphate: potential host for various charge carrier ions. *NPG Asia Materials*, 6(10):e138–e138, 2014.
- [245] Yongjin Fang, Lifen Xiao, Jiangfeng Qian, Xinping Ai, Hanxi Yang, and Yuliang Cao. Mesoporous amorphous fepo₄ nanospheres as high-performance cathode material for sodium-ion batteries. *Nano letters*, 14(6):3539–3543, 2014.
- [246] Bert Conings, Jeroen Drijkoningen, Nicolas Gauquelin, Aslihan Babayigit, Jan D’Haen, Lien D’Olieslaeger, Anitha Ethirajan, Jo Verbeeck, Jean Manca, Edoardo Mosconi, et al. Intrinsic thermal instability of methylammonium lead trihalide perovskite. *Advanced Energy Materials*, 5(15):1500477, 2015.
- [247] Juchuan Li, Cheng Ma, Miaofang Chi, Chengdu Liang, and Nancy J Dudney. Solid electrolyte: the key for high-voltage lithium batteries. *Advanced Energy Materials*, 5(4):1401408, 2015.
- [248] Yongchang Liu, Ning Zhang, Fanfan Wang, Xiaobin Liu, Lifang Jiao, and Li-Zhen Fan. Approaching the downsizing limit of maricite nafepo₄ toward high-performance cathode for sodium-ion batteries. *Advanced Functional Materials*, 28(30):1801917, 2018.
- [249] Xingde Xiang, Kai Zhang, and Jun Chen. Recent advances and prospects of cathode materials for sodium-ion batteries. *Advanced materials*, 27(36):5343–5364, 2015.
- [250] Wen Liu, Pilgun Oh, Xien Liu, Min-Joon Lee, Woongrae Cho, Sujong Chae, Youngsik Kim, and Jaephil Cho. Nickel-rich layered lithium transition-metal oxide for high-energy lithium-ion batteries. *Angewandte Chemie International Edition*, 54(15):4440–4457, 2015.

- [251] Peng-Fei Wang, Ya You, Ya-Xia Yin, and Yu-Guo Guo. Layered oxide cathodes for sodium-ion batteries: phase transition, air stability, and performance. *Advanced Energy Materials*, 8(8):1701912, 2018.
- [252] Chen Xu, Yi Zeng, Xianhong Rui, Jixin Zhu, Huiteng Tan, Antonio Guerrero, Juan Toribio, Juan Bisquert, Germà Garcia-Belmonte, and Qingyu Yan. Amorphous iron oxyhydroxide nanosheets: synthesis, li storage, and conversion reaction kinetics. *The Journal of Physical Chemistry C*, 117(34):17462–17469, 2013.
- [253] Dong Jun Lee, Seung-Ho Yu, Hyeon Seok Lee, Aihua Jin, Jisoo Lee, Ji Eun Lee, Yung-Eun Sung, and Taeghwan Hyeon. Facile synthesis of metal hydroxide nanoplates and their application as lithium-ion battery anodes. *Journal of Materials Chemistry A*, 5(18):8744–8751, 2017.
- [254] Yonghuan Fu, Liewu Li, Shenghua Ye, Penggang Yang, Peng Liao, Xiangzhong Ren, Chuanxin He, Qianling Zhang, and Jianhong Liu. Construction of cobalt oxyhydroxide nanosheets with rich oxygen vacancies as high-performance lithium-ion battery anodes. *Journal of Materials Chemistry A*, 9(1):453–462, 2021.
- [255] Anh Tien Nguyen, Viet Duc Phung, Valentina Olegovna Mittova, Hai Dang Ngo, Thuan Ngoc Vo, My Linh Le Thi, Irina Yakovlevna Mittova, My Loan Phung Le, Yong Nam Ahn, Il Tae Kim, et al. Fabricating nanostructured hfoe₃ perovskite for lithium-ion battery anodes via co-precipitation. *Scripta Materialia*, 207:114259, 2022.
- [256] Keshu Dai, Qinyun Wang, Yuting Xie, Miao Shui, and Jie Shu. Disordered carbon coating free li_{0.2375}la_{0.5875}tio₃: a superior perovskite anode material for high power long-life lithium-ion batteries. *Journal of Materials Science*, pages 1–14, 2022.
- [257] Anshuman Chaupatnaik and Prabeer Barpanda. Perovskite lead-based oxide anodes for rechargeable batteries. *Electrochemistry Communications*, 127:107038, 2021.
- [258] Yuta Fujii, Daniel Ramirez, Nataly Carolina Rosero-Navarro, Domingo Jullian, Akira Miura, Franklin Jaramillo, and Kiyoharu Tadanaga. Two-dimensional hybrid halide perovskite as electrode materials for all-solid-state lithium secondary batteries based on sulfide solid electrolytes. *ACS applied energy materials*, 2(9):6569–6576, 2019.

- [259] Tufan Paul, Soumen Maiti, Biplab Kr Chatterjee, Partha Bairi, Bikram Kumar Das, Subhasish Thakur, and Kalyan Kumar Chattopadhyay. Electrochemical performance of 3d network CsPbBr_3 perovskite anodes for li-ion batteries: Experimental venture with theoretical expedition. *The Journal of Physical Chemistry C*, 125 (31):16892–16902, 2021.
- [260] Nahid Kaisar, Tanmoy Paul, Po-Wei Chi, Yu-Hsun Su, Anupriya Singh, Chih-Wei Chu, Maw-Kuen Wu, and Phillip M Wu. Electrochemical performance of orthorhombic CsPbI_3 perovskite in li-ion batteries. *Materials*, 14(19):5718, 2021.
- [261] Xiaolei Li, Zifeng Lin, Na Jin, Xiaojiao Yang, Yibo Du, Li Lei, Patrick Rozier, Patrice Simon, and Ying Liu. Perovskite-type SrVO_3 as high-performance anode materials for lithium-ion batteries. *Advanced Materials*, page 2107262, 2021.
- [262] Limin Chang, Jiahui Li, Zaiyuan Le, Ping Nie, Yu Guo, Hairui Wang, Tianhao Xu, and Xiangxin Xue. Perovskite-type CaMnO_3 anode material for highly efficient and stable lithium ion storage. *Journal of Colloid and Interface Science*, 584:698–705, 2021.
- [263] Athanasia Kostopoulou, Dimitra Vernardou, Dimitra Makri, Konstantinos Brintakis, Kyriaki Savva, and Emmanuel Stratakis. Highly stable metal halide perovskite microcube anodes for lithium-air batteries. *Journal of Power Sources Advances*, 3:100015, 2020.
- [264] Pulak Pal and Aswini Ghosh. Three-dimensional CsPbCl_3 perovskite anode for quasi-solid-state li-ion and dual-ion batteries: Mechanism of Li^+ conversion process in perovskite. *Physical Review Applied*, 14(6):064010, 2020.
- [265] Lu Zhang, Xiaohua Zhang, Guiying Tian, Qinghua Zhang, Michael Knapp, Helmut Ehrenberg, Gang Chen, Zexiang Shen, Guochun Yang, Lin Gu, et al. Lithium lanthanum titanate perovskite as an anode for lithium ion batteries. *Nature communications*, 11(1):1–8, 2020.
- [266] A Kostopoulou, D Vernardou, K Savva, and E Stratakis. All-inorganic lead halide perovskite nanohexagons for high performance air-stable lithium batteries. *Nanoscale*, 11(3):882–889, 2019.
- [267] Padmini Pandey, Neha Sharma, Reena A Panchal, SW Gosavi, and Satishchandra Ogale. Realization of high capacity and cycling stability in pb-free A_2CuBr_4 ($\text{A} = \text{CH}_3\text{NH}_3/\text{Cs}$, 2 d/3 d) perovskite-based li-ion battery anodes. *ChemSusChem*, 12 (16):3742–3746, 2019.
- [268] K Kamala Bharathi, Brindha Moorthy, Hanuma Kumar Dara, Lignesh Durai, and Do Kyung Kim. Electrochemical properties of $\text{Na}_0.5\text{Bi}_0.5\text{Tl}_0.5\text{O}_3$ perovskite as an

- anode material for sodium ion batteries. *Journal of Materials Science*, 54(20):13236–13246, 2019.
- [269] Junnan Liu, Eslam Sheha, Samaa I El-Dek, Damian Goonetilleke, Marine Harguindeguy, and Neeraj Sharma. Smfe0.3 and bi-doped smfe0.3 perovskites as an alternative class of electrodes in lithium-ion batteries. *CrystEngComm*, 20(40):6165–6172, 2018.
- [270] Xiaoyan Hu, Yiwen Tang, Ting Xiao, Jian Jiang, Zhiyong Jia, Dawei Li, Bihui Li, and Lijuan Luo. Rapid synthesis of single-crystalline srso₃(oh)6 nanowires and the performance of srso₃ nanorods used as anode materials for li-ion battery. *The Journal of Physical Chemistry C*, 114(2):947–952, 2010.
- [271] N Sharma, KM Shaju, GV Subba Rao, and BVR Chowdari. Sol-gel derived nano-crystalline casno₃ as high capacity anode material for li-ion batteries. *Electrochemistry Communications*, 4(12):947–952, 2002.
- [272] Jochen Mannhart and Darrell G Schlom. Oxide interfaces—an opportunity for electronics. *Science*, 327(5973):1607–1611, 2010.
- [273] Pavlo Zubko, Stefano Gariglio, Marc Gabay, Philippe Ghosez, and Jean-Marc Triscone. Interface physics in complex oxide heterostructures. *Annu. Rev. Condens. Matter Phys.*, 2(1):141–165, 2011.
- [274] Harold Y Hwang, Yoh Iwasa, Masashi Kawasaki, Bernhard Keimer, Naoto Nagaosa, and Yoshinori Tokura. Emergent phenomena at oxide interfaces. *Nature materials*, 11(2):103–113, 2012.
- [275] Camilo X Quintela, Kyung Song, Ding-Fu Shao, Lin Xie, Tianxiang Nan, Tula R Paudel, Neil Campbell, Xiaoqing Pan, Thomas Tybell, Mark S Rzchowski, et al. Epitaxial antiperovskite/perovskite heterostructures for materials design. *Science advances*, 6(30):eaba4017, 2020.
- [276] S Lin, DF Shao, JC Lin, L Zu, XC Kan, BS Wang, YN Huang, WH Song, WJ Lu, P Tong, et al. Spin-glass behavior and zero-field-cooled exchange bias in a c-based antiperovskite compound pdncr₃. *Journal of Materials Chemistry C*, 3(22):5683–5696, 2015.
- [277] Wen Fong Goh and Warren E Pickett. Survey of the class of isovalent antiperovskite alkaline-earth pnictide compounds. *Physical Review B*, 97(3):035202, 2018.
- [278] Daichi Matsunami, Asaya Fujita, Koshi Takenaka, and Mika Kano. Giant barocaloric effect enhanced by the frustration of the antiferromagnetic phase in mn₃gan. *Nature materials*, 14(1):73–78, 2015.

- [279] Pavel Lukashev, Renat F Sabirianov, and Kirill Belashchenko. Theory of the piezomagnetic effect in mn-based antiperovskites. *Physical Review B*, 78(18):184414, 2008.
- [280] Pavel Lukashev, Kirill D Belashchenko, and Renat F Sabirianov. Large magnetoelectric effect in ferroelectric/piezomagnetic heterostructures. *Physical Review B*, 84(13):134420, 2011.
- [281] J Zemen, E Mendive-Tapia, Z Gercsi, Rudra Banerjee, JB Staunton, and KG Sandeman. Frustrated magnetism and caloric effects in mn-based antiperovskite nitrides: Ab initio theory. *Physical Review B*, 95(18):184438, 2017.
- [282] Ding-Fu Shao, Gautam Gurung, Tula R Paudel, and Evgeny Y Tsymbal. Electrically reversible magnetization at the antiperovskite/perovskite interface. *Physical Review Materials*, 3(2):024405, 2019.
- [283] Kewen Shi, Ying Sun, Jun Yan, Sihao Deng, Lei Wang, Hui Wu, Pengwei Hu, Huiqing Lu, Muhammad Imran Malik, Qingzhen Huang, et al. Baromagnetic effect in antiperovskite $\text{mn}_3\text{ga}_0.95\text{n}_0.94$ by neutron powder diffraction analysis. *Advanced Materials*, 28(19):3761–3767, 2016.
- [284] Zhenzhen Hui, Xianwu Tang, Dingfu Shao, Renhuai Wei, Jie Yang, Peng Tong, Wenhai Song, Xuebin Zhu, and Yuping Sun. Self-assembled c-axis oriented antiperovskite soft-magnetic cunco_3 thin films by chemical solution deposition. *Journal of Materials Chemistry C*, 3(17):4438–4444, 2015.
- [285] Muhammad Rizwan, Samina Gul, Tahir Iqbal, Uzma Mushtaq, M Hassan Farooq, Muhammad Farman, Rabia Bibi, and Mohsin Ijaz. A review on perovskite lanthanum aluminate (laalo_3), its properties and applications. *Materials Research Express*, 6(11):112001, 2019.
- [286] E Cicerrella, JL Freeouf, Lisa F Edge, Darrell G Schlom, T Heeg, J Schubert, and SA Chambers. Optical properties of la-based high-k dielectric films. *Journal of Vacuum Science & Technology A: Vacuum, Surfaces, and Films*, 23(6):1676–1680, 2005.
- [287] K Krishnaswamy, CE Dreyer, A Janotti, and CG Van de Walle. Structure and energetics of laalo_3 (001) surfaces. *Physical Review B*, 90(23):235436, 2014.
- [288] Abhijit Biswas, Chan-Ho Yang, Ramamoorthy Ramesh, and Yoon H Jeong. Atomically flat single terminated oxide substrate surfaces. *Progress in Surface Science*, 92(2):117–141, 2017.

- [289] Yueh-Lin Lee and Dane Morgan. Ab initio defect energetics of perovskite (001) surfaces for solid oxide fuel cells: A comparative study of LaMnO_3 versus SrTiO_3 and LaAlO_3 . *Physical Review B*, 91(19):195430, 2015.
- [290] D Dijkkamp, T Venkatesan, XD Wu, SA Shaheen, N Jisrawi, YH Min-Lee, WL McLean, and Mark Croft. Preparation of y-ba-cu oxide superconductor thin films using pulsed laser evaporation from high T_c bulk material. *Applied Physics Letters*, 51(8):619–621, 1987.
- [291] Tatau Nishinga and Thomas F Kuech. *Thin Films and Epitaxy*. Elsevier, 2015.
- [292] Douglas B Chrisey and Graham K Hubler. Pulsed laser deposition of thin films. *Pulsed Laser Deposition of Thin Films*, page 648, 2003.
- [293] Hans M Christen and Gyula Eres. Recent advances in pulsed-laser deposition of complex oxides. *Journal of Physics: Condensed Matter*, 20(26):264005, 2008.
- [294] Gertjan Koster, Mark Huijben, and Guus Rijnders. *Epitaxial growth of complex metal oxides*. Elsevier, 2015.
- [295] YS Sun, YF Guo, XX Wang, W Yi, JJ Li, SB Zhang, CI Sathish, AA Belik, and K Yamaura. Magnetic and electrical properties of antiperovskite Mn_3In synthesized by a high-pressure method. In *Journal of Physics: Conference Series*, volume 400, page 032094. IOP Publishing, 2012.
- [296] P Tong, YP Sun, XB Zhu, and WH Song. Synthesis and physical properties of antiperovskite-type compound $\text{In}_0.95\text{Ni}_3$. *Solid state communications*, 141(6):336–340, 2007.
- [297] Lei Ding, Cong Wang, Lihua Chu, Jun Yan, Yuanyuan Na, Qingzhen Huang, and Xiaolong Chen. Near zero temperature coefficient of resistivity in antiperovskite $\text{Mn}_3\text{Ni}_1-x\text{Cu}_x$. *Applied Physics Letters*, 99(25):251905, 2011.
- [298] Keita Ito, Geun Hyoung Lee, Hiro Akinaga, and Takashi Suemasu. Molecular beam epitaxy of ferromagnetic $\gamma\text{-Fe}_4\text{N}$ thin films on LaAlO_3 (1 0 0), SrTiO_3 (1 0 0) and MgO (1 0 0) substrates. *Journal of crystal growth*, 322(1):63–68, 2011.
- [299] Keita Ito, Kazunori Harada, Kaoru Toko, Hiro Akinaga, and Takashi Suemasu. Epitaxial growth and magnetic characterization of ferromagnetic Co_4N thin films on SrTiO_3 (001) substrates by molecular beam epitaxy. *Journal of crystal growth*, 336(1):40–43, 2011.
- [300] Yuanyuan Na, Cong Wang, Lihua Chu, Lei Ding, Jun Yan, Yafei Xue, Wanfeng Xie, and Xiaolong Chen. Preparation and properties of antiperovskite Mn_3Ni thin film. *Materials Letters*, 65(23-24):3447–3449, 2011.

- [301] Abhijit Biswas and Yoon Hee Jeong. Strain effect in epitaxial oxide heterostructures. In *Epitaxy*. IntechOpen, 2017.
- [302] Swati Parmar, Abhijit Biswas, Bishakha Ray, Suresh Gosavi, Suwarna Datar, and Satishchandra Ogale. Stabilizing metastable polymorphs of van der waals solid mos2 on single crystal oxide substrates: Exploring the possible role of surface chemistry and structure. *The Journal of Physical Chemistry C*, 125(20):11216–11224, 2021.
- [303] Ki Ro Yoon, Kihyun Shin, Jiwon Park, Su-Ho Cho, Chanhoo Kim, Ji-Won Jung, Jun Young Cheong, Hye Ryung Byon, Hyuk Mo Lee, and Il-Doo Kim. Brush-like cobalt nitride anchored carbon nanofiber membrane: current collector-catalyst integrated cathode for long cycle li-o2 batteries. *ACS nano*, 12(1):128–139, 2018.
- [304] Lucas HG Kalinke, Humberto O Stumpf, Italo O Mazali, and Danielle Cangussu. Bimetallic oxamate complexes synthesized into mesoporous matrix as precursor to tunable nanosized oxide. *Materials Research Bulletin*, 70:743–747, 2015.
- [305] O Clause, M Goncalves Coelho, M Gazzano, D Matteuzzi, F Trifiro, and A Vaccari. Synthesis and thermal reactivity of nickel-containing anionic clays. *Applied clay science*, 8(2-3):169–186, 1993.
- [306] Zied Othmen, Alejandro Schulman, Kais Daoudi, Michel Boudard, Carlos Acha, Hervé Roussel, Meherzi Oueslati, and Tetsuo Tsuchiya. Structural, electrical and magnetic properties of epitaxial $\text{La}_{0.7}\text{Sr}_{0.3}\text{CoO}_3$ thin films grown on SrTiO_3 and LaAlO_3 substrates. *Applied surface science*, 306:60–65, 2014.
- [307] Ellie L Uzunova, Georgi St Nikolov, and Hans Mikosch. Electronic structure and vibrational modes of cobalt oxide clusters Co_n ($n= 1- 4$) and their monoanions. *The Journal of Physical Chemistry A*, 106(16):4104–4114, 2002.
- [308] Zhaohui Dong, Zhongying Mi, Weiguang Shi, Hui Jiang, Yi Zheng, and Ke Yang. High pressure effects on hydrate Cu_2BTC investigated by vibrational spectroscopy and synchrotron x-ray diffraction. *RSC advances*, 7(87):55504–55512, 2017.
- [309] YG Cao, XL Chen, YC Lan, JY Li, YP Xu, T Xu, QL Liu, and JK Liang. Blue emission and raman scattering spectrum from AlN nanocrystalline powders. *Journal of Crystal Growth*, 213(1-2):198–202, 2000.
- [310] Yongsheng Xu, Binbin Yao, Dan Liu, Weiwei Lei, Pinwen Zhu, Qiliang Cui, and Guangtian Zou. Room temperature ferromagnetism in new diluted magnetic semiconductor $\text{AlN}:\text{Mg}$ nanowires. *CrystEngComm*, 15(17):3271–3274, 2013.

- [311] Yongqi Zhang, Bo Ouyang, Guankui Long, Hua Tan, Zhe Wang, Zheng Zhang, Weibo Gao, Rajdeep Singh Rawat, and Hong Jin Fan. Enhancing bifunctionality of con nanowires by mn doping for long-lasting zn-air batteries. *Science China Chemistry*, 63(7):890–896, 2020.
- [312] Fengmei Yu, Lizhu Ren, Meng Meng, Yunjia Wang, Mei Yang, Shuxiang Wu, and Shuwei Li. Growth and magnetic property of antiperovskite manganese nitride films doped with cu by molecular beam epitaxy. *Journal of Applied Physics*, 115(13):133911, 2014.
- [313] Takafumi Ishii, Akihiro Horiuchi, and Jun-ichi Ozaki. An ion-sensitive field effect transistor using metal-coordinated zeolite-templated carbons as a three-dimensional graphene nanoribbon network. *Frontiers in Materials*, 6:129, 2019.
- [314] Charles Daniel Wagner. *Handbook of x-ray photoelectron spectroscopy: a reference book of standard data for use in x-ray photoelectron spectroscopy*. Perkin-Elmer, 1979.
- [315] Hua Chen, Qian Niu, and Allan H MacDonald. Anomalous hall effect arising from noncollinear antiferromagnetism. *Physical review letters*, 112(1):017205, 2014.
- [316] AH MacDonald and M Tsoi. Antiferromagnetic metal spintronics. *Philosophical Transactions of the Royal Society A: Mathematical, Physical and Engineering Sciences*, 369(1948):3098–3114, 2011.
- [317] Satoru Nakatsuji, Naoki Kiyohara, and Tomoya Higo. Large anomalous hall effect in a non-collinear antiferromagnet at room temperature. *Nature*, 527(7577):212–215, 2015.
- [318] ZQ Liu, H Chen, JM Wang, JH Liu, K Wang, ZX Feng, H Yan, XR Wang, CB Jiang, JMD Coey, et al. Electrical switching of the topological anomalous hall effect in a non-collinear antiferromagnet above room temperature. *Nature Electronics*, 1(3):172–177, 2018.
- [319] T Jungwirth, J Sinova, Aurelien Manchon, X Marti, J Wunderlich, and C Felser. The multiple directions of antiferromagnetic spintronics. *Nature Physics*, 14(3):200–203, 2018.
- [320] Anthony R West. *Solid state chemistry and its applications*. John Wiley & Sons, 2014.
- [321] Youssef Ben Smida, Riadh Marzouki, Savaş Kaya, Sultan Erkan, Mohamed Faouzi Zid, and Ahmed Hichem Hamzaoui. Synthesis methods in solid-state chemistry. In *Synthesis Methods and Crystallization*. IntechOpen, 2020.

- [322] Deepak P Dubal, Omar Ayyad, Vanesa Ruiz, and Pedro Gomez-Romero. Hybrid energy storage: the merging of battery and supercapacitor chemistries. *Chemical Society Reviews*, 44(7):1777–1790, 2015.
- [323] Li Guan, Linpo Yu, and George Z Chen. Capacitive and non-capacitive faradaic charge storage. *Electrochimica Acta*, 206:464–478, 2016.
- [324] Jingsong Huang, Bobby G Sumpter, and Vincent Meunier. A universal model for nanoporous carbon supercapacitors applicable to diverse pore regimes, carbon materials, and electrolytes. *Chemistry—A European Journal*, 14(22):6614–6626, 2008.
- [325] Elzbieta Frackowiak, Krzysztof Fic, Mikolaj Meller, and Grzegorz Lota. Electrochemistry serving people and nature: High-energy ecocapacitors based on redox-active electrolytes. *ChemSusChem*, 5(7):1181–1185, 2012.
- [326] SW Zhang and George Zheng Chen. Manganese oxide based materials for supercapacitors. *Energy Materials*, 3(3):186–200, 2008.
- [327] Linghao Su, Liangyu Gong, Haitao Lü, and Qiang Xü. Enhanced low-temperature capacitance of mno₂ nanorods in a redox-active electrolyte. *Journal of Power Sources*, 248:212–217, 2014.
- [328] Nagaphani B Aetukuri, Bryan D McCloskey, Jeannette M García, Leslie E Krupp, Venkatasubramanian Viswanathan, and Alan C Luntz. On the origin and implications of li₂o₂ toroid formation in nonaqueous li-o₂ batteries. *arXiv preprint arXiv:1406.3335*, 2014.
- [329] D Larcher and JM Tarascon. Towards greener and more sustainable batteries for electrical energy storage. *nat chem* 7: 19–29, 2015.
- [330] Xiaoqi Sun, Patrick Bonnicksen, Victor Duffort, Miao Liu, Ziqin Rong, Kristin A Persson, Gerbrand Ceder, and Linda F Nazar. A high capacity thiospinel cathode for mg batteries. *Energy & Environmental Science*, 9(7):2273–2277, 2016.
- [331] Naoaki YABUUCHI and Kei KUBOTA. Mouad dahbi a shinichi komaba. *Research Development on Sodium-Ion Batteries. Chemical Reviews*, 114(23):11636–11682, 2014.
- [332] M Rosa Palacin. Recent advances in rechargeable battery materials: a chemist’s perspective. *Chemical Society Reviews*, 38(9):2565–2575, 2009.
- [333] CP Grey and JM Tarascon. Sustainability and in situ monitoring in battery development. *Nature materials*, 16(1):45–56, 2017.

-
- [334] Alexandre Ponrouch, Carlos Frontera, Fanny Bardé, and M Rosa Palacín. Towards a calcium-based rechargeable battery. *Nature materials*, 15(2):169–172, 2016.
- [335] Shunsuke Yagi, Tetsu Ichitsubo, Yoshimasa Shirai, Shingo Yanai, Takayuki Doi, Kuniaki Murase, and Eiichiro Matsubara. A concept of dual-salt polyvalent-metal storage battery. *Journal of Materials Chemistry A*, 2(4):1144–1149, 2014.

Publications

1. Fe₃SnC@CNF: A 3D Antiperovskite Intermetallic Carbide System as a New Robust High-Capacity Lithium-Ion Battery Anode.
K Roy, V Chvan, **SM Hossain**, S Halder, R Vaidhyanathan, P Ghosh, S. Ogale, *ChemSusChem* 13 (1), 196-204, 2020; doi: [10.1002/cssc.201902508](https://doi.org/10.1002/cssc.201902508) (Equal Contributions)
2. Growth Properties and Applications of Pulsed Laser Deposited Nanolaminate Thin Films.
A Biswas, A Sengupta, U Rajput, SK Singh, V Antad, **SM Hossain**, Satishchandra Ogale, *Phys. Rev. Applied* 13, 044075-Published 29 April 2020; doi: [10.1103/PhysRevApplied.13.044075](https://doi.org/10.1103/PhysRevApplied.13.044075)
3. Visible Light-Driven Highly Selective CO₂ Reduction to CH₄ using Potassium Doped C₃N₅.
Bharati Debnath, Saideep Singh, **Sk Mujaffar Hossain**, Shreya Krishnamurthy, Vivek Polshettiwar, and Satishchandra Ogale
Langmuir 2022, 38, 3139-3148; doi: [10.1021/acs.langmuir.1c03127](https://doi.org/10.1021/acs.langmuir.1c03127)
4. Construction of a 2D/2D g-C₃N₅/NiCr-LDH Heterostructure to Boost the Green Ammonia Production Rate under Visible Light Illumination.
Bharati Debnath, **Sk Mujaffar Hossain**, and Satishchandra Ogale1 (*Under review ACS Applied Materials & Interfaces*)
5. Lithiation-induced Evolution of Biphasic Constitution in Intermetallic Anti-perovskite Fe₃SnC and its consequences for magnetism: A Case for Rechargeable Spintronic Battery.
Sk Mujaffar Hossain, Vinila Bedekar, Priyanka Yadav, Bharati Debnath, Ram Janay Chaudhary, Prasenjit Ghosh, Satishchandra Ogale (*Status: Manuscript ready for submission*)
6. Surface-modified Antiperovskite Nitride Co₃CuN as a High Capacitive Anode Material Boosting Li-Ion Storage Capacity.
Sk Mujaffar Hossain, Bharati Debnath, Prasenjit Ghosh, and Satishchandra Ogale (*Status: Manuscript ready for submission*)
7. Significant enhancement of oxygen evolution activity of 4d/5d based epitaxial bimetallic SrIr_{0.5}Ru_{0.5}O₃ films over the films of SrIrO₃ and SrRuO₃ grown by

pulsed laser deposition.

Abhijit Biswas G. Shiva Shanker, Tisita Das, **Sk Mujaffar Hossain**, Gourav Singla, Sudip Chakraborty, and Satishchandra Ogale (*Status: Manuscript under preparation*)